ISTITUTO SUPERIORE DI SANITÀ

III Workshop BIOFLUMEN
Biological Fluid Mechanics Network

Technological innovation and evaluation of medical devices for the cardiovascular system

Istituto Superiore di Sanità
Rome, 15 November 2004

Proceedings edited by
Mauro Grigioni

Dipartimento di Tecnologie e Salute

ISSN 1123-3117
Rapporti ISTISAN
05/46

Istituto Superiore di Sanità
III workshop BIOFLUMEN. Biological Fluid Mechanics Network. Technological innovation and evaluation of medical devices for the cardiovascular system. Istituto Superiore di Sanità. Rome, 15 November 2004.
Proceedings edited by Mauro Grigioni
2005, iii, 101 p. Rapporti ISTISAN 05/46

The network BIOFLUMEN (Biological Fluid Mechanics Network) has been promoted as tool where different professional experiences, both from bioengineering and clinics, are linked to develop and to integrate investigational techniques related to physiopathological conditions, especially in the cardiovascular field. The third meeting at the Istituto Superiore di Sanità (the Italian National Institute of Health) presented the state of the art of *in vitro* experimental, computational and clinically used techniques for the study of fluid dynamics and biomechanics of cardiac and vascular prosthetic devices. *In vitro* experiments showed: the possibility to characterize mechanical heart valves by means of acoustic, velocimetric, vibrational and thermographic methodologies; the possibility to evaluate the thermal gradient related to medical device exposed to magnetic field; and how magnetic resonance could influence prosthetic heart valves mechanically. Computational fluid dynamics highlighted its usefulness in the definition of several indices for the evaluation of the efficiency of vascular anastomosis, for the prediction of the degree of perfusion of vascular districts and for the investigation of complex fluid-structure-interaction due to the dynamics of prosthetic heart valves and artificial ventricles.
Key words: Experimental investigation, Computational Fluid Dynamics, Evaluation of medical devices

Istituto Superiore di Sanità
III Workshop BIOFLUMEN. Biological Fluid Mechanics Network. Innovazione tecnologica e valutazione di dispositivi medici per il sistema cardiovascolare. Istituto Superiore di Sanità. Roma, 15 novembre 2004.
Atti a cura di Mauro Grigioni
2005, iii, 101 p. Rapporti ISTISAN 05/46 (in inglese)

Il network BIOFLUMEN (Biological Fluid Mechanics Network) è stato costituito come punto di incontro di diverse professionalità, sia bioingegneristiche che mediche, per sviluppare e integrare metodi di indagine relativamente a problematiche di carattere fisiopatologico, specialmente in ambito cardiovascolare. La terza edizione del Workshop, tenutosi presso l'Istituto Superiore di Sanità, ha presentato lo stato dell'arte delle metodologie sperimentali, numeriche e cliniche, adottate per studiare i diversi aspetti fluidodinamici e meccanici di dispositivi cardiaci e vascolari. I metodi sperimentali presentati hanno messo in evidenza le diverse possibilità di: caratterizzare valvole cardiache meccaniche mediante analisi acustica, velocimetrica, vibrazionale e termografica; valutare il gradiente termico relativo a pacemaker sottoposti a campi magnetici presenti durante risonanza magnetica; e stimare, infine, come quest'ultima metodica possa influire meccanicamente sulle protesi meccaniche cardiache. Gli studi numerici di fluidodinamica computazionale hanno mostrato come possano essere di ausilio nel definire indici per valutare l'efficienza di anastomosi vascolari, nel predire i livelli di perfusione di distretti anatomici e nel presentare i risultati di complessi modelli di interazione fluido-struttura per valvole cardiache e fluidodinamica ventricolare.
Parole chiave: Studi sperimentali, Fluidodinamica computazionale, Valutazione di dispositivi medici

Per informazioni su questo documento scrivere a: grigioni@iss.it.

Il rapporto è accessibile online dal sito di questo Istituto: www.iss.it.

Presidente dell'Istituto Superiore di Sanità e Direttore responsabile: *Enrico Garaci*
Registro della Stampa - Tribunale di Roma n. 131/88 del 1° marzo 1988

Redazione*: Paola De Castro, Sara Modigliani* e *Sandra Salinetti*
La responsabilità dei dati scientifici e tecnici è dei singoli autori.

TABLE OF CONTENTS

PRESENTATION

A recent restructuring of the governmental bodies in the health sector which supervise the diffusion and the use of medical devices calls for new viewpoints and further investigational efforts by part of the scientific community, considering both the design aspects and the social impact that such technologies have nowadays gained. The consideration of such aspects are resumed in the methodology usually referred to as technological evaluation. The latter comprehends, then, not only purely technical evaluations, but also (if not especially) considerations of ethical and social nature, the methodological implications for the use as well as economical considerations. The balance between these exigencies and those related to the safety and efficacy of medical devices define the framework in which the scientific community of bioengineers (then, not limiting the scope to the participants to our biannual meetings), together with the clinicians, must position itself on the normative as well as on the research standpoint.

The insight that originate from the requests of information by governmental bodies, from those more specifically of technical nature to those of statistical type (epidemiology data), as a support to decisional processes in monitoring activities of the market and of the applications of medical devices, highlight the lack of articulated proposals for studies in these fields. The velocity of technological innovation in the sector of medical devices (in which coronary stents and filtering systems for the reduction of the neurological damage by embolization represent some of the most debated topics, to date) is forcing the community of clinicians and he scientific societies to face new problems with the instrument of the consensus conference (see, e.g., the case of Drug Eluting Stents (DES) addressed by GISE), more agile with respect to the issueing of guidelines, which generally requires systematic literature studies; the latter, as opposed to what occurs with drugs, is generally scarce as well as volatile, owing to the extreme adaptability of the devices to specific cases, very different from each other, and to the impressive rythm of modifications that a given device is subjected to during the course of its application, until it finally disappears, substituted by other devices.

In this scenario, the availability has become essential of scientific works oriented to the analysis of risk, to highlight particular aspects relative to the possible reduction of complications not only by means of design modifications but even more with the appropriate intended use, and finally assessments related to the ecoomical convenience and applicative opportunity. Goverrnmental bodies have – and will be having even more in the future – the necessity of defining the so-called therapeutical paths for the application of the proposed technologies in the health sector, and the difficulties inherent to the category of medical devices pose to us and to our disciplines requirements ever more clear in terms of multidisciplinarity, and challenges in the set-up of evaluation methods able to respond appropriately to these requirements.

Mauro Grigioni

LASER VIBROMETRY FOR THE STUDY OF PROSTHETIC MECHANICAL HEART VALVES

Lorenzo Scalise (a), Paolo Castellini (a), Umberto Morbiducci (a, b), Costantino Del Gaudio (b), Mauro Grigioni (b), Enrico Primo Tomasini (a)
(a) Dipartimento di Meccanica, Università Politecnica delle Marche, Ancona, Italy
(b) Dipartimento di Tecnologie e Salute, Istituto Superiore di Sanità, Rome, Italy

Introduction

Laser techniques, due to the non-contact nature, are an interesting alternative investigational methodology to be tested in the study of biomedical devices for the cardiovascular system, especially as evaluation method in design and quality control of artificial organs. The applicability and accuracy of laser Doppler measurement technique depends on the conditions in which the system operates, i.e., the level of the signal available, the environmental conditions, the characteristics of the surface observed, the presence of other shifts in addition to the ones pointed out (1, 2). Different fields of application have been reported in the past years for Laser Doppler Vibrometry (LDVi) (2). In particular, the use of LDVi has found many application in medicine in dentistry (3), and hortopedics (4). Laser vibrometry technique (LDVi) applied on prosthetic heart valves could be regarded as an useful tool in order to analyse the mechanical features of these devices for a detailed comprehension of their working conditions. Aim of the present study is to verify if, notwithstanding the interfering inputs due to the operative conditions of mechanical prosthetic heart valves, a non contact approach such as LDVi allows to extract on valves' kinematics informations reliable to their specific design features. To do this, two different experimental set-up have been built up. The proposed method could be useful in the definition of valves' behaviour in repeatable experimental conditions. The critical points and difficulties to build up experimental studies in this field have been clearly pointed out.

Materials and methods

A laser Doppler vibrometer is based on the principle of the detection of the Doppler shift of coherent laser light, scattered from a small area of the vibrating specimen (1). The relationship of the Doppler frequency shift f_D and the phase change Φ introduced into the measurement beam, with the vibrational velocity v and displacement d, respectively, are expressed by:

$$f_D = 2\frac{v(t)}{\lambda} \qquad \text{Eq. [1]}$$

$$\Phi = 4\pi\frac{d(t)}{\lambda} \qquad \text{Eq. [2]}$$

with λ being the wavelenght of the laser light. Therefore, vibrational velocity and displacement can be obtained from Eq. [1] and Eq. [2], respectively.Two experimental set-ups have been studied.In the first one (experimental set-up A), a Single Point Vibrometer was used to measure the vibrations on a Bjork-Shiley monostruct valve. A pulsatile flow loop was appositely realised (5) and was filled with water, which is pumped by a pulse generator generating the pulsatile flow regime The pulse generator operates in a range of 70 to 140 cycles/min, with a cardiac output up to 6 L/min. Tests have been conducted in fluidynamic equivalence (5) between water

and blood (20 to 40 cycles/min). In order to have optical access the valve was mounted in a test chamber made of acrylic. The access of the vibrometer was obtained using a glass window placed at the end of the chamber outlet pipe. A photo of experimental set-up A is shown in Figure 1.

Figure 1. Experiment A: set-up

The second session (experimental set-up B) was performed with a pulsatile mock circulatory system (MCS), the VSI (Vivitro Systems Inc.), properly modified (6): in it, the hydrodynamic and kinematic behaviour of two of the most commonly implanted mechanical bileaflet heart valves, the St. Jude HP (SJ27) and the Carbomedics (CM27) 27 mm tissue annulus diameter, were investigated. A schematic of the second experimental set-up is shown in Figure 2.

Figure 2. Experiment B: set-up

The pump drive waveforms implemented in the adopted MCS are able to mimic physiological haemodynamic waveforms. A cardiac output of 2 L/min, with a mean arterial pressure of 100 mmHg and a heart beat of 70 beats per minute are the investigated working conditions for the prosthetic valve.The study of the kinematics of the prosthetic valve was performed using a laser Doppler vibrometric system PSV-300 (Polytec, De). The VSI mock circulatory loop allows to approach the vision of the valvular function in the aortic site by means of a glass window, through which the laser light has been oriented (Figure 2). Proper own Labview codes controlling the VSI system, as well as the first experimental set-up, provided the trigger to synchronize the vibrometer recording with the cardic cycle. In both the two experimental sessions, the laser beam was not kept at a fixed point on the specimen:

- a scanning of two points (point 2, on the center of the occluder; point 3, on the center of the strut leg) on the valve with a laser head and a contemporary measure with the other laser head pointed on the valve ring (point 1), for the set-up A;
- a scanning of four characteristic points on the leaflets surface (two for each leaflet), very close to the couplings hinge/pivot, (carried out in the attempt to catch specific features both in the opening and the closing phase of the valve), for the set-up B.

A sketch of the location of the measurements points in the two experimental sessions, together with the nomenclature chosen for their identification, is showed in Figure 3. It must be pointed out that:

- for the set-up A, the information acquired is the velocity of the target point;
- for the set-up B, the approach adopted to the kinematic measurement allowed to follow the temporal evolutions on a position, not of a point on the leaflet (only components of the kinematic quantities perpendicular to the optical axis are measured).

As far the set-up B is concerned, each signal was sampled at 10240 Hz. The position signals, describing the mechanical valve kinematics, were successively segmented with a time period equal to the duration of a beat, averaged and normalized with respect to root mean square of the averaged waveform itself, before to proceed with the analysis in the frequency domain. The power spectra of the averaged position signals from laser measurements, relative to the two valves under investigation, are compared in terms of spectral components.

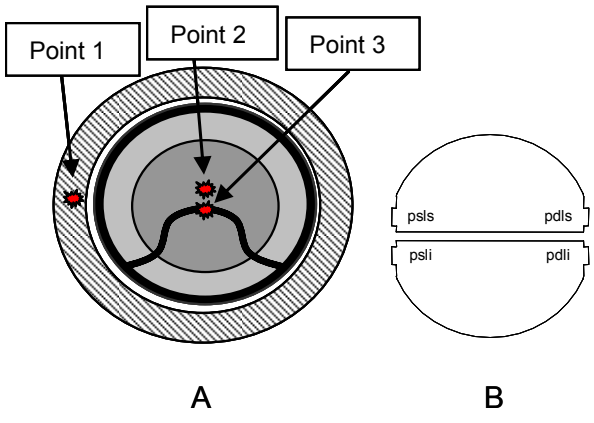

Figure 3. Sketch of the locations of the measurement points (and corresponding identifying nomenclature) for experiment A and experiment B

Results

Results obtained with the set-up A

In Figure 4, it has been reported the time history of the signal measured with the single-point vibrometer. This signal is the velocity of the target point (point 2). It is possible to observe the vibration associated to the closing of the occluder (diastole instant: 0.486 s) that it is composed by a double negative peak, with a maximum negative velocity of 1.21 mm/s. The systole is measured at 2.01 s and it is reporting a maximum velocity of the occluder of 9.95 mm/s. On the same Figure, the vibrational velocity of the valve case has been reported (measurement point 1). It is possible to observe how the two vibrational time histories have some similarities.

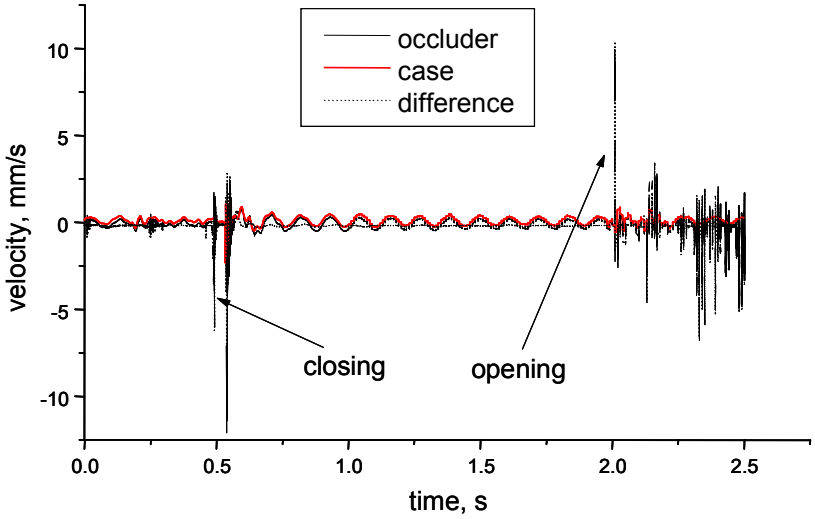

Figure 4. Single cycle on the mono-disk valve (point 1, point 2, and difference of the signals)

This demonstrates that part of the velocity measured on point 2 is also measured on the case (point 1) and is therefore not generated on the occluder during opening and closing, but is coming from the case. In order to eliminate the vibration signal of the case from the occluder signal we have subtracted the two time histories (acquired simultaneously). This signal can now be considered the vibrational time history of the occluder (point 2). Figure 5 is reporting the measurement from the strut leg, the signal (simultaneously acquired) from the case, and the difference of the two. Finally in Figure 6, it has been reported the measured power spectra of the velocity signals measured on the case and on the occluder. It is possible to observe the similar frequency content, even if the signal from the strut leg is about 20 dB in average higher then the signal from the case. Maximum difference has been obtained at 130 Hz (+33 dB) and 580 Hz (+31.7 dB).

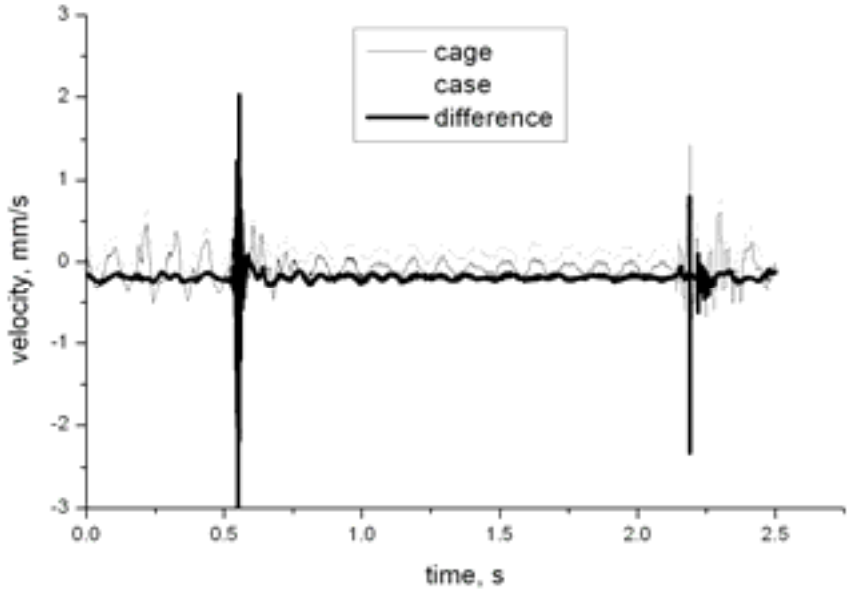

Figure 5. Single cycle on the mono-disk valve (point 1 and point 3, and difference signal)

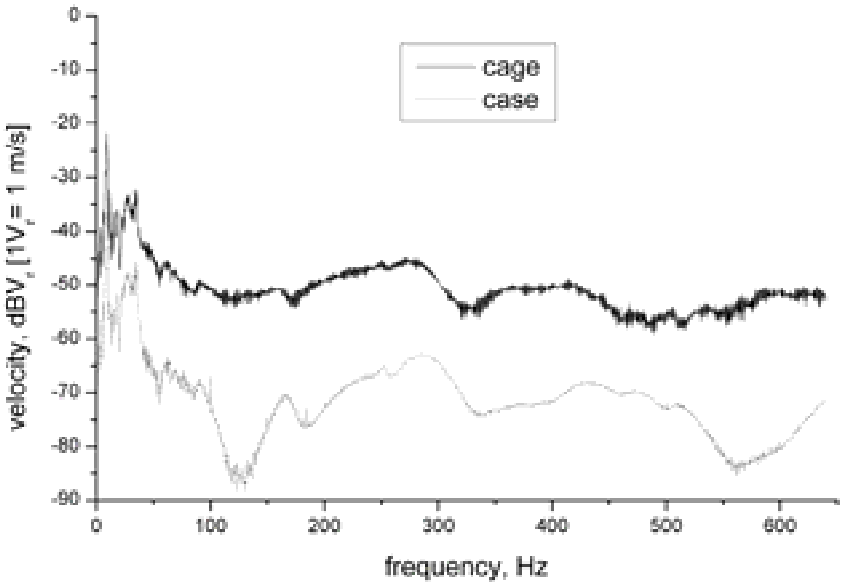

Figure 6. Power spectrum of a single cycle on the mono-disk valve (point 1 and point 2)

Results obtained with the set-up B

The position signals describing the averaged beat in all the measurements valve sites are shown in Figure 7 for the CM27, and SJ27, respectively. The averaged waveforms have been normalized with respect to their Root Mean Square (RMS) value; the averaged ventricular

pressure waveforms are also shown in those Figures, in order to correlate the kinematics of the points on the valve to the different phases in the cardiac cycle. In Figure 7, the CM27 shows a behaviour significantly different with respect to the other valve model: the position waveforms for example shows a characteristic super-elongation in the opening phase, and a trend in the closing phase that may be related to a rebound of the leaflet on the hinge after the closure impact; for the CM27 this phenomenon seems to be more significant in the ls and, even if less pronounced, it is also present in the ls of the SJ27.

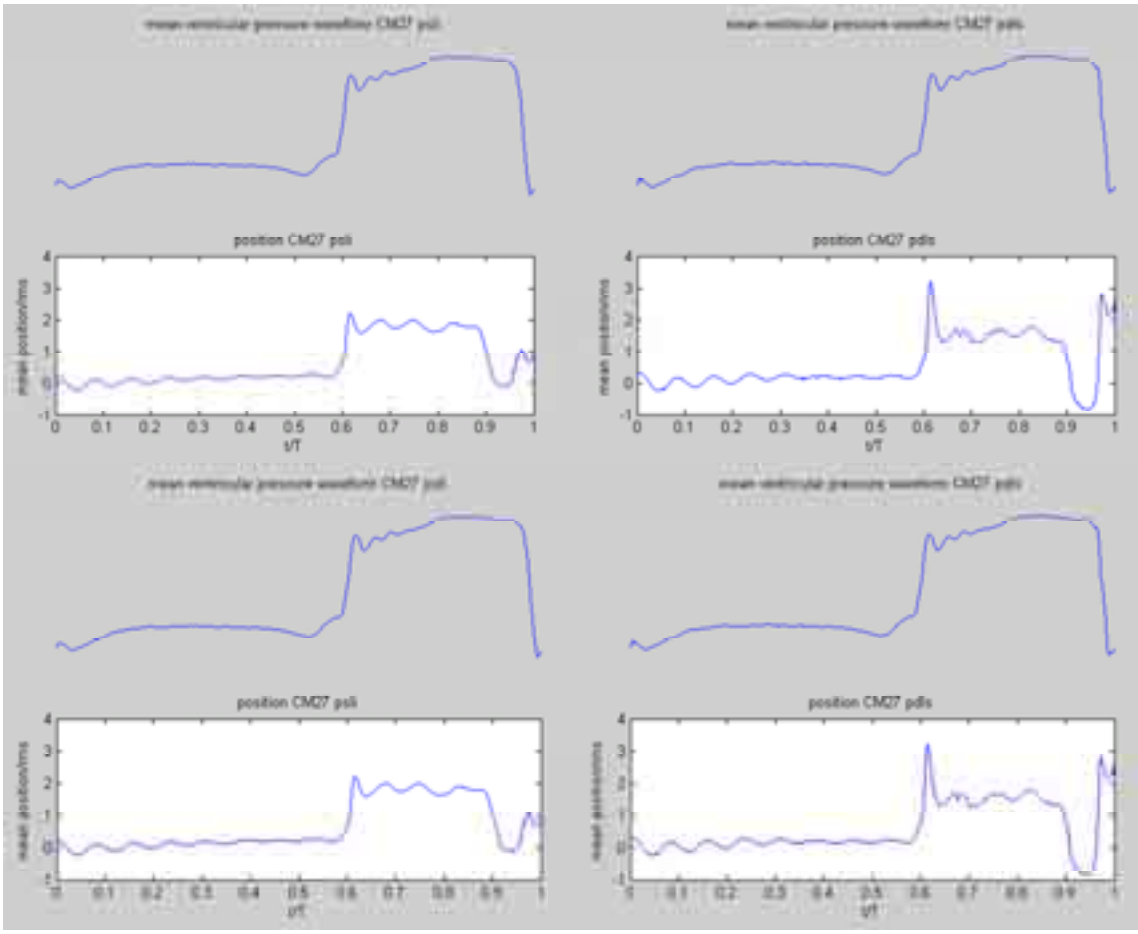

Figure 7. Averaged pressure and position (normalized with respect to RMS) waveforms in sites psli and pdls

The normalized power spectra of the position signals, in one site of measurement on the superior leaflet (pdls), are compared in Figure 8: it can be noticed how the CM27 power density spectrum is characterized by a power fraction distributed on spectral components higher than the other valve model. This behaviour may be related to a design difference between the two models: the capability, for the SJ27, to maintain the leaflets fixed when in fully open position, while for the CM27 the presence of a fluttering phenomenon is widely well-grounded in literature (7).

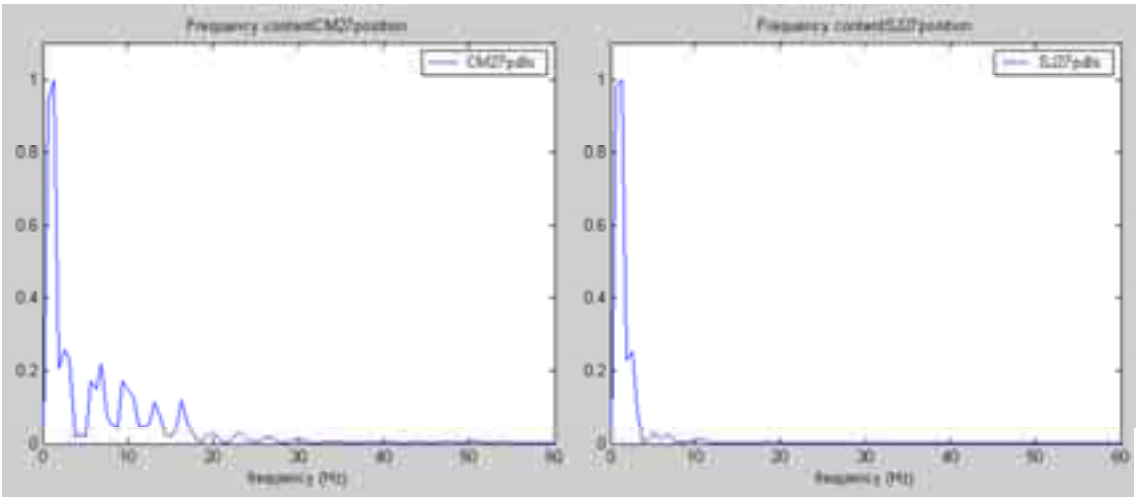

Figure 8. Normalized power spectra of the averaged position signals relative to the two valves under investigation (pdls site of measure)

Discussion

Due to their non-contact nature, laser techniques for vibration measurement offer themselves as ausiliary investigational tool to be tested in the field of biomedical devices, especially as evaluation method in design and quality control of artificial organs (no items have been found in the Medline).

The applicability and accuracy of this measurement technique depend on the conditions in which the system operates, that in the case of the study of mechanical prosthetic heart valves are:

1) characteristics of the measurand surface of the leaflet, which is poorly cooperative with respect to the usage of laser Doppler systems with its alternance, during the motion, of reflective and badly diffusive areas. This effect brings to a deterioration of the signal-to-noise ratio;
2) level of the signal available, and the laser beam loss when the measure is carried out in points of the leaflet with the widest dynamics of the motion (i.e., on leaflets' tip: at a certain time instant during the opening phase the beam could no more intercept the leaflet's surface and the beam is 'lost', not being reflected by the leaflet itself);
3) environmental conditions, because the valve is tested in a mock loop in presence of a fluid simulating blood viscosity, which has to be passed through by the laser beam together with the glass window allowing the optical access to the valvular function. A partial matching of refraction indices may contribute to further compromise the signal-to-noise ratio;
4) presence of other shifts in addition to the ones pointed out (vibrations of the whole system).

Moreover, the wide dynamics of leaflets' motion, together with the need of management of the acquisition timing (in order to clearly determine the exact instant of the closure impact, flow and pressure signals must be synchronously acquired) makes the measure critical, requiring a clear comprehension of the necessary requirements both for the acquisition software, and the

computational costs. The different approaches followed in the present study need to clarify if each of the two proposed experimental set-up is sufficient by itself to extract informative content from the recorded signals, or a more complex and expensive set-up is needed, in which a laser head has to be used as a trigger (a second laser beam is used to intercept the leaflet when it goes beyond the spatial position pointed by the beam itself).

Conclusions

A diagnostic of single valves could be made and risks and rates of failure for the devices could be predicted. Moreover, laser Doppler vibrometry may be used to examine nondestructively explanted mechanical heart valves, and the findings may be related to guidelines, technical reports, and other information to judge the risk of failure and its possible impact on valve design and clinical practice. The comparison of test results of preimplant and postretrieval valves (8), with respect to a reference stock of valves and materials, may be helpful in the definition of failure scenarios and risk analysis both for manufacturers and market surveillance bodies. Future aim is to verify if a non invasive measurement technique such as laser Doppler vibrometry could be applied for the preclinical evaluation of mechanical heart valves, and to assess the ability of this methodology to identify mechanical heart valve critical design features and manufacturing process steps that may be valve-related structural failure.

References

1. Drain L. *The laser doppler technique*. Chichester: John Wiley & Sons; 1980
2. Tomasini EP, Revel GM, Castellni P. Laser based measurement. In: *Encyclopaedia of vibration*. London: Academic Press; 2001. p.699-710.
3. Castellini P, Scalise L, Tomasini EP. Teeth mobility measurement: a laser vibrometer approach. *Rev Scien Instr* 1999;70(6):2850-5.
4. Revel GM, Scalise A, Scalise L. Measurement of stress-strain and vibrational proprieties of tendons *Meas Science Technol* 2003;14:1427-36.
5. Marassi M, Castellini P, Pinotti M, Scalise L. Cardiac valve prosthesis flow performances measured by 2D and 3D-stereo particle image velocimetry. *Exp Fluids* 2004;36:176-86.
6. Grigioni M, Daniele C, Romanelli C, Morbiducci U, D'Avenio G, Del Gaudio C, Barbaro V. Pathological patient in protocol definition for bench testing of mechanical cardiac support systems. *Int J Artif Organs* 2003;26:64-72.
7. Grigioni M, Daniele C, Del Gaudio C, Balducci A, Morbiducci U, D'Avenio G, Barbaro V. Critical aspects for a CFD simulation compared with PIV analysis of the flow field downstream a prosthetic heart valve. In: Arnez ZM, Brebbia CA, Solina F, Stankovski V (Ed.). *Simulations in biomedicine V*. (proceedings of the 5th International Conference on Computer Simulations in Biomedicine, Ljubljana, April 2003). Southampton: WIT Press; 2003. p. 271-280.
8. Cromheecke ME, Overkamp PJ, De Mol BA, Van Gaalen G, Becker A. Retrieval analysis of mechanical heart valves: impact on design and clinical practice. *Artif Organs* 1998;22:794-9.

COMPARISON BETWEEN STRESS PATTERN ANALYSIS BY FINITE ELEMENT METHOD AND STRESS MEASUREMENT BY THERMOELASTICITY ON MECHANICAL HEART VALVE

Jacopo Pirisinu, Gianluca Rossi
Dipartimento d'Ingegneria Industriale, Università degli Studi di Perugia, Italy

Introduction

The artificial heart valves are systems that control the blood flow, making possible the correct operation of the heart (1). From a structural point of view, the reliability is an important characteristic of this prothesis. For this reason the heart valves are more simple as possible from the mechanical point of view (1). A new FEM (Finite Element Method) is here developed, in order to test the previously presented measurement methodology (2) based on thermoelasticity that allow to perform stress measurements with a spatial resolution up to 22 μm by using a special infrared zoom.

A new finite element model of the mechanical heart valve

The artificial heart valve analysed is a mitralic heart valve (Bicer-val, by Carbomedics) illustrated in Figure 1. It has been studied with the development of a new finite element model, optimised using the information previously obtained. The external diameter of the valve is 31 mm. The external metal ring is realised by machining from one solid piece and the valve is therefore characterised by the absence of any soldering point.

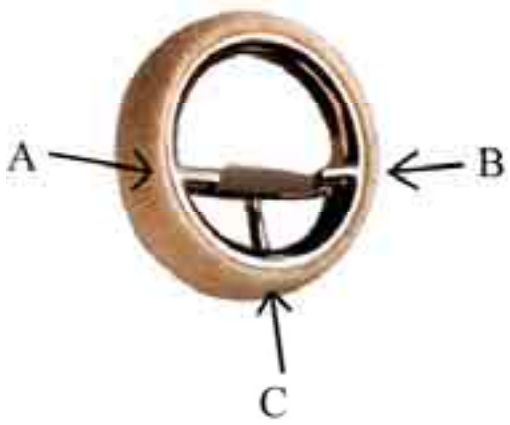

Figure 1. A picture of the heart valve analysed

In Figure 2 is shown the mesh of the FEM model of the ring.

The FEM model was realized using the ANSYS software.

The mesh density was increased, mainly in correspondence of the internal carbon disk supports illustrated in the point (A) of Figure 2.

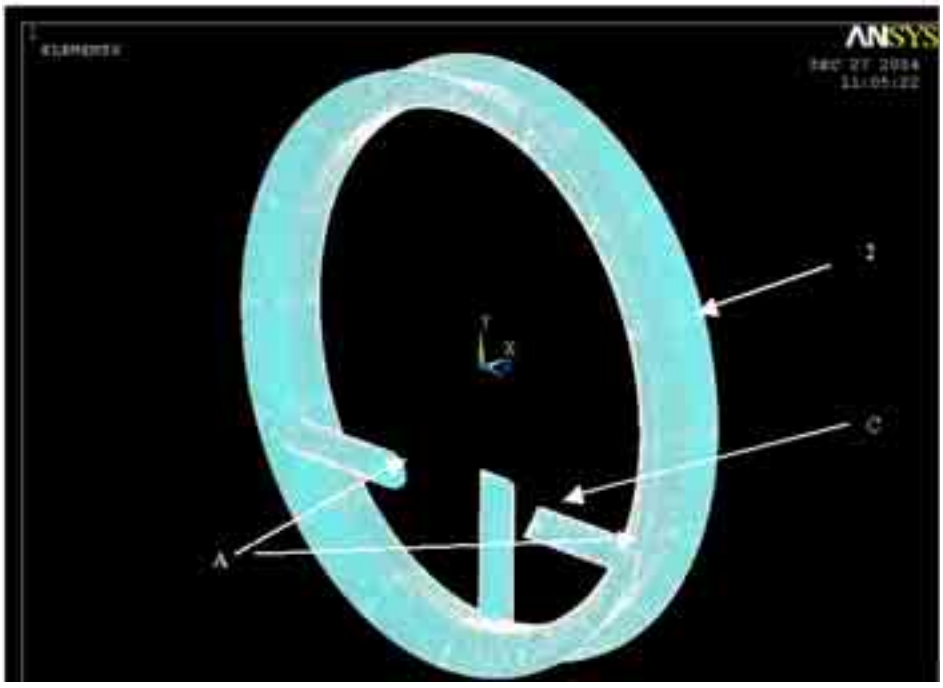

Figure 2. Mesh of the FEM model of the valve external ring

The external ring surface was fixed (2), by locking all the possible degrees of freedom, while in the free edge of the supports the displacement (on X axis direction, along the flow direction) was imposed. The displacements were previously measured during the experimental tests using a laser Doppler vibrometer (2).

As described in (2) the valve was loaded using an electrodynamic shaker, on the test bench, applying a sinusoidal force with frequency equal to 8 Hz and amplitude of about 10 N.

A typical result of the FEM simulation is illustrated in Figure 3. FEM codes do not give as output a stress distribution comparable to the results of a thermoelasticity measurement, that is in terms of the sum of the superficial principal stresses. This happens because the software used to calculate the stress on a single element that is three-dimensional.

A typical Von Mises stress distribution is illustrated in Figure 3 and it is expressed in MPa. It was therefore necessary to improve the FEM model by covering the pre-existing volume mesh with an infinitesimal thin skin, realized using shell elements. In this way it is possible to obtain the superficial stress on the component such as the thermoelastic measurement system allow to obtain.

The new improved FEM model and the new Fem result are shown in Figures 4 and 5.

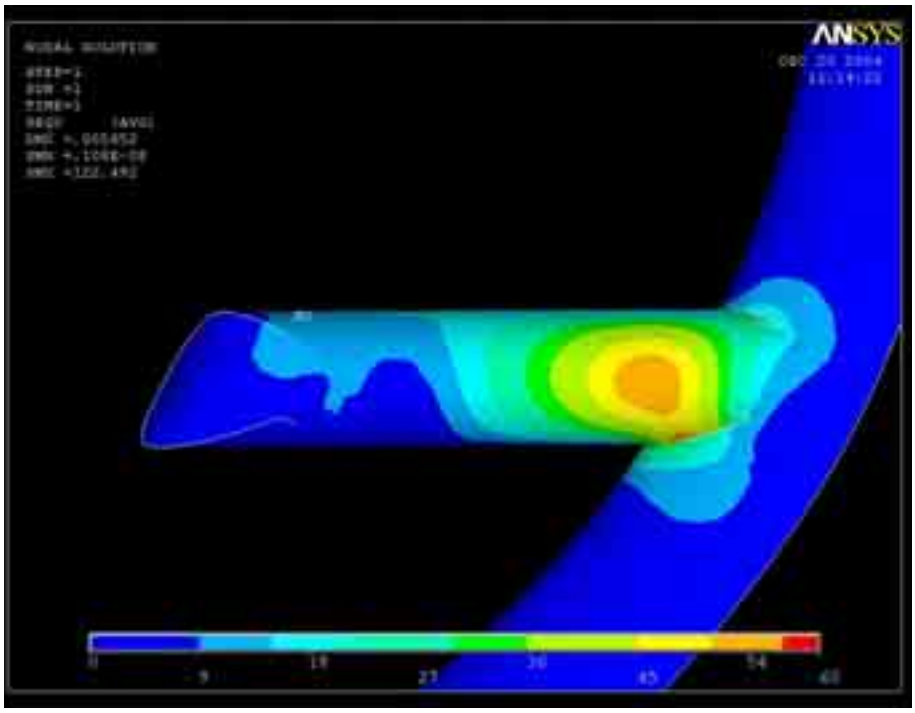

Figure 3. A typical FEM result

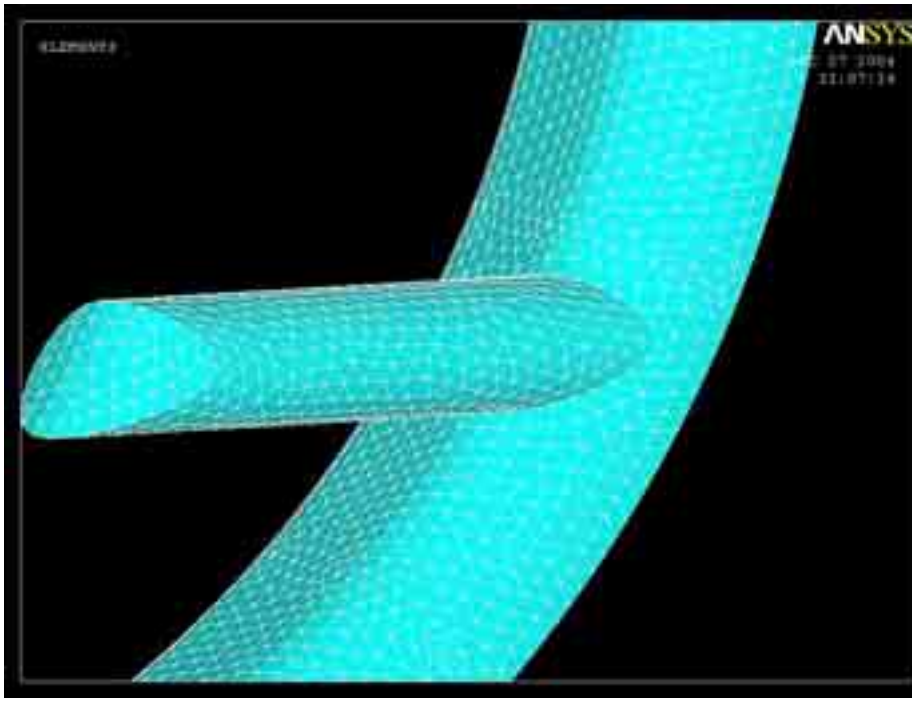

Figure 4. Shell added on the component

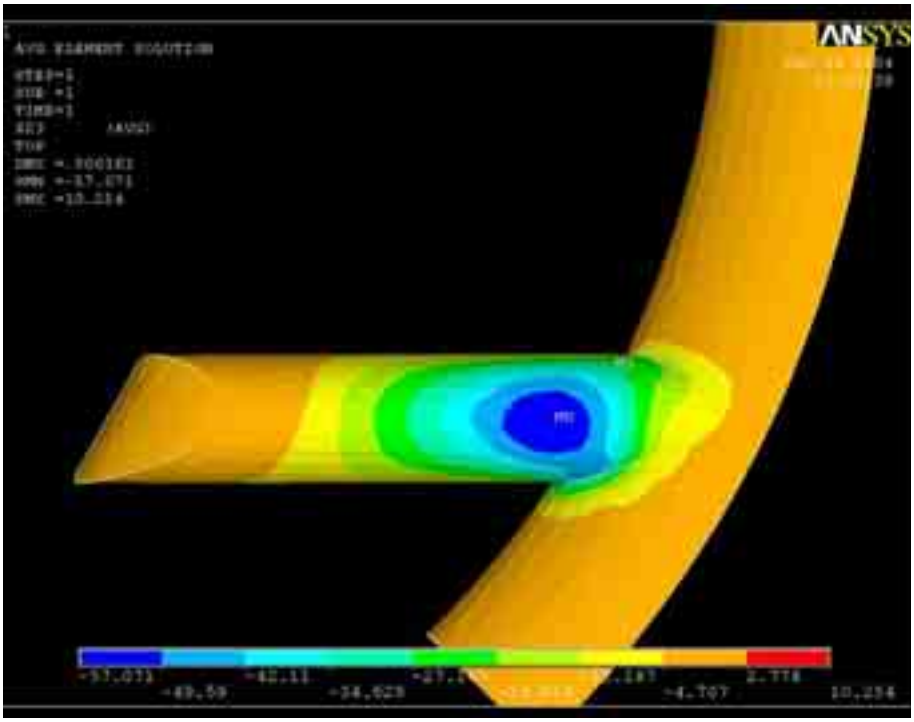

Figure 5. FEM results on the added shell

FEM: termoelasticity comparison

Thermoelastic Stress Analysis (TSA) is being used by engineers and scientists to solve since more than 10 years, many practical problems in structural and material design (4). The combination of infrared array detectors and advanced signal processing has made of the TSA a practical tool to characterize the performance of mechanical components, materials and structures. Thermoelastic stress analysis is based on the principle that when a solid is compressed its temperature increase, while decrease if the applied pressure is released. The following equation (1) describe the superficial temperature fluctuation with time (ΔT) on solid materials of the fluctuation with time of the sum of the principal stresses ($\Delta\sigma$) (4):

$$\Delta T = -\frac{\alpha T}{\rho C_p}(\Delta\sigma) \qquad [1]$$

where ρ is density, *Cp* is heat capacity at constant pressure, α is the thermal expansion coefficient and *T* is the ambient temperature. To detect the superficial stress field it is therefore necessary to measure the superficial distribution of temperature fluctuation with time of the mechanical component, cyclically loaded. In the following Figure 6 taken from (2), is shown one of the thermoelastic measurement performed on the valve cyclically loaded by using the exciter. These results put in evidence a very good qualitative correlation with the FEM model. Using a calibration factor between stress and temperature fluctuation, it is possible to obtain the stress maps expressed in MPa. It is also possible to obtain the sum of the principal stress profile

along a line, as illustrated in Figure 6. Same profiles of the sum of the principal stresses can be obtained from the FEM model by a proper data processing. A comparison is here illustrated in Figure 7.

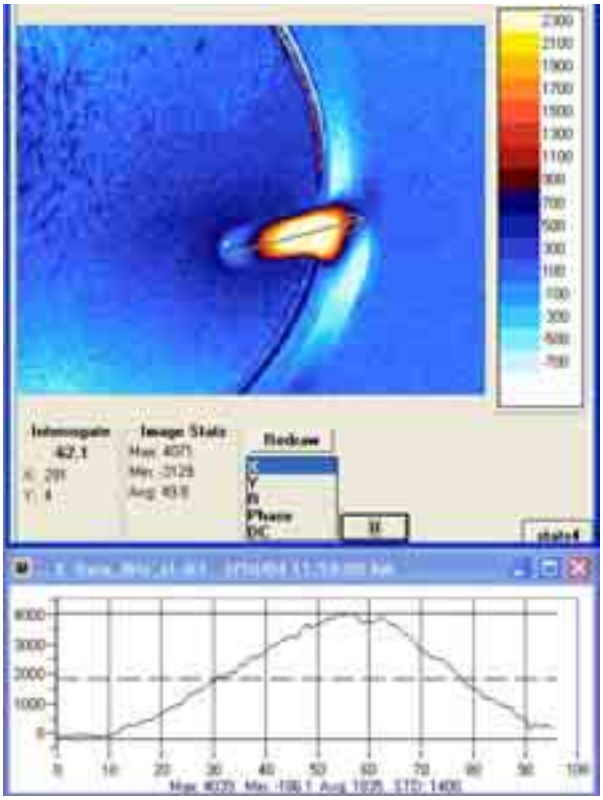

Figure 6. Thermoelastic stress analysis result

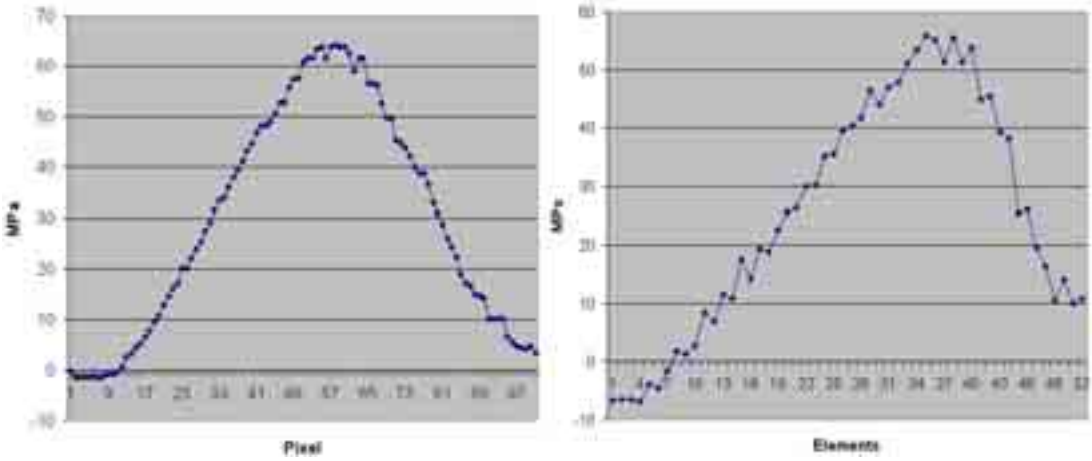

Figure 7. Comparison between thermoelasticity and FEM results

It is possible to see a different spatial resolution between the pixel of the thermographic system and the elements of the FEM model but the comparison show a very good agreement. Also in terms of maximum values the agreement is very good taking into account that the calibration factor here used is the general calibration factor for the steel (2) and does not consider the particular material (satellite alloy) and the type of the black paint used. The development of a technique to better define the calibration factor can be therefore an important development of this work.

Conclusions

In this paper a new measurement procedure for the analysis of stress fields on mechanical heart artificial valves has been validated by comparison with a FEM models. This procedure is based on the use of a thermoelastic non contact measurement system that allow to obtain the superficial stress pattern of a component cyclically loaded. The stress maps obtained by the FEM simulation pointed out a very good agreement, both qualitative and quantitative with the experimental data, opening new possibilities for the improvement of testing and design methods of artificial heart valves.

Acknowledgments

Authors would like to thank Mauro Grigioni (Dipartimento di Tecnologie e salute, Istituto Superiore di Sanità, Rome, Italy) for having provided the mechanical heart valve and its characteristics for the FEM modelling.

References

1. Abbot WM, Bouchier-Hayes DJ. The role of mechanical properties in graft design. In: Dardick H (Ed.). *Graft material in vascular surgery*. Chicago, IL: Year Book Medical Publishers; 1978. p. 59-78.
2. Rondini C, Rossi GL, Scalise L. Laser vibrometry and stress measurement by thermoelasticity on mechanical heart valve. In: *Proceedings of VI International Conference on Vibration Measurements by Laser Technique*, Ancona, 22-25/06/2004, SPIE Book 5503, Washington, USA
3. Akutsu T Kloff WJ. Permanent substitutes for valves and heart. *Trans Amer Soc Art Intern Organs (ASAIO)* 1958;4:230-5.
4. Harwood W, Cummings A, McKenzie K. *An introduction to thermoelastic stress analysis*. Bristol: Adam Hilger Publishing; 1991.

ACOUSTIC ANALYSIS TO INVESTIGATE CLOSING BEHAVIOUR OF PROSTHETIC HEART VALVES

Costantino Del Gaudio (a), Giovanni Pedrazzo (b), Umberto Morbiducci (a), Mauro Grigioni (a)
(a) Dipartimento di Tecnologie e Salute, Istituto Superiore di Sanità, Rome, Italy
(b) Analysa srl, Cuneo, Italy

Introduction

Mechanical heart valves are currently implanted for their characteristic features, such as low transvalvular pressure gradient and durability, which can assure an acceptable outcome for the patient, even if mechanical heart valve implant is not completely free of complications. Problems (e.g. leakage, mechanical failure, etc.) could arise, after implantation, without evident clinical warnings when complications have already occurred (1). This is a serious problem for patients undergone to prosthetic valve implantation whose clinical conditions must be continuously monitored. For this aim, a technique that could be adopted and that could guarantee an acceptable degree of discomfort for the patient, being not invasive, is represented by the spectral analysis of the valve sound: it is documented that the sound spectrum of malfunctioning prosthetic valves differs from that relative to normal ones (2): for mechanical heart valves the formation of a thrombus on the valve itself and its ring produces a shift of energy to lower frequencies, due to the altered way for the valve occluder to collide with the ring (3).

Several studies have been conducted in the past in order to investigate the clinical relevance of the acoustic analysis of the valvular sounds of prosthetic and native valves, both *in vivo* and *in vitro* (2, 4-6). However this methodology needs particular care in the interpretation of the results being affected by the specific pato-physiological conditions of each patient that could be result in a difficult attempt for a correct classification of the functionality of these devices.

This kind of considerations highlight the necessity to perform a detailed spectral analysis for each prosthetic valve, taking into account just the mechanical behaviour to put in evidence a characteristic pattern and to provide a comparison among several devices. For this aim the acoustic behaviour of three mechanical heart valves was analysed in a basic *ad hoc* set-up, implementing a time-frequency analysis, such as wavelet transform, which is suitable for investigating fast-varying signals (7) like the ones acquired during the functioning of these medical devices, especially in the closing phase. This seems to be the preliminary step for evaluating the frequency pattern of each valve in order to reconstruct, as the final goal, a sort of "fingerprint" to classify and to discriminate the degree of functionality of an implant.

Materials and methods

Experimental set-up

Three mechanical heart valves (27 mm tissue annulus diameter) were analysed to measure acoustic signals during working conditions; the present study is based on the investigation of relative energy differences of two bileaflet valves (Carbomedics, CM; St Jude HP, SJ) and one tilting valve (Bjork-Shiley, BS).

Mechanical heart valves have been mounted in *ad hoc* set-up composed by two chambers in communication by means of the valve under test; one of the two chambers is at atmospheric pressure reference, while the other is pressurized by the control pressure waveform that impose the opening and the closing of the valve. The fluid used for this experimentation was distilled water. The command waveform was a square wave with a duty cycle of 50% and a frequency of 1 Hz (60 bpm) which imposed the closure of the leaflets under a peak pressure of about 120 mmHg. Simultaneous measurements were made of the driving pressure waveform and of the acoustic signal of the valve during each cycle. The acoustic signal, detected by means of a hydrophone (Reson, Inc.) and high-pass filtered at 20 Hz, and the square command waveform were sampled at 51.2 kHz for about 120 s.

Data analysis

Owing to the square command waveform, the hydrophonic signal was segmented to identify each temporal period determined by a valve closing and opening event. Focussing the investigation on the valve closing signal to evaluate a mean characteristic closing signal for the mechanical prosthesis under study, a cross-correlation operation was performed among the several closing signals. This operation was necessary due to the independency of each valve signal giving a slight temporal shifting for a closing signal with respect to the other ones; extracting an average closing signal without cross-correlating these specific patterns would result a meaningless operation.

Signal processing

As reported in Sheng (7), the Fourier spectrum analysis is global in time and is basically not suitable to analyse non-stationary and fast varying signals: the Fourier transform does not provide any information about the temporal evolution of spectral characteristics of the signal itself. To analyse the closing signal of prosthetic heart valves, normalized with the relative root mean square value, the Short Time Fourier Transform (STFT) was implemented, according to the following definition (7):

$$S_f(\omega,\tau) = \int_{-\infty}^{\infty} f(t)g^*(t-\tau)e^{-j\omega t}dt \qquad [1]$$

where *f(t)* is the signal under investigation, *g(t)* is a square integrable short-time window, with fixed width, shifted along the time axis by a factor τ and * is the complex conjugate.

However, also STFT presents drawbacks associated to the choice of the window, of fixed width, to analyse the signal: once the window has been chosen, the time and frequency resolutions are fixed over the entire time-frequency plane (7). Thus for this study, the Wavelet Transform (WT) was adopted as well, which is local in both time and frequency domains.

Continuous wavelet transform of a signal *f(t)* is defined as:

$$W_f(s,\tau) = \int_{-\infty}^{\infty} f(t)h^*_{s,\tau}(t)dt \qquad [2]$$

where $h_{s,\tau}(t)$ is a set of basis functions (wavelets) and * is the complex conjugate (7). However the continuous wavelet transform could be highly redundant; in order to have an efficient signal representation with a limited set of parameters the discrete transform is implemented, generally built up with orthogonal dyadic functions (8). The corresponding discrete wavelet can be expressed as:

$$h_{i,k}(t) = 2^{-\frac{i}{2}} h(2^{-i}t - k) \qquad [3]$$

where *i* and *k* are integers.

Operatively the acquired signals were decomposed in ten levels by means of the wavelet function Daubechies 7; the coefficients derived from this decomposition are successively implemented to reconstruct the so-called detail signals. The signal is decomposed at each scale into its details and approximation by means of high-pass and low-pass filters respectively and downsampled (9); according to this procedure polynomial trends are automatically removed from the details, whose frequency bandwidth is defined in the range

$$2^{-(j+1)} f_s < f < 2^{-j} f_s$$

where f_s is the sampling frequency and *j* the decomposition level. Acoustic energy for each mechanical valve was computed by adding together the corresponding square wavelet coefficients, according to the following relationship:

$$E_j = \sum_k c_{j,k}^2$$

where *j* represents the level of signal decomposition (2); the total energy of the signal can be obtained by:

$$E_{TOT} = \sum_j E_j \ ;$$

then the normalized energy (relative wavelet energy) is computed as $p_j = \frac{E_j}{E_{TOT}}$.

Results

The result of STFT for the closing signal of the SJ valve is reported in Figure 1.

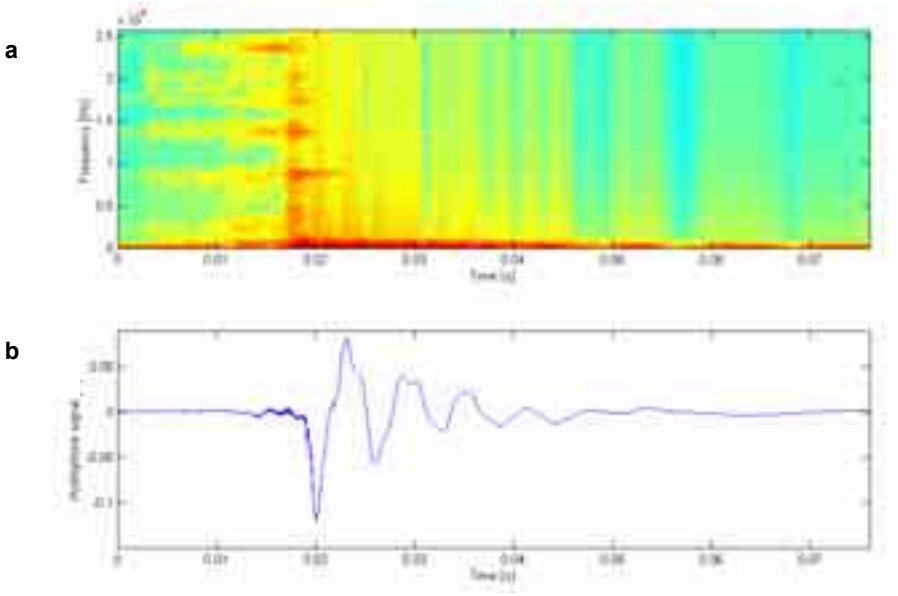

Figure 1. STFT analysis (a) for the closing signal of the SJ valve (b)

The temporal evolution of the average spectral pattern for the three mechanical valves is reported in Figure 2: bileaflet valves showed a similar behaviour, in terms of morphology and amplitude, while the spectral pattern for the BS valve highlighted two peaks that can be explained considering a first impact of the occluder onto the legs structure of the valve and then the closing impact of the occluder onto the housing ring.

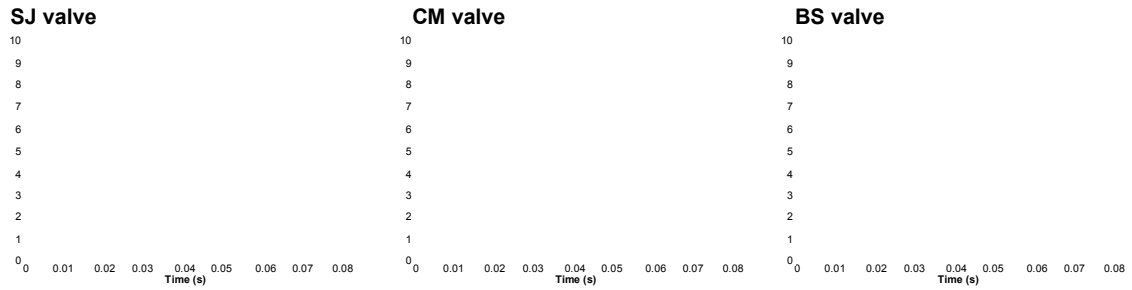

Figure 2. Temporal evolution of the acoustic spectral pattern calculated by means of STFT for the three investigated mechanical heart valves

The implementation of the multiresolution analysis produced the signal decomposition presented in Figure 3 for the SJ valve. In Figure 4 the relative energy for each frequency sub-band, for all the investigated mechanical valves, is reported. The preponderant amount of relative energy is concentrated in the band 100-200 Hz (BW3) showing the highest amplitude for the CM. The BS valve presents higher relative energy starting from 400 Hz, showing how this particular prosthetic device highlights a spectral content more distributed with respect to bileaflet valves.

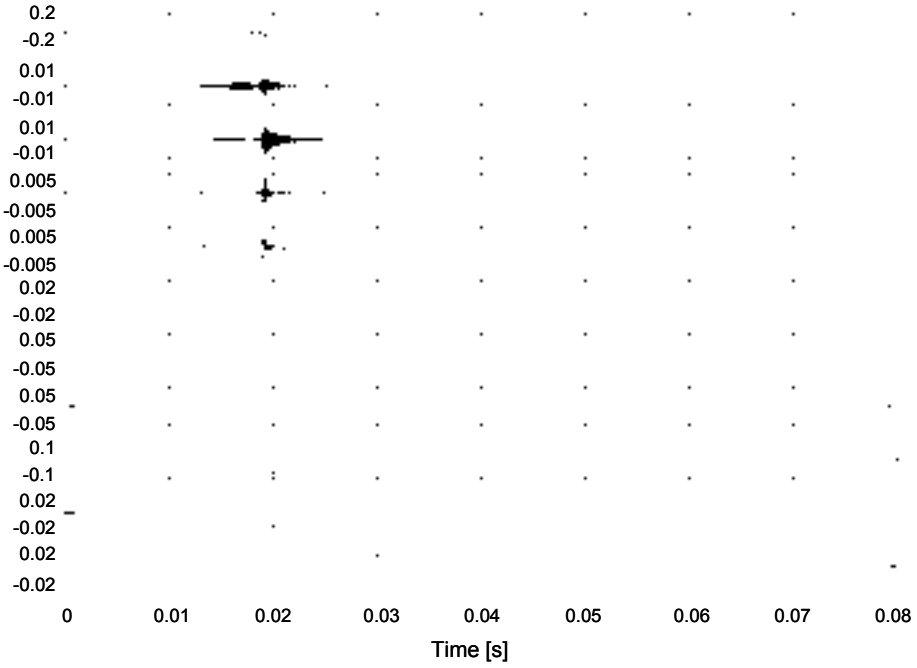

Figure 3. Wavelet decomposition for the closing signal of the SJ valve

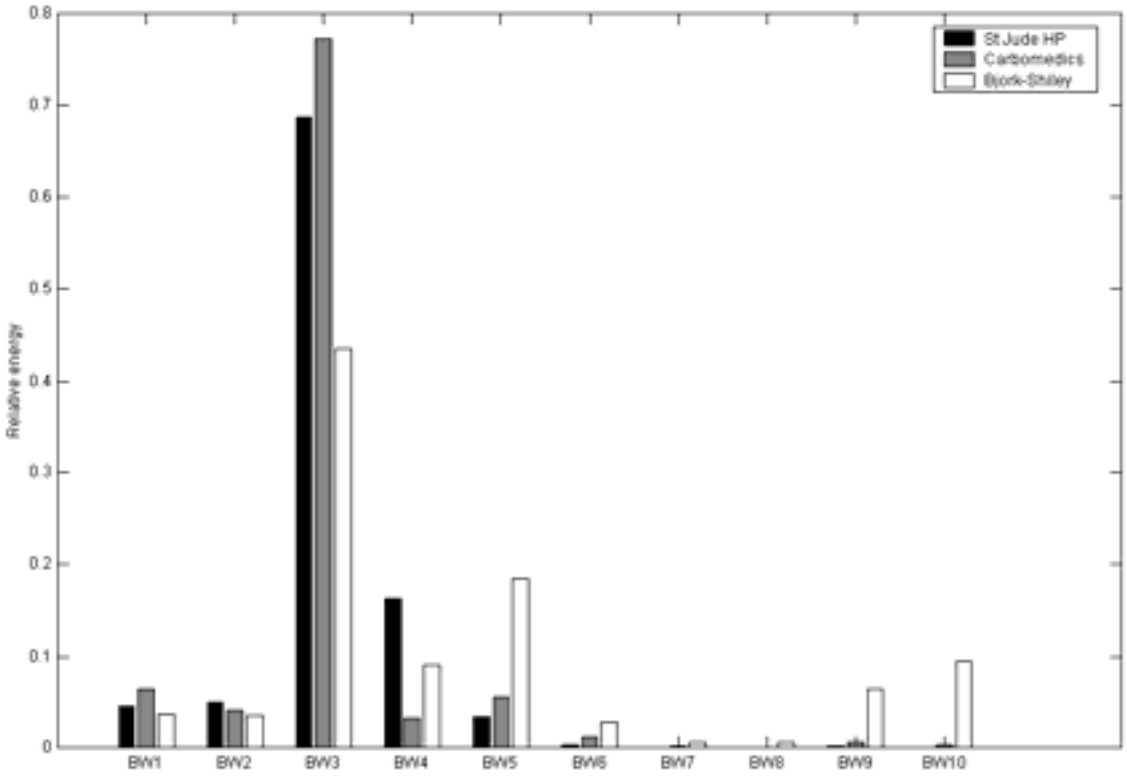

Figure 4. Relative energy for the decomposed acoustic signals by means of WT for the three investigated mechanical heart valves

Discussion

Acoustic signal analysis of mechanical heart valves represents a relevant investigational field for several reasons; this approach, currently under study, has the potentiality:

i) to highlight minimal changes in mechanical valve function (1);

ii) to states the degree of discomfort for an implanted patient, due to the level of the acoustic energy characteristic for each prosthetic valve during the closing phase;

iii) to be implemented as a routinely monitoring technique, once reached a certain level of confidence in evaluating the acoustic behaviour of these prosthetic devices.

The study here proposed aimed to investigate in a comparative way three mechanical heart valves (two bileaflet and a tilting one) in a pneumatic driven set-up with a basic waveform (e.g., a square waveform) which is typically a test signal for evaluating the dynamic response of an engineering system. Due to the strong impulsive nature of this kind of signals, a proper analysis technique is required; the wavelet methodology here adopted represents the most suitable choice for this aim, not suffering of particular limitations as for the STFT, in which the choice of the window for the signal analysis determines the spectral resolution (7).

The results obtained from the implementation of WT have shown that a consistent part of the relative acoustic energy is concentrated in the 100-200 Hz frequency band for the three

mechanical valves under study and that the BS valve has higher relative energy for frequencies superior to 400 Hz. Moreover, the BS valve has higher relative energy than the CM valve in the BW4 frequency band (200-400 Hz); this result shows a good agreement with previous findings (6), where the closing sound of implanted BS valves presented more energy beyond 250 Hz than the CM valves.

Acknowledgment

A special thanks to Giovanni Calcagnini for the critical discussion about the methodologies of signal analysis implemented for this study.

References

1. Eitz T, Fritzsche D, Grimmig O, Frerichs I, Frerichs A, Hellige G, Minami K, Korfer R. Acoustic phenomena and valve dysfunction in cardiac prostheses: data acquisition and collection via the Internet. *J Heart Valve Dis* 2003;12(4):414-9.
2. Masson C, Regis R. Time-frequency analysis of the noise produced by the closing of the artificial heart valves: an in vitro study. *Med Eng Phys* 1998;20:418-31.
3. Köymen H, Altay BK, Ider YZ. A study of prosthetic heart valve sounds. *IEEE Trans Biomed Eng* 1987;34(11):853-63.
4. Nandagopal D, Mazumdar J, Bogner RE, Goldblatt E. Spectral analysis of second heart sound in normal children by selective linear prediction coding. *Med Biol Eng Comput* 1984; 22:229-39.
5. Picard D, Chara J, Guidoin R, Haggag Y, Poussart D, Walker D, How T. Phonocardiogram spectral analysis simulator of mitral valve prostheses. *J Med Eng Tech* 1991;15(6):222-31.
6. Sava H, McDonnell JTE. Differences in spectral composition between monostrut Bjork-Shiley and Carbomedics valves implanted in the aortic position. *Med Biol Eng Comput* 1995; 33:689-94.
7. Sheng Y. Wavelet transform. In: Poularikas AD (Ed.). *The transforms and applications handbook.* Florida: CRC Press; 1996. p. 747-827.
8. Akin M. Comparison of wavelet transform and FFT methods in the analysis of EEG signals. *J Med Syst* 2002;26:241-7.
9. Wiklund U, Akay M, Morrison S, Niklasson U. Wavelet decomposition of cardiovascular signals for baroreceptor function tests in pigs. *IEEE Trans Biomed Eng* 2002;49:651-61.

TESTING REQUIREMENTS FOR STEROSCOPIC PARTICLE IMAGE VELOCIMETRY MEASUREMENTS OF MECHANICAL HEART VALVES FLUID DYNAMICS

Umberto Morbiducci, Giuseppe D'Avenio, Costantino Del Gaudio, Mauro Grigioni
Dipartimento di Tecnologie e Salute, Istituto Superiore di Sanità, Rome, Italy

Introduction

The analysis of the fluid dynamics of implantable mechanical devices is the most important instrument both for the comprehension of the functionality and the investigation of some peculiar features of these devices in order to reach a higher degree of performance and subsequently to assure a better clinical outcome for the patient. A relevant remaining problem for any device or system in contact with blood are blood damage and thrombus formation. In particular, the case of prosthetic heart valves, in terms of the evaluation of their performances in replacing the diseased native valves. Critical aspects remain in the post-implantation stage, relied to the damage on red blood cells when the induced mechanical stresses overcome a certain threshold (1, 2). The downstream fluid dynamics of most heart valves are well described in the literature, but it is still worthwhile to improve and clarify the minimal requirements criteria in the application of the current techniques. A very powerful technique for experimental fluid dynamics is Particle Image Velocimetry (PIV). PIV (3) is essentially a multipoint measurement technique that allows full-field measurement of instantaneous velocity vectors in a flow field, thus allowing us to map the entire velocity or stress field over the aortic root. PIV is routinely used by flow researchers and medical device manufacturers to provide two-dimensional mapping that can identify disturbed flow patterns. As such, it provides a powerful tool for studying the safety and efficacy of flow-related devices. However, being the flow field downstream of a prosthetic heart valve fully three-dimensional, stereoscopic PIV which measures the real three dimensions of the fluid velocity field, seems to be eligible to be a gold standard in the evaluation of implantable medical devices fluid dynamics. Three-dimensional PIV (4, 5) is based on the same fundamental principle as human eyesight, i.e., the stereoscopic vision: slightly different images are captured by the eyes and, from the comparison of these two images, the brain derives a three-dimensional interpretation. Stereo PIV, with each one of the two cameras playing the role of an "eye", measures displacements rather than actual velocities (as 2D PIV does). The accuracy in the determination of the out-of-plane component is related to the angle between the two cameras: the larger this angle, the more accurate is the determination of the out-of-plane displacement (with a restricted optical access, a smaller angle must be used, and a cost of accuracy in determining the third velocity component must be paid). The actual stereo measurements begin with conventional 2D PIV processing of simultaneous recordings from the two cameras. This produces two 2D vector maps showing the instantaneous flow field as seen from each of the cameras. Using a calibration procedure, the points in the chosen interrogation grid are now mapped from the light sheet plane and onto the left and right image planes. With a two-dimensional displacement seen from both left and right camera estimated at the same point in physical space, the true 3D particle displacement can be calculated by solving the equations obtained in the calibration. It follows that a correct stereo PIV calibration is an essential prerequisite for an accurate measurement of the three components of the velocity

vector field in the investigated flow domain. In the optics of an application of stereo PIV technique as a reliable measurement solution for the complete analysis of prosthetic heart valve flows, several methodological and technological problems must be tackled. Therefore, the main focus of the present study is the suggestion of essential testing requirements for *in vitro* Stereo PIV measurements of mechanical heart valves fluid dynamics in a commercial mock circulatory loop.

Materials and methods

The measurements involved the use of the Sheffield University-developed Pulse Duplicator (PD), appropriately modified, reported in Figure 1. The blood-analogue solution flows in the system in the counterclockwise direction. The PD allows optical access to the aortic flow. Suitable modifications, showed in Figure 1, have been designed and realized to enhance this feature and enable optimal recordings of particle images. In particular, suitable Perspex-made windows have been built to enable normal imaging of the flow by the two cameras, in the stereo-PIV configuration. The PD was firstly selected in order to realise an experimental set-up particularly suited for LDA studies because (6), having separate chambers for aortic and mitral positions, the influence between the two valve flows is minimised; in such a way it is possible to study the flow downstream of each valve with standard plug flow entering the valve. The ventricular function is simulated by means of a suitably controlled piston, at various cardiac outputs and heart rates. Pressures are sampled at opposite sides of the tested valve. In the aortic section of the PD, a particular attention was employed in the anatomic reconstruction of the aorta. An aortic root was glassblown according to data desumed from an angiographic study found in literature (7). A Delrin-made coupling system on the PD presses the blown-glass aorta towards the valve sewing ring, maintaining a central alignment of the former. The valve is thus fixed by mechanical compression of the sewing ring; in this way sealing is assured without any valve function impairment.

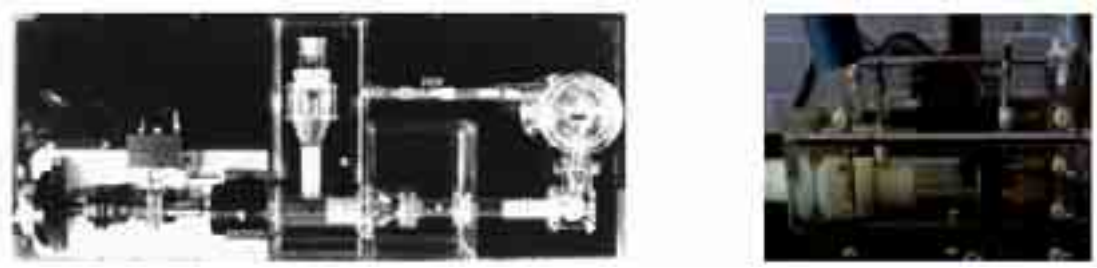

a b

Figure 1. Experimental set-up: overview of the pulse duplicator (a) and sketch of thr aortic site (b)

All tests were carried out at a pulse rate of 70 beats/min, with the systolic period spanning the 35% of the entire cardiac cycle. The cardiac output was set at 5 L/min. The given test conditions are in accordance with FDA Replacement Heart Valve Guidance. A suitable solution of glycerol, water and sodium iodide was employed in the measurements. The refractive index of the solution is 1.473, the same as glassblown aorta, made of Pyrex glass (when there is not internal tension). Viscosity measurements with a Cannon-Fenske routine viscometer confirmed

that the solution had a viscosity similar to that of blood at high shear rates (3.7 cSt). The prosthetic heart valve used in the measurements was the 27mm total annulus diameter sized SORIN Bicarbon, which has curved leaflets. For 3D measurements, 105mm Nikon lenses were used in the recordings. Owing to the characteristics of the Scheimpflug configuration, the depth of field was certainly sufficient to have a uniformly focused image. A 150 mJ/pulse Q-switched double-head laser was used to illuminate the seeding particles. The temporal shift dT was chosen in order to have a maximum displacement between particles less than a quarter of the interrogation window size (8). At the same time, care was taken to choose dT to warrant that the displacement between particles was generally greater than a particle diameter. In the 3D stereo-PIV configuration, cameras were inclined by 30 degrees with respect to the vertical, in the plane normal to the valve axis. Then, the angle formed by the axes of the two cameras was 60 degrees. The Scheimpflug configuration enabled to maintain the focus throughout the image plane. The threshold for the peak-to-noise SNR was chosen equal to 1.2, as a reasonable value for having a sufficient yield of the velocity calculations from particle images. The commercial software used, i.e. Insight 5.0 (TSI), was subjected to preliminary tests that gave the results for the time of evaluation of a 3D flow field of 45 s approximately. Actually, these results have proven to be a lower bound for the computation time necessary to analyze the particle images. It was found that the performance of the system degraded continuously during the batch analysis of image files, due probably to the interplay between commercial software and the underlying operating system, which can have an important role in the determination of the required computation times. The analysis hereby presented refers to N=300 fields per cycle phase and scanning plane. It must be underlined, though, that measurements involving up to N=1000 velocity determination per cycle phase and scanning plane have been carried out, in order to investigate about the statistical significance of the size of the data set. The storage cost for the analysis carried out, being each recorded image 2.5 MB, is in the order of 350 GB. A positioning stage for both stereo camera and laser sheet was built *ad hoc*. The precise positioning of the laser sheet is enabled by a target with a crosshair on one face, at the height of the valve axis. The illumination of the marker with the laser at low pulse energy enabled to check that the reference point (z=0) was the same during the measurements. Each different plane at z= constant implied a slight manual refocusing of the image(s), since the proportion of the optical paths in the air and in the liquid phase was different at each z value. Nevertheless, the adjustment was always very small. For each plane at z=constant, a number of timing points (TP) was chosen as the most indicative for the analysis. The timing points are indicated in Table 1.

Table 1. Timing points investigated in the cardiac cycle

Timing pt no.	Temporal distance from systolic peak (ms)
1	-45
2	-30
3	-15
4	0
5	15
6	30
7	45
8	145
9	205
10	235
11	280
12	500

In Figure 2, the scanning planes are reported, in relation to the geometry of the valve (the circle represents the valve's internal orifice) and the aorta (the section at the maximum span of the sinuses of Valsalva is shown). The valve is seen from the inflow side. The planes at z=0, 3, 6, 9 and 12 mm were considered in the 3D measurements. It is common to adopt a completely empirical approach for stereo PIV calibration by placing a planar target built up with a regularly spaced grid of marks at the position of the light sheet and moving the target by a specified amount in the out-of-plane direction to two or more z-positions (9). At each z-position a calibration function with sufficient degrees of freedom is mapping the world xy-plane to the camera planes, while the difference between z-planes provides the z-derivatives of the mapping function necessary for reconstructing the three velocity components. This empirical approach has the advantage that all image distortions arising from imperfect lenses or light path irregularities e.g. from air/glass/water interfaces are compensated automatically in one step. The calibration of the 3D PIV system was carried out using the PIV software, together with the calibration software supplied with.

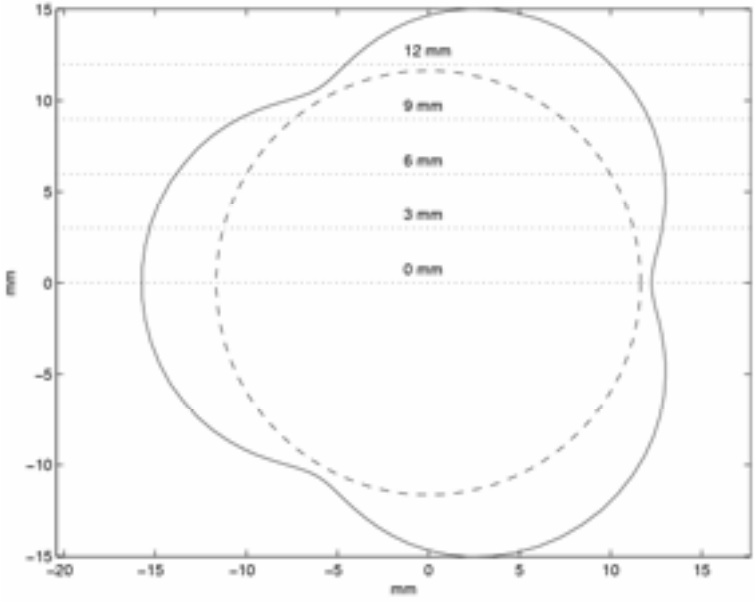

Figure 2. Sketch of the longitudinal planes investigated

The calibration or mapping process uses a calibration target, which is a rectangular grid of marker points with known (x, y, z) locations. The target is mounted on a traverse, or a target with two planes is used without traversing, and positioned in the fluid. The latter option was chosen for the measurements at ISS premises, due to the difficulty in traversing a target in the small and not easily accessible space available to the flow.

The target was placed directly in the fluid, after removal of the glassblown aorta. Since the homogeneity of the glass and the matching of refractive index between the aorta (n=1.473) and the fluid, this procedure was sufficient to calibrate the stereo camera of the 3D PIV system. The distance between the two planes of the target was Δz=0.5 mm. Each dot of a 7x7 rectangular grid (5 mm spacing) was relative to one of the two planes, in an alternate fashion (along each diagonal, the z coordinate was the same). The light sheet was aligned midway between the two target planes. The initial step of the procedure consisted of recording the calibration images, that is, capturing and saving a set of images of the calibration target that can be analyzed and used as

data points for the calibration file. For 3D operation, pairs of left and right images are captured and stored. With the two-plane target only one set of calibration images is used. In order to have satisfying results, the cameras were focused on the lightsheet plane, then the target was positioned in the field of view of the cameras, using a large f-number to have a sufficient depth of field for having the two plane in focus. Once the calibration images over the range of the lightsheet thickness are acquired, a set of calibration points filling the entire measurement volume is collected to build up the mapping functions. For each camera, six polynomial equations can be found by a least squares method, i.e., three fluid-to-image-mapping functions, and three image-to-fluid-mapping functions. The calibration process removes the sub-pixel accuracy requirement in the two cameras alignment: in fact, even in presence of a perfect alignment, the image perspective from the two cameras causes the rest of the pixels not to image the same point in the fluid domain. The local magnification for each vector in the left and right images can be found using the derivatives of the mapping functions, which represent the gradient of particle image displacement to fluid displacement. These gradients represent the amount of particle image displacement, in pixels, in the *X* or *Y* direction that is caused by a *1* mm particle displacement in the *x*, *y*, or *z* direction in the fluid. The three-dimensional particle displacement is computed by combining interpolated pixel displacement vectors from the left and right cameras using the calibration gradients to convert from pixel displacement to world displacement. The vector grid is defined as a square grid in the fluid coordinates. This world location is mapped into the left and right cameras using the calibration mapping functions. Bilinear interpolation is used to estimate the pixel displacement at that location from the four surrounding vectors.

Results

An example of the results obtained in the conditions previously described is shown in Figure 3.

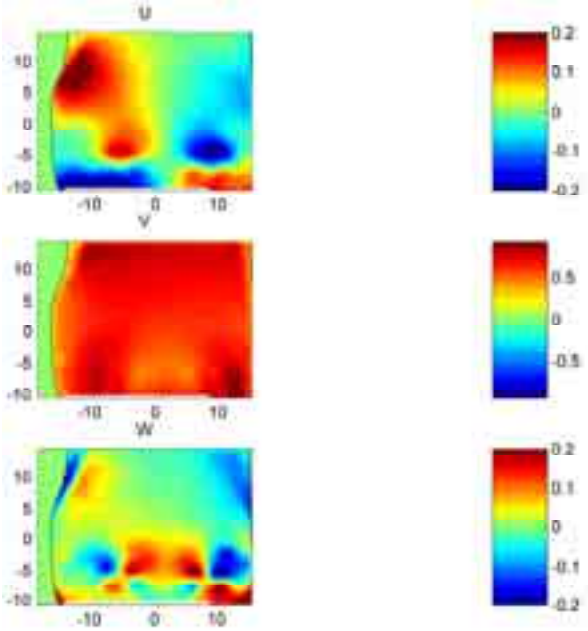

Figure 3. Map of the velocity components (m/s) at peak systole, in the midplane

From the colorimetric maps of velocity (in m/s) components several typical features of the bileaflet valves are to be noted.. The axes of the colorimetric maps represent distances (in mm) in the relative light sheet plane; the ordinate (Y) is the axial direction (aligned with the main flow) and the abscissa (X) is the in-plane transversal direction. The valve is placed at the bottom part of each Figure, and the main flow is directed upwards. Occasionally, low SNR conditions have prevented the determination of the local velocity, so that the relative region of the flow field has been left blank. The median plane of the flow is a plane of symmetry, taking account of both valve structure and glassblown aorta. Nevertheless, the tests at a CO of 5 L/min suggest that there are remarkable three-dimensional effects even in this plane. In Figure 3, for instance, the velocity average along the axial (V) and transversal (W) direction are shown, at the phase of peak systole (timing point no. 4).

The color map indicates the velocity value, in m/s. Two dips in velocity value are obtained at the location of the leaflets. These are the wakes downstream the leaflets which, in the case of this sample, are very short with respect to the flat leaflet design. Two high velocity regions are detected laterally to the leaflets, where the higher velocity vectors are in the right-side region towards the aortic annulus wall. In fact there is much more space at disposal for the flowing jets on the left side (sinus of Valsalva) where the mixing region is governed by slow moving 3D vortex (see also LDA measurements (10)). Depending on the color table selected the whole central region could allow us to view the quality of the three jets typically exiting from a bileaflet valve. What it is relevant in the presented Figure is the acceleration in the final location of the sinuses regions where the flow jets reattach themselves to the wall with the higher velocities on the left side of the aorta due to the narrowing of the space available for the flow, while a more plug-flow-like profile is built up in the tube section of the represented ascending aorta inflow section. However in term of 3D measurements a particularity of the flow fields must be highlighted. The 3D analysis underlines possible limitations of the more common two-dimensional PIV measurements, with regard to complex biomedical applications whose related flow field is fully three-dimensional.

Discussion

Full-field measurement of instantaneous velocities in the flow field of mechanical artificial heart valves is vital as the flow is unsteady and turbulent. Biological flows are almost always strongly unsteady, so one has to perform phase - averages to completely describe the flow field. In order to have a good representation of the flow field, it would be sufficient to have a temporal resolution in the order of 10 ms, resulting in a total of about 40 time steps or phase angles (forward flow phase through a heart valve is typically in the order of 400 ms). Moreover, to approach with method the problem of the sample size to be used for the achievement of an accurate statistics, the acquisition of a great number of images is required per measurement plane and phase angle. The choice made by the authors, i.e., 300 images per phase angle, 5 measurement planes, 12 time instants, is, in their experience, a minimal ‘safety’ requirement to be fulfilled, from a methodological point of view, in order to propose stereo PIV technique as a measurement solution for a deep and complete analysis of heart valve substitutes’ fluid dynamics in a commercial mock circulatory loop (high computational and storage costs for a stereo PIV analysis to be carried out). In the experience of the authors, the possibility to have great modularity and manoeuvrability is considered particularly useful from a validation point of view. Several problems arise due to the fact that with commercial mock loops, it is not guaranteed the possibility to configure the set-up in order to attain an angle of 90° between

probes' axes, without image deformations. The results shown before represent a novelty in the *in vitro* determination of flow past the artificial valves.

References

1. Barbaro V, Grigioni M, Daniele C, D'Avenio G. A discussion on the threshold limit for hemolysis related to Reynolds shear stress. *J Biomech* 1999;32:1107-12.
2. Lim WL, Chew YT, Chew TC, Low HT. Pulsatile flow studies of a porcine bioprosthetic aortic valve *in vitro*: PIV measurements and shear-induced blood damage. *J Biomech* 2001;34(11):1417-27.
3. Adrian R. Particle-imaging techniques for experimental fluidmechanics. *Ann Rev Fluid Mech* 1991;23:261-304.
4. Prasad AK. Stereoscopic particle image velocimetry. *Exp Fluids* 2000;29:103-16.
5. Prasad AK, Adrian RJ. Stereoscopic particle image velocimetry applied to fluid flows. *Exp Fluids* 1993;15:49-60.
6. Grigioni M, Daniele C, D'Avenio G, Barbaro V. The influence of the leaflets' curvature on the flow field in two bileaflet prosthetic heart valves. *J Biomech* 2001;34(5):613-21.
7. Reul H, Vahlbruck A, Giersiepen M, Schmitz-Rode TH, Hirtz V, Effert S. The geometry of the aortic root in health, at valve disease and after valve replacement. *J Biomech* 1990;23(2):181-91.
8. Keane RD, Adrian RJ. Optimization of particle image velocimeters. Part I: Double pulsed systems. *Meas Sci Tech* 1990;1:1202-15.
9. Soloff SM, Adrian RJ, Liu ZC. Distorsion compensation for generalized stereoscopic particle image velocimetry. *Meas Sci Technol* 1997;8:1441-54.
10. Barbaro V, Grigioni M, Daniele C, D'Avenio G, Boccanera G. 19 mm sized bileaflet valve prostheses' flow field investigated by bidimensional laser Doppler anemometry (part I: velocity profiles)'. *Int J Artif Organs* 1997;20(11):622-8.

FLOW VISUALIZATION BY BUBBLES GENERATION

Antonello Delogu, Costantino Del Gaudio, Umberto Morbiducci, Giuseppe D'Avenio, Vincenzo Barbaro, Mauro Grigioni
Dipartimento di Tecnologie e Salute, Istituto Superiore di Sanità, Rome, Italy

Introduction

Fluid dynamics analysis of implantable medical devices, such as prosthetic heart valves and vascular stents, represents a relevant topic to asses on the safe nature of these devices taking into account that the non-physiologic local haemodynamics could be responsible for possible damage to blood cells or to vascular endothelium (1, 2). Several investigators have dealt with this problem by means of experimental and numerical techniques, e.g. particle image velocimetry, laser Doppler anemometry (3, 4) and bubble flow visualization (5); in particular the latter methodology is one of the oldest methods of flow visualization (6), based on electrolysis reaction inside the flow itself.

In this study a basic experience of bubble flow visualization in a glass cyndrical duct in pulsatile regime was built up in order to highlight the typical velocity pattern under laminar conditions.

Materials and methods

Bubble flow generation: basic concepts

Considering an aqueous solution of sodium chloride, the generation of gas bubbles is made possible by the flowing of an electrical current inside the solution itself. Electrolysis of aqueous NaCl solutions gives a mixture of hydrogen and chlorine gas and an aqueous sodium hydroxide solution.

The chemical reactions that take place at the electrodes during electrolysis are the following:

$2H_2O+2e^- = H_2+2OH^-$ (reduction of water at the cathode)
$2Cl^- = Cl_2 + 2e^-$ (oxidation of chlorine at the anode)

According to Faraday's laws, the amount of a substance consumed or produced at one of the electrodes in an electrolytic cell is directly proportional to the amount of electricity that passes through the cell; consequently, the amount of bubbles is proportional to the current flowing through the electrodes.

Advantages of this method of visualization are:

- timing of bubbles generation can be controlled (it is therefore possible to carry out the synchronization of the generation of the bubbles with an external event);
- the amount of generated bubbles can be controlled; depending on the parameters relative to the flow in observation (speed of the flow, area of the section in examination), it is possible to increase or to diminish the amount of bubbles to obtain the optimal visualization;
- the shape of generating electrode is arbitrary; a particular flow geometry can request different electrode shape.

Some disadvantages are:
- the electrodes must be located inside the solution, which, in some cases, can be difficult to realize;
- a connection between the electrodes (which are located inside the solution) and the external environment is needed;
- as the solution is electrolyzed, concentration of solution varies; this problem can be more pronounced with little quantities of fluid;
- bubbles and solution have different densities, and bubbles tend to rise upwards because of their buoyancy;
- solution and electrodes can be contaminated by the products of electrolysis; a partial solution to this problem can be found in the right choice for the electrode material (stainless steel, platinum, graphite).

Experimental set-up

The experimental set-up shown in Figure 1 was used. A reservoir filled with an aqueous solution of sodium chloride was connected, through two pipes, to a peristaltic pump; the concentration of the solution was 9 g/L. The negative electrode (a platinum wire, diameter 0.001") was placed on the inlet section of a glass cylindrical duct, to allow the flow visualization; the positive electrode (an aluminum plate, approximately 4 square inches) was placed away from the direct flow incoming from the input pipe, thus avoiding chlorine bubbles interference.

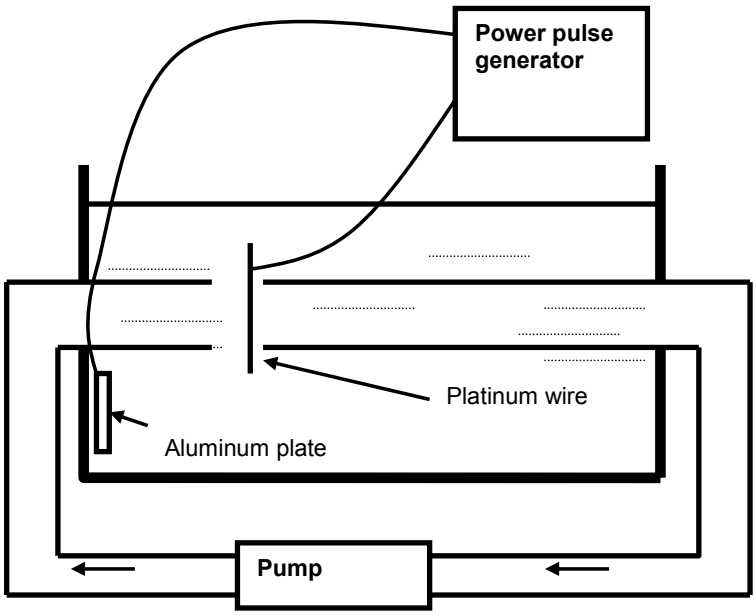

Figure1. Experimental set-up

The distance between the electrodes was maintained low in order to guarantee a low impedance in the electric circuit; consequently, the voltage of applied power pulses could be held to reasonably low levels.

Visualization and recording of fluid flow was performed with the aid of halogen lamps, laser beams and a digital camera connected to a computer. Electrodes were connected to a custom power pulse generator (block diagram in Figure 2). A stand-alone solution has been chosen, in order to minimize the connections between the apparatus and the surrounding environment; all that is needed is an external primary power source (a 12V 5Ah battery was successfully used during experiments).

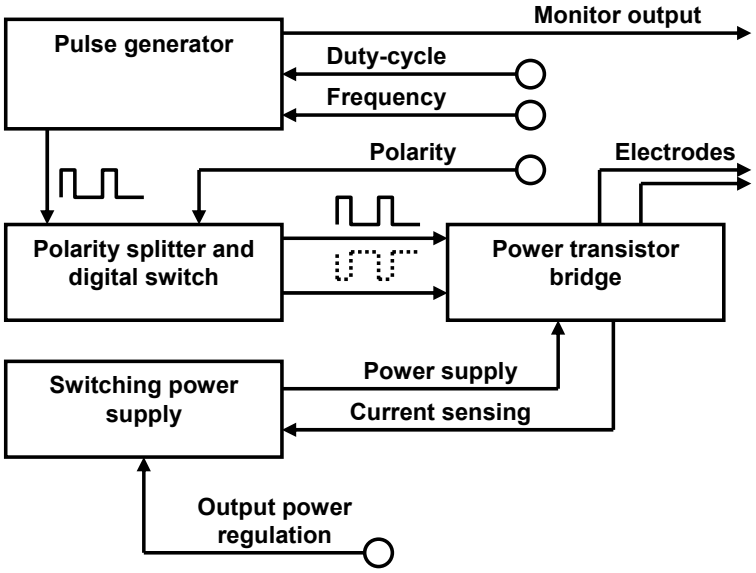

Figure 2. Block diagram of power pulse generator

Duty-cycle and frequency of electric pulses can be adjusted, depending upon experimental conditions. A monitor output signal is available; it can be connected to an oscilloscope, providing the necessary feedback to obtain the best visualization.

The polarity of output power pulses is controlled by the polarity command; in this way, the platinum electrode can receive positive or negative pulses. Electric pulses are amplified and translated to the requested levels by the power transistor bridge circuit; four high power Darlington transistors have been used, in order to obtain high power output pulses.

The output power regulation command is used to set the amplitude of the output power pulses; a current sensing signal is used to maintain the output current constant, in spite of variations of the conductivity of the aqueous solution.

Results

Figure 3 shows a picture taken during experiments. The platinum wire has been mounted on a Delrin insulating ring; small amounts of unwanted bubbles along the ring are caused by mechanical connection of the platinum wire to the power pulse generator. From this Figure it is possible to visualize the almost parabolic-shaped velocity profile: the skewness that can be highlight can be ascribed to the non axial arrangement of the platinum wire support with respect to the glass tube.

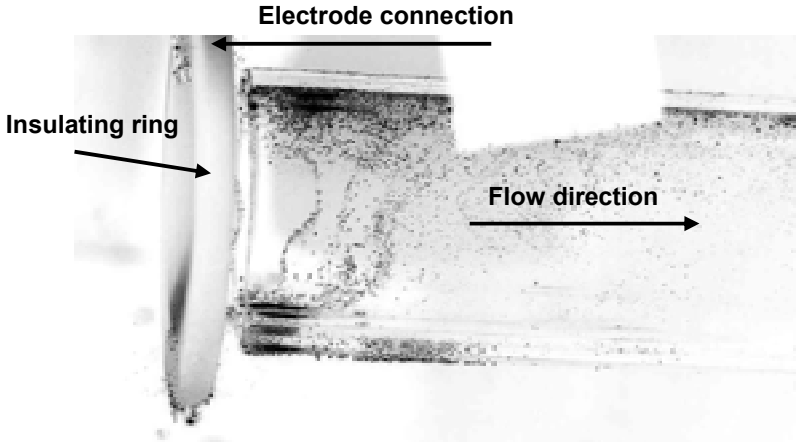

Figure 3. Example of flow visualization
(the platinum wire is in vertical position, inside the insulating ring)

Pulses width and pulse repetition rate have been set according to the flow regime imposed (0.8 L/min at 80 rpm) to obtain bubbles generation that allowed the best visualization; useful amounts of visible bubbles have been reached with voltage levels of about 30 V. Few bubbles accumulated on the inner top wall of the pipe, because of the buoyancy phenomenon.

Discussion

Flow visualization by bubbles generation is a basic method for highlighting *in vitro* fluid dynamic structures relative to, e.g., implantable medical devices such as prosthetic heart valves. This study presented a custom bubble generator for flow visualization, having the possibility to set several parameters in order to have the best set-up arrangement depending on the considered experiment. However some problems, intrinsic to the methodology herein discussed, such as possible perturbations introduced by the cathode may be decreased using small-diameter wires and, moreover, the buoyant velocity of bubbles may be only few percent of the flow velocity thus to not affect consistently the velocity field under investigation (5). Nevertheless, in some situations, the relative simplicity and the evident efficacy of the proposed set-up combined to the immediate presentation of the results, even if qualitatively, can be of primary importance.

References

1. Grigioni M, Daniele C, D'Avenio G, Barbaro V. Evaluation of the surface-averaged load exerted on a blood element by the Reynolds shear stress field provided by artificial cardiovascular devices. *J Biomech* 2002;35(12):1613-22.
2. Sprague EA, Luo J, Palmaz JC. Endothelial cell migration onto metal stent surfaces under static and flow conditions. *J Long Term Eff Med Implants* 2000;10(1-2):97-110.
3. Grigioni M, Daniele C, Del Gaudio C, Balducci A, Morbiducci U, D'Avenio G, Barbaro V: Critical aspects for a CFD simulation compared with PIV analysis of the flow field downstream a prosthetic

heart valve. In: Brebbia CA, Arnez ZM, Solina F, Stankovski V (Ed.). *Simulations in Biomedicine V. Advances in Computational Bioengineering*. Southampton, Boston: Wit Press; 2003. p. 271-80.

4. Saxena R, Lemmon J, Ellis J, Yoganathan A. An *in vitro* assessment by means of laser Doppler velocimetry of the Medtronic advantage bileaflet mechanical heart valve hinge flow. J *Thorac Cardiovasc Surg* 2003;126(1):90-8.
5. Lichtenstein O, Martinez-Val R, Mendez J, Castillo-Olivares JL. Hydrogen bubble visualization of the flow past aortic prosthetic valves. *Life Support Syst* 1986;4(2):141-9.
6. Merzkirch W. *Flow visualization*. New York: Academic Press, Inc.; 1974.

ULTRASOUND AND VENTRICULAR FLUID DYNAMICS

Federico Domenichini (a), Gianni Pedrizzetti (b)
(a) Dipartimento di Ingegneria Civile, Università di Firenze, Florence, Italy
(b) Dipartimento di Ingegneria Civile, Università di Trieste, Trieste, Italy

Introduction

Comprehensive understanding of the blood dynamics through cardiac cavities has potential clinical relevance where diseases, interventions, or presence of devices alter the physiological relations between morphology, motion and timing of the heart. Maintenance or restore of physiological flow patterns through the heart might affect ventricular remodelling or incidence of intracavitary thrombosis after cardiac surgery. In addition, mathematical models able to reproduce some physiological flows under realistic conditions can help in understanding the interaction between contractility, elasticity and change in momentum at atrial, ventricular and great vessel levels. It allows the design of new, more physiologically sound, diagnostics and interventional devices. Finally, mathematical models of intracardiac flow might improve the interpretation of quantitative parameters obtained from currently used imaging techniques able to interrogate intracardiac flow.

Blood flow in the human left ventricle has been investigated by several physical and computational modelling either under the axisymmetric assumption and with three-dimensional models that suffer of some limitation in the accuracy especially near the boundaries (1), and references therein). Current imaging techniques, like echocardiography and magnetic resonance, allow a direct visualization of intraventricular flow (2,3). Nevertheless, flow patterns within the normofunctioning human left ventricle, as well as their modification in presence of a specific cardiac disease, remain to be clarified.

The increasing capabilities of numerical computation allow scientists to reproduce some physiological flows under realistic conditions and to visualize the mechanical phenomena involved. Accordingly, we developed a mathematical model describing the normal flow pattern in the left ventricle and numerically solved the three-dimensional Navier-Stokes equations in a Left Ventricular (LV) half prolate spheroid geometry with moving walls. The simulations, performed with a highly accurate simulation method (4), were designed on the basis of data extracted semi-automatically from echocardiographic data. The computed results were compared with actual data obtained from pulsed wave and two-dimensional flow velocity mapping from Doppler echocardiography performed on healthy human subjects.

Methods

Extraction of quantitative echocardiographic data

The geometric and dynamics data required as input to the mathematical model were extracted with semi-automatic procedures from echocardiographic imaging. Data used to develop the mathematical model were obtained from a healthy prematurely born children, weighing 0.8 kg, that had not known cardiac or systemic diseases. The computational model was also tested on data obtained from a normal child (not reported for brevity).

Echocardiographic studies were performed with standard techniques. From the apical 4-chamber view, pulsed Doppler recordings of the LV inflow were acquired at a horizontal sweep speed of 1000 mm/s. From the same echocardiographic window 3 R-R loops of two-dimensional and color Doppler velocity map of LV flow was obtained together with a single ECG lead. The LV endocardial border was manually drawn on one frame and then automatically tracked and identified on all frames of the sequence using a dedicated software package (Diogenes software prototype; Siemens Medical Systems Mountain View CA, and Advanced Medical Imaging Development, Roma, Italy). Once the endocardial border motion has been identified, the LV volume V(t) was computed, for each frame, using the Simpson's rule (64 disks).

The geometry of the left ventricle was approximated as that of half prolate spheroid, defined by the instantaneous values of the equatorial plane (next to the mitral plane) diameter D(t), and of the major semiaxis H(t). Such a geometry was adjusted on the computed border by selecting the time-profiles of D(t) and H(t) that best approximate the actual cavity shape with the constraint that the prolate spheroid should have the same LV volume. The mitral eccentricity ε was evaluated directly from the Doppler images by measuring the position of the jet-axis between the annuli. The mitral velocity U(t) during LV diastole was measured with the pulsed-wave Doppler interrogation. The first noisy estimate of the mitral jet size σ(t) was computed from continuity $U\pi\sigma^2/4=dV/dt$ and then modelled as piecewise constant (during E- and A-waves) linearly connected during the diastasis. The steps of this processes are shown in Figure 1.

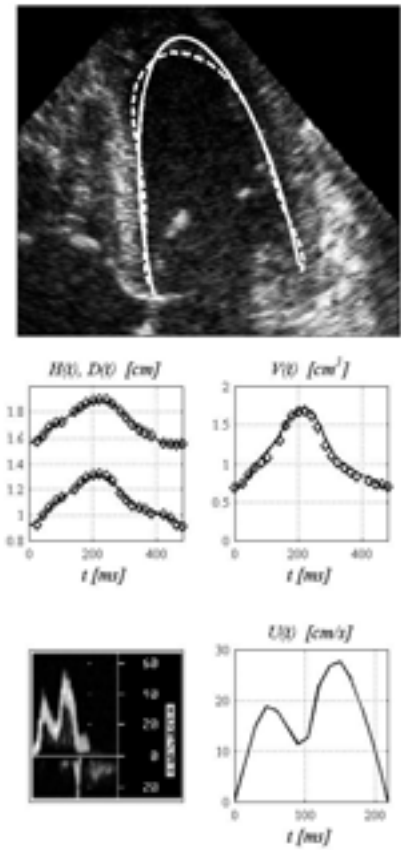

Figure 1. Extraction of echocardiographic data. Top: endocardial border at one time point: tracked (dashed line) and model fitting (continuous line). Middle left: H(t) and D(t), tracked (squares) and model fitting (continuous line). Middle right: V(t), tracked (squares) and model fitting (continuous line). Bottom: transmitral velocity, clinical data (left) and model fitting (right)

Development of the mathematical and numerical model

The description of the mathematical system, details and tests of the numerical method can be found in (5). Briefly, the numerical method is based on centred finite differences, in the prolate spheroid system of coordinates, with a spectral expansion along the circumferential coordinate. The equations are solved on a half prolate spheroid domain defined by D(t) and H(t) (see Figure 1).

The time-law of the ventricular volume V(t), and of the entering/exiting flow Q(t)=dV/dt are reconstructed from them. The three-dimensional Navier-Stokes equations are written in the prolate spheroid body-fitted system of coordinates (5). The fluid problem has two dimensionless parameters, the Stokes number $\beta=D_0^2/\nu T$, and the Strouhal number $St= D_0/U_0T$; ν is the kinematic viscosity of the fluid, assumed to be Newtonian, typically equal to $3.3x10^{-6}m^2/s$, T is the heartbeat duration, D_0 is the value of D(t) at the end of diastole, U_0 is the transmitral flow peak velocity. The LV flow was enforced assigning inlet/outlet velocity profiles at the mitral plane, simulating the mitral inflow and the aortic outflow, respectively, characterised by the mitral eccentricity ε, and by mitral/aortic jet size $\sigma(t)$ (Figure 2).

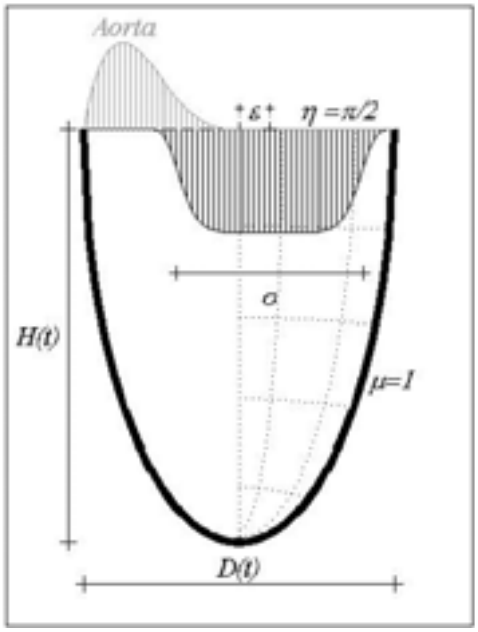

Figure 2. Sketch of the mathematical model

In summary, the model is completely specified once the time variation D(t) and H(t), the value of β are given in addition to the flow parameters ε and σ. The time laws D(t) and H(t) could in principle be obtained assuming an elastic model for the compliant ventricle walls subjected to the computed fluid pressure.

Such an approach would have required the knowledge of the LV thick walls viscoelastic behaviour and its time varying properties; in addition the pressure time-law at the inlet, or the parameters of a global circulatory model, must also be given. These data are not measured in routine clinical observations, and reliable data are not easily available or accessible. Therefore this is a model for the intraventricular blood mechanics only, as a consequence of the D(t) and H(t) measurements, that is not affected whether the same geometry is given or it is computed.

Results

The method described above was applied to simulate the LV flow of a prematurely born baby, weighing approximately 0.8 kg. Being T=480 ms and D_0=13.1 mm, we have β=109. The mitral jet has a diameter σD varying in the range (0.45 – 0.65)D(t), s is initially taken equal to 0.65 (E-wave) then linearly decreased, during the interval 0.2T<t<0.25T, to the value σ =0.45 (A-wave). The eccentricity was found to be ε=0.125D. The resulting value of the Strouhal number is St=0.099.

Comparison between Color-Doppler images and the corresponding maps derived from the computed results, not reported here, shows a qualitative good agreement. Data from the numerical simulation allow us to get some deeper insights into the actual flow dynamics. In the upper row of Figure 3 the flow on the scanplane is shown in terms of vorticity distribution (grayscale background) and velocity (arrow vectors) at three time points (t=162, 217, and 278 ms), corresponding to the peak of the A-wave, the end-diastole, and the peak velocity of systole, respectively. During the early filling (E-wave), not shown in Figure 3, the mitral flow forms a weak vortex wake close to the mitral plane. In our case of a prematurely born baby whose transmitral flow has E/A= 0.68, a faster jet is produced by the acceleration during atrial contraction. The vortex structure produced during the A-wave dominates the wake flow field (Figure 3a). It must also be noticed that the inflow is not axial but naturally redirected toward the LV lateral wall (to the right in Figure). At end-diastole, the vortex structure nearly fills the cavity and gives rise to a large recirculating flow mainly beneath the anterior mitral leaflet. The flow is directed toward the apex on the side next to the lateral wall and it is reversed behind the anterior leaflet (Figure 3b). During the ejection, viscous dissipation reduces the intensity of the vortex that was almost disappeared (Figure 3c).

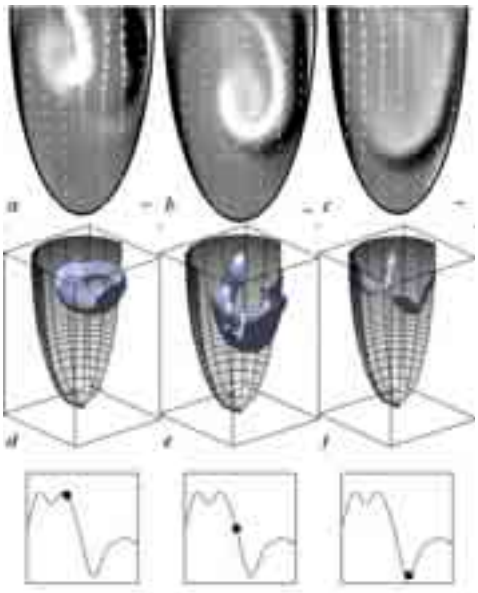

Figure 3. Numerical results. Upper row: flow on the scanplane, vorticity distribution (grayscale) and velocity (arrow vectors); the black arrows correspond to a velocity of 10 cm/s. Lower row: isosurfaces of the scalar indicator of vortex structures λ_2. Times: t = (162, 217, 278) ms from a to c and from d to f (peak of the A-wave, end of diastole, peak of the systole, respectively)

The description of the LV flow pattern outlined in Figure 3 (a to c), is based on a two-dimensional slice of the three-dimensional flow. A more complete picture of the intraventricular flow dynamics is shown in terms of vorticity in Figure 3 (d to f), where the isosurfaces of a scalar indicator of vortex structures are shown using the so-called λ_2-method (4). The diastolic wake vortex is initially a vortex ring with nearly circular geometry placed behind the mitral valve (Figure 3d). This ring corresponds to the head of the mitral jet. Afterward, when the mitral inflow is almost completed, the vortex propagates downstream and it is subjected to a self-induced deformation, leading to a convergence of the vorticity below the anterior leaflet of the mitral valve, while the vortex portion behind the posterior leaflet is destroyed by the interaction with the LV wall. At end-diastole the structure resembles a horizontal vortex, corresponding to the circulation cell on the scanplane, with two vertical legs (Figure 3e). These mean the presence of secondary swirling flow. At the very end-diastole the vortex begins to dissipate by the viscosity and is almost disappeared during systole (Figure 3f).

Discussion

The three-dimensional intraventricular flow field have been reproduced by a complete numerical solution of the mechanical equations, forced by echographic data.

Previous studies about the left ventricular fluid dynamics have been mainly limited to the axisymmetric assumption (1), while three-dimensional simulations based on the immersed element technique suffer of some limitation in the accuracy especially near the boundaries. Indeed, fully resolved three-dimensional simulations are at the limit of normally available computational resources and this study, too, had included some limitations.

The three-dimensional flow pattern here described is profoundly different to what could be found within axially symmetric models (1). The three-dimensional evolution of the flow field has shown the development of a main circulation region, as commonly supposed from Doppler imaging and MRI (3), corresponding to a slice of a three-dimensional vortex structure that is formed at the mitral valve leaflets edge. This vortex forms essentially as a jet whose leading head takes the shape of a deformed vortex ring. The jet deviates towards the LV lateral wall that is therefore subjected to a higher pressure, with a reversed flow next to the interventricular septum. The internal vortex structure eventually develops into a horizontal tube terminating with vertical legs that account for the swirling nature of the flow. The vorticity rapidly dissipates at the end of diastole and eventually disappears during systole. The dissipation is enhanced by three-dimensional instability; this, found here in a paediatric heart, suggests that a larger LV cavity will develop some weak turbulence during diastolic deceleration.

These results, although preliminary, contribute to build interpretative schemes for clinical observations, remodelling and therapeutic options. They could improve the physical understanding of the diagnostic imaging based on flow visualisation to eventually give a mechanical interpretation of the diagnostic parameters in terms of the corresponding flow phenomena. These results must be considered as preliminary because of several modelling limitations. The ventricular geometry has been taken as that of a prolate spheroid with smooth walls, therefore the results can not be generalised to irregularly shaped ventricles and do not account for the papillary muscles or chordae tendinae. The main limitation is the absence of a valvular modelling. The work is in progress on this topic, the valvular leaflets are expected to influence the jet development.

References

1. Baccani B, *et al*. Model and influence of mitral valve opening during the left ventricular filling. *J Biomech* 2003;36(3):355-61.
2. Kim WY, *et al.* Left ventricular blood flow patterns in normal subjects: a quantitative analysis by three-dimensional magnetic resonance velocity mapping. *J Am Coll Cardiol* 1995;26:224-38.
3. Kilner PJ, *et al*. Asymmetric redirection of flow through the heart. *Nature* 2000; 404:759-61.
4. Jeong J, Hussain F. On the identification of a vortex. *J Fluid Mech* 1995;285:69-94.

PHASE-DOMAIN METHODS IN DOPPLER ULTRASOUND

Giuseppe D'Avenio, Cecilia Poli, Gad Piperno, Carla Daniele, Vincenzo Barbaro, Mauro Grigioni
Dipartimento di Tecnologie e Salute, Istituto Superiore di Sanità, Rome, Italy

Introduction

Since almost 20 years, echographic equipments are available that can provide velocity measurements of circulatory flows in real time (1). This information is presented usually as a color-coded image, superimposed on a echographic image of the corresponding local anatomy. Thus, the method is generally known as color Doppler. Anyway, the same information can be presented also in other forms, such as, e.g., instantaneous velocity profiles (2).

In pulsed Doppler systems, such as those here considered, a short pulse of ultrasound is delivered to the zone of interest, and the backscattered signal is processed to yield hemodynamical data. The information on the local velocity is contained in the signal reflected by the erythrocytes carried by the blood stream. Their velocity affects the characteristics of the Doppler signal, in that a gradual translation occurs, both as a phase- and a time-shift, between successive pulse returns. Then, the methods of velocity measurements can be divided in two main categories: time-domain and phase domain methods. In this paper, we consider two algorithms belonging to the class of phase domain methods; the comparison will be carried out on the basis of numerical simulation and experimental measurements.

Materials and methods

Velocity estimation from ultrasound data

The most successful method pertaining to the class of time-domain method is represented by the cross-correlator. By means of the cross-correlation between successive pulse return, it is able to reconstruct the mean displacement of the scatterers and, hence, their velocity (3). A disadvantage of this method, which has hindered its diffusion, is given by the necessity of processing the complete received signal, sampled at high frequency (owing to the Nyquist theorem, the sampling frequency must be such that $f_s > 2f_{max}$, where f_{max} is the maximum received frequency). This baseband processing is computationally demanding, since the necessity of performing a large number of operations per second.

With phase-domain methods, the received signal is processed in order to extract the mean phase shift between successive returns. Thus, the local velocity is calculated from the phase shift, The traditional (1D) autocorrelator measures the average phase shift, with respect to the central frequency of the transmitted pulse, induced by the average motion of the scatterers present in the flow. In this approach, the demodulated signal is used, instead of the received signal, with the advantage of baseband processing and the consequent reduced sampling rate requirements with respect to time-domain methods. For this reason, the autocorrelation method proposed by Kasai *et al.* (1) is still the most used in commercial scanners. It relies on the in-phase and quadrature components (I and Q, respectively) of the signal, whose extraction is depicted schematically in Figure 1. The received signal s(t) is multiplied by the appropriate

harmonic signal at the transmitted frequency, and the high-frequency modulation products are rejected by the Low Pass Filters (LPF).

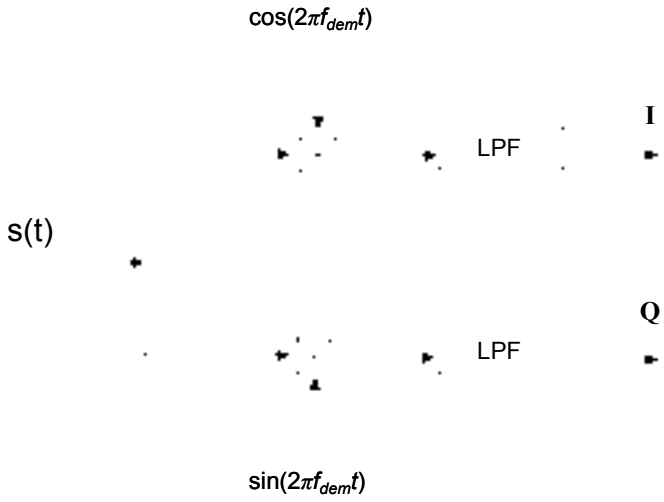

Figure 1. Extraction of the in-phase and quadrature signals (I and Q, respectively) from the received signal

Due to the structure of the data set on which it operates, the autocorrelation method is hereby denoted as "1D autocorrelator". In fact, the ensemble average of the velocity is performed on a number of estimations equal to the number of transmitted pulses (*N*), after the estimation of the mean phase of the signal received after each pulse and subsequent demodulation of the latter. This approach can be improved by means of a more complete analysis of the available signal, in order to evaluate more accurately the Doppler equation. As shown by Loupas et al. (4), the return signal can be subjected to a 2D Fourier transformation, so that the resulting spectrum can be plotted as a function of two quantities, the high frequency and the Doppler frequency. In Figure 2 an example is shown (from simulated data) of the spectrum relative to a uniformly moving target: it can be seen that a definite peak occurs in the quadrant of the positive frequencies (as well as in the opposing quadrant). The two frequencies corresponding to this peak, $\langle RF \rangle, \langle f_{Dopp} \rangle$ (the brackets denote the average value), are related to the velocity by means of the Doppler equation,

$$\langle v \rangle = \frac{c}{2} \frac{\langle f_{Dopp} \rangle}{\langle RF \rangle} \qquad [1].$$

The peak of the spectrum tends to get broader as the noise level is increased, indicating the necessity of a careful analysis of the signal itself, in such cases.

The calculation of the average frequencies is carried out by means of 2D integrals that yield the center of mass of the quantity of interest. Adopting the notation of Loupas *et al*. (4), as a unifying framework, these averages can be expressed explicitly as follows:

$$\langle RF \rangle = \frac{\int_{-0.5}^{0.5}\int_{-0.5}^{0.5} RF\,\hat{\Gamma}(f_{Dopp}, RF)\,df_{Dopp}\,dRF}{\int_{-0.5}^{0.5}\int_{-0.5}^{0.5} \hat{\Gamma}(f_{Dopp}, RF)\,df_{Dopp}\,dRF} \quad [2];$$

$$\langle f_{Dopp} \rangle = \frac{\int_{-0.5}^{0.5}\int_{-0.5}^{0.5} f_{Dopp}\,\hat{\Gamma}(f_{Dopp}, RF)\,df_{Dopp}\,dRF}{\int_{-0.5}^{0.5}\int_{-0.5}^{0.5} \hat{\Gamma}(f_{Dopp}, RF)\,df_{Dopp}\,dRF} \quad [3].$$

Here $\hat{\Gamma}(f_{Dopp}, RF)$ denotes the spectrum of the analytical signal associated to the return signal s(t); the use of $\hat{\Gamma}(f_{Dopp}, RF)$ is suggested by its property of having a null content for negative frequencies.

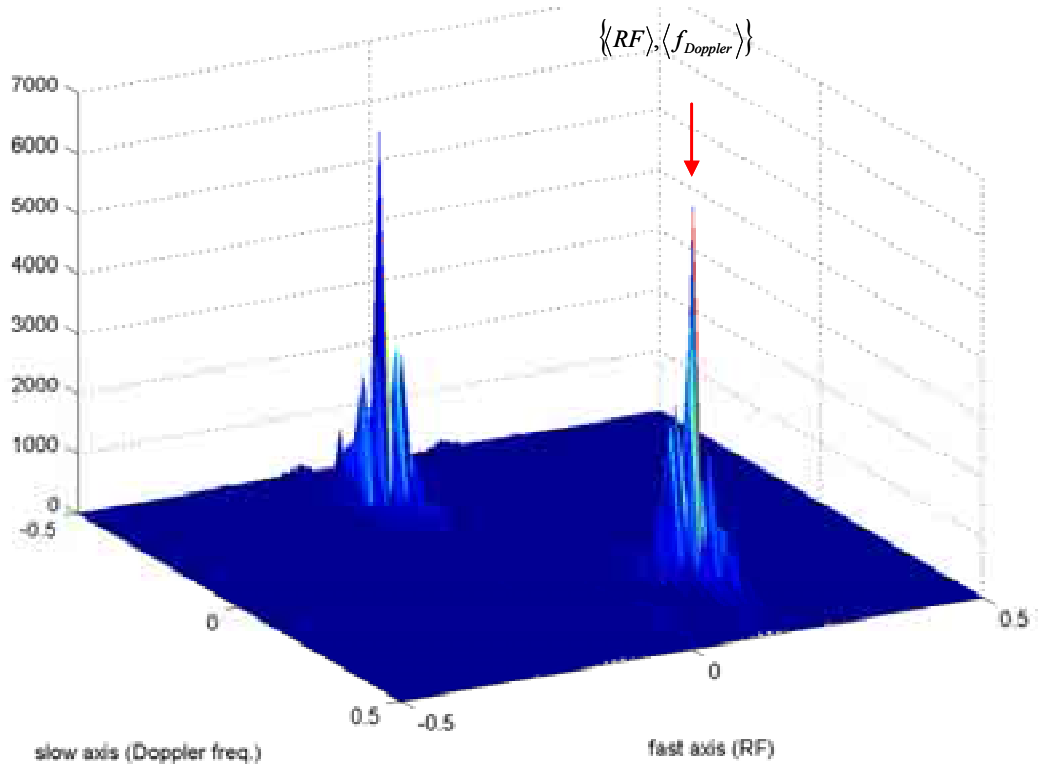

Figure 2. Bidimensional spectrum of the received signal

In practice, it is not convenient to carry out explicitly the indicated operations; instead, it is preferable to use the autocorrelation function of the return signal (whence the denomination "2D autocorrelator" proposed by Loupas *et al.* (4)). Both algorithms, for $\langle v_{1D} \rangle$ and $\langle v_{2D} \rangle$, make use of the in-phase and quadrature signals, the latter being arranged in two-dimensional arrays,

$I(m,n), Q(m,n)$, m=0,.. M-1, n=0,.. N-1, where M is the number of depth samples (along the axis of the transducer) used for a single velocity estimation and N is the number of pulse returns. There are two important differences between the two methods:

1) the Doppler frequency is estimated in a different way, for $\langle v_{1D} \rangle$ there is an average first along the depth direction (i.e., quantities are summed over m) and then along the pulse direction (n), whereas for the 2D approach all the relevant samples are considered at the same time;
2) the estimation of the average of the received high frequency is very different, in that in the 1D traditional approach it is assumed equal to the transmitted frequency, whereas in the 2D autocorrelator it is explicitly calculated, in the same way as the Doppler frequency. This allows to take into account the fluctuations of the received signal, which are very well correlated with the fluctuations of the Doppler frequency. Thus, from the Doppler equation an improvement in the accuracy of velocity estimation can be expected.

An extensive numerical simulation (1000 repetitions for each set of parameters) has been carried out, with different SNR conditions. A constant velocity was imposed in the numerical model, so that the standard deviation of the result can be chosen as a figure of merit for the particular algorithm considered: ideally, the observed standard deviation should be zero, in such conditions, but the random nature of the scatterers' distribution in the flow prevents the velocity estimators' accuracy to attain such level. Nevertheless, the efficiency of each algorithm results in significant difference in the standard deviation of the velocity estimation.

Experimental measurements have also been carried out, using the *I* and *Q* signals provided by a commercial US profilometer (DOP1000, Signal Processing, AG, Switzerland). The carrier frequency was set at 8 MHz, the Pulse repetition frequency (PRF) was given by 1/PRF=Ts=64 ms. The I & Q signals were acquired at 5 MHz. A steady-flow hydraulic loop provided the test bench for comparative measurements with both autocorrelation approaches. The mean Reynolds number was around 1250, which guarantees laminar flow conditions.

Results

The results of the simulations at SNR=10 dB (Figure 3) show that the 2D approach outperforms the traditional 1D autocorrelator, at each value of the couple of parameters M and N, because the standard deviation of the velocity estimation is always lower for the 2D autocorrelator. The increased computational burden required by the 2D autocorrelator is, then, well justified by its performance, in realistic SNR conditions. Also at higher SNR (20 dB; data not reported) a higher precision of the 2D approach was observed.

The experimental comparison dealt with the calculation of the flow profile in a steady-flow loop. The transducer was positioned at 45 degrees, towards a slightly curved tube, at the same side of the center of curvature; then, a slightly skewed flow profile is to be expected, with higher velocities at the proximal half of the profile.

Due to the available space of the buffer for data acquisition, the calculation of the flow profile could be carried out for M=32 and N=45, at most. In such conditions (Figure 4), the 2D profile is certainly more accurate, since the skewness of the profile is qualitatively the same as expected by the slight curvature of the tube, and the 1D profile presents a velocity minimum in the center of the profile, whereas in steady-flow conditions this effect can be excluded, and is therefore an artifact provided by the poorer performance of the 1D approach. Even worse results have been found for smaller data sizes: for instance, with M=24 and N=6, a zone of flow reversal appears at the edge of the 1D profile, whereas the 2D autocorrelator still presents a result similar to that shown in Figure 4.

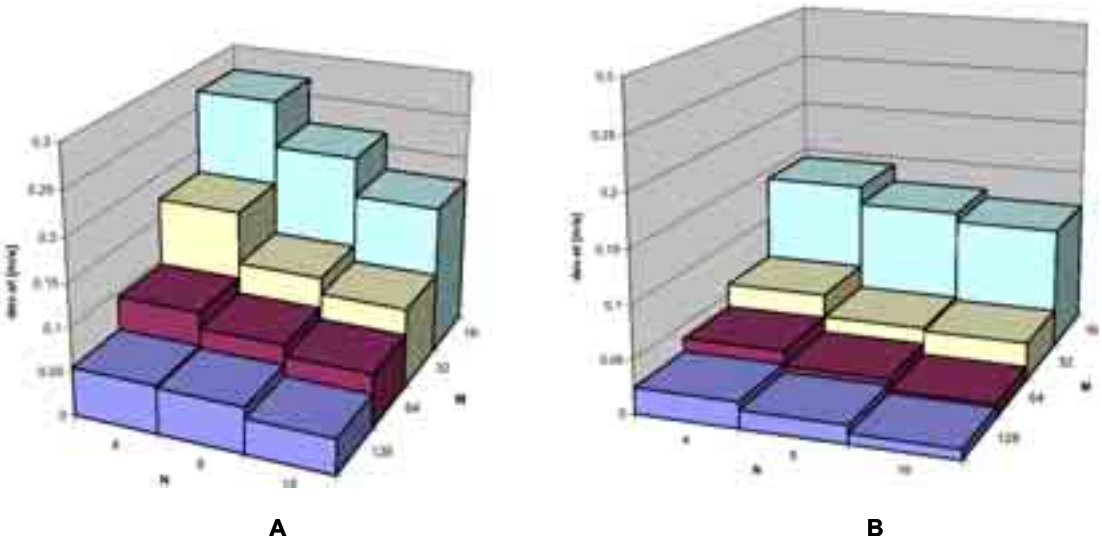

A B

Figure 3. Standard deviation of the velocity determination, as a function of the number of depth samples (M) and pulse returns (N). The values relative to the 1D approach (A) are always higher than those of the 2D autocorrelator (B)

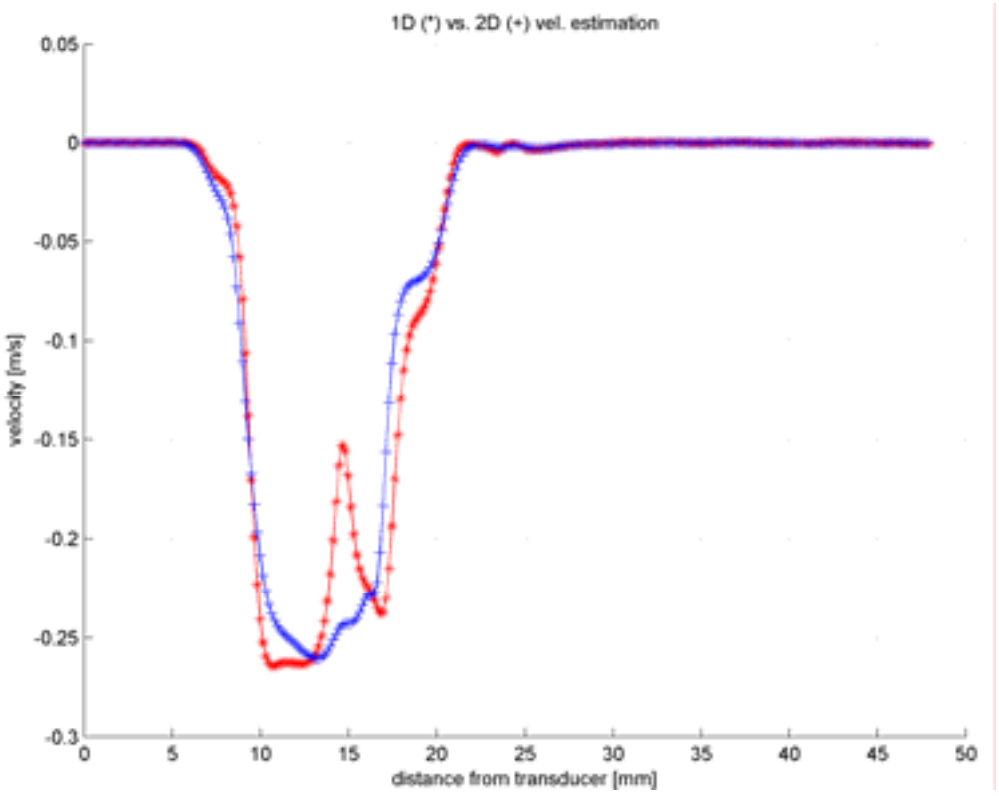

Figure 4. Flow profile, according to the 1D (asterisks) and the 2D (crosses) autocorrelation

Conclusion

Numerical and experimental studies have been carried out on two methods for velocity estimation by means of Doppler ultrasound. It was found that the traditional 1D autocorrelator, still widely used in real-time US scanners, has a poorer performance than a more recent 2D approach, in terms of accuracy and robustness to noise.

References

1. Kasai C, Namekawa K, Koyano A, Omoto R. Real-time two-dimensional blood flow imaging using an autocorrelation technique. *IEEE Trans Sonics Ultrason* 1985;32:458-63.
2. Grigioni M, Daniele C, D'Avenio G, Formigari R, Bernucci P, Ballerini L, Barbaro V. Pulsatile flow and atherogenesis: results from *in vivo* studies. *Int J Artif Organs* 2001;24(11):784-92.
3. Hein IA, Chen JT, Jenkins WK, O'Brien WD. A real time ultrasound time-domain correlation blood flowmeter: Part 1 theory and design. *IEEE Trans Ultrason Ferroelect Freq Cont* 1993;40:768-75.
4. Loupas T, Powers JT. An axial velocity estimator for ultrasound blood flow imaging, based on a full evaluation of the Doppler equation by means of a two-dimensional autocorrelation approach. *IEEE Trans Ultrason Ferroelect Freq Cont* 1995;42:672-88.

NUMERICAL APPROACH FOR THE ANALYSIS OF THE BEHAVIOUR OF PROSTHETIC MECHANICAL HEART VALVES

Monica Soncini (a), Alberto Redaelli (a), Matteo Nobili (a), Emiliano Votta (a), Umberto Morbiducci (b), Costantino Del Gaudio (b), Antonio Balducci (b), Mauro Grigioni (b)
(a) Dipartimento di Bioingegneria, Politecnico di Milano, Milan, Italy
(b) Dipartimento di Tecnologie e Salute, Istituto Superiore di Sanità, Rome, Italy

Introduction

The use of Computational Fluid Dynamics (CFD) to investigate heart valve mechanics presents a considerable challenge because of the large rotations that leaflets encompass and the fully coupled fluid-structure interaction features of the phenomenon. Two approaches are currently possible, whether the fluid-structure boundary movement is loosely calculated through interpolation techniques without deforming the mesh of the fluid domain (1) or the fluid mesh deformation is actually accounted for (2, 3). Methods adopted in the first case have the advantage to avoid mesh movement treatment and are versatile, but suffer from inaccuracy at the interface between the fluid and the leaflets. In the second case, the fluid-structure interaction at the boundary is more consistent; the computational grid moves accordingly to the fluid-structure boundary. This approach is usually based on the Arbitrary Lagrangian Eulerian (ALE) approximation, which allows to incorporate grid velocities in the momentum and continuity equations of the fluid domain. However, this approach is problematic for valve simulations, since the large mesh deformations due to the leaflet's rotations are critical for mesh adaptation. Moreover they are more demanding in terms of computational costs. To the author's knowledge, ALE based model available in literature on mechanical valves are limited to the two dimensional case (2, 4). Most of the works focus on the feasibility of simulating the opening or closure process of a heart valve. Experimental validation is not taken into account, with the exception of the works on bioprosthetic valves (4) and on 2-D mechanical valves (5).

The present study reports the 3D numerical and experimental simulation of the opening process of a bileaflet mechanical heart valve. The study is based on a moving deforming mesh method in conjunction with a remeshing algorithm as implemented in the CFD commercial software. Simulations were performed at the Laboratory of Computational Biomechanics of the Polytechnic University of Milan. The 27 mm size St. Jude HP was investigated, whose technical drawings were provided by St. Jude Medical. The Laboratory of Biomedical Engineering of the Italian National Health Institute carried out *in vitro* experimental simulations of the study.

Materials and methods

Experimental simulation

The experimental session was performed with a pulsatile, open loop, Mock Circulatory System (MCS) - the VSI (Vivitro Systems Inc.) mock loop properly modified (Figure 1) (6). The mechanical bileaflet prosthetic valve was located in the aortic valve site, while a

mechanical reference valve was inserted in the mitral site. Ventricular, atrial and aortic pressure measurements were performed through wall pressure ports. Aortic and mitral flow measurements were performed with two electromagnetic flow meters located in the aortic and mitral valve position, respectively (Figure 1).

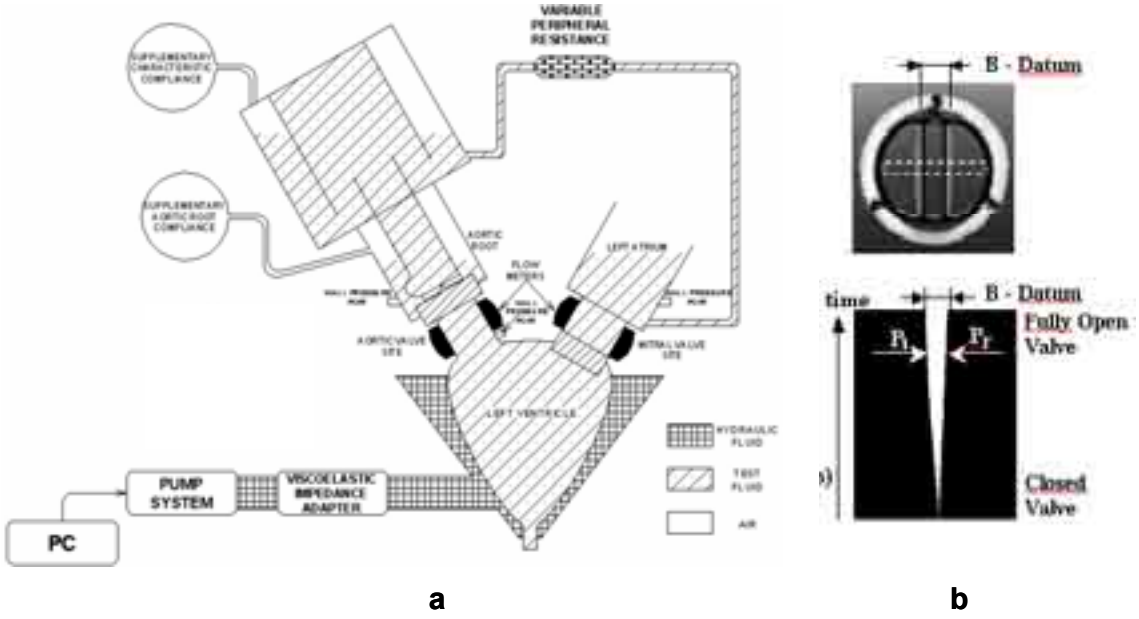

Figure 1. Sketch of the MCS (a); temporal evolution of the gap between the leaflets (B-Datum) during the beat, from the completely closed valve configuration to the fully open one (b)

The hydrodynamic behaviour of the prosthetic valve was investigated with a solution of water and 35% glycerol; the viscosity of the solution was approximately 3.7 10^{-3} Pa s. A cardiac output of 2 L/min, with a mean arterial pressure of 100 mmHg and a heart beat of 72 beats per minute were the investigated working conditions for the prosthetic valve, in order to attain laminar flow throughout the cardiac cycle. The study of the kinematics of the prosthetic valve was performed using ultrafast cinematographic technique (6). The MCS allows to approach the vision of the valvular function through which a high speed videocamera (Kodak Ektapro; 239 x 192 pixels, fc=1000 frames per second). The splitting of the Ektapro screen into 12 parallel slices allowed us to grab the image of the central piece of the prosthetic valve (Figure 1b) with a 12000 frames/s rate. The position of the innermost points at the internal left and right leaflet edge (Pl and Pr, respectively), was recorded, thus allowing to measure the width of the gap between the leaflets (B Datum, Figure 1b).

Numerical model

The numerical simulation was performed with the finite volume commercial software Fluent 6.1; Fluent software is not designed for fully coupled fluid-structure interaction problems, but provides well suited features for the handling of the specific problem of rotating boundaries. Fluent provides a robust mesh deformation handling method, which can be used in conjunction with a remeshing algorithm for the treatment of degenerated cells. Moreover, Fluent accounts for the ALE formulation, thus providing an accurate solution for the Navier Stokes equations in

deforming meshes. Valve seat, leaflet geometries, aortic and ventricular conduits were modelled from St. Jude Medical and MCS technical drawings, respectively; only the ducts located between the MCS pressure sensors were modelled (see Figure 1).

The valve seat and the leaflet geometries were slightly modified in order to attain a high-quality mesh throughout the valve opening phase; a 0.07 mm gap was created between the leaflets in the closed position so as to put two rows of cells in between. The role of the butterfly hinges was simulated by limiting the leaflet rotation between 24 (fully closed position) and 84 degrees (fully opened configuration), with respect to the valve orifice plane. Concerning the MCS model, the Valsalva sinuses were approximated with a surface of revolution (Figure 2).

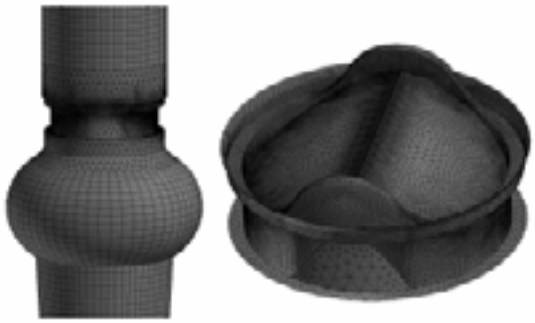

Figure 2. Discretised model of both the overall fluid domain and the valve surface

The valve region was discretised with tetrahedral elements according to the MDM (Moving Deforming Mesh module) requirements. In the aortic and ventricular ducts, an hexahedral mesh was used in order to limit the numerical diffusion (total number of cells is 340,000). Fluid properties were set according with the fluid used in the experimental simulations. The density of the leaflet was set to 2000 kg m^{-3} (data provided by St. Jude Medical) and leaflet moment of inertia equal to 9.51 10-9 kg m^2 was calculated by means of a structural code. A no-slip condition was set on the walls. The experimental pressure drop between the inlet and outlet was applied as boundary condition for the simulation. The time step was equal to 0.02 ms. The complete opening of the valve was obtained in 154 h.

In order to simulate a bidirectional fluid-structure relationship, the MDM was used in conjunction with two user-defined subroutines, working together iteratively through consecutive steps; at the beginning of each step the first one calculates and updates the kinematics of the leaflets on the basis of the moment applied to the leaflet, which is calculated by the second subroutine at the end of the previous step, once the time step convergence has been achieved. Two simplifying assumptions are inherent to the described procedure: a delay of one time step occurs in the communication between the fluid and the leaflet solvers, since the mesh is updated at the beginning of the time step and the updated flow patterns are available at the end of the time step; moreover an under-relaxation parameter was implemented in order to smooth the moment between steps, which introduces a further delay in the information exchange.

Results

Figure 3 shows the streamlines coloured by velocity magnitude. No vortices were observed during the opening process of the valve. This is justified by the relatively low Reynolds number of 2430 in the highest velocity region, that is located at the leading edge of the leaflet, at the symmetry plane.

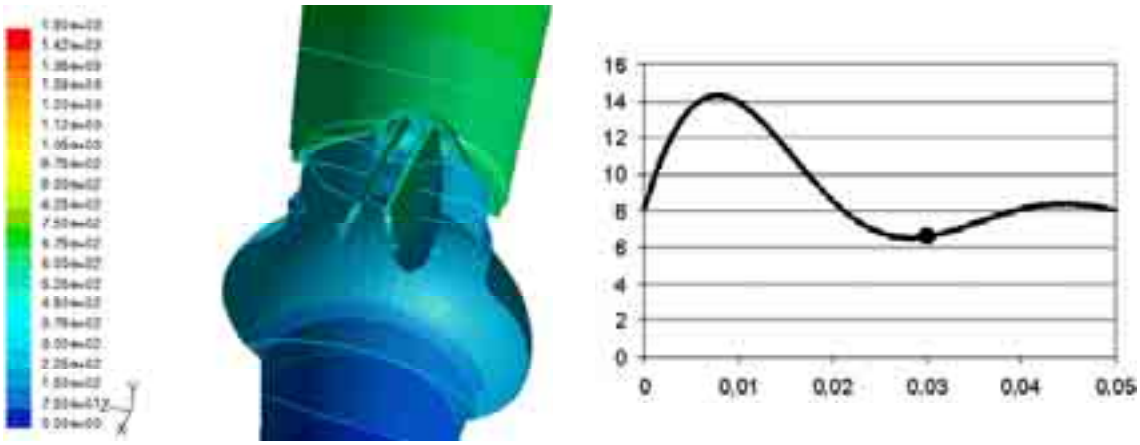

Figure 3. Pressure magnitude calculated in an intermediate opening phase (opening angle of 64°)

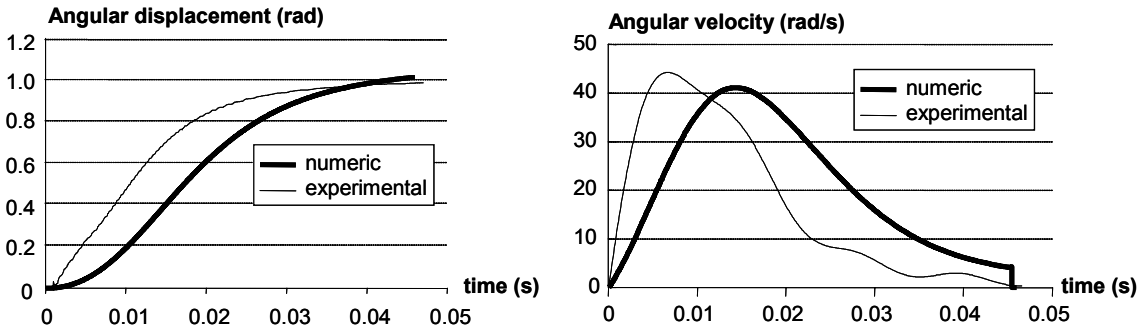

Figure 4. Comparison between experimental data and numerical simulation

Figure 4 reports the comparison between numerical and experimental results in terms of valve kinematics. Numerical results about valve angular displacement and velocity show a good, although approximated, agreement with experimental measurements. The opening angle process is delayed by about 7 ms considered acceptable with respect to the opening phase time lapse of 46 ms. Angular velocity is slightly underestimated (7%).

Discussion

The present work focused on the simulation feasibility of a realistic 3D model of a mechanical valve: the natural counter-part was the set-up of a rigorous experimental protocol for the assessment of the boundary conditions and for comparison. The most critical feature of the simulation performed is the delay observed between the experimentally observed and calculated angular displacement. It should be noted that this behaviour was observed also by other authors, who observed a 18 ms delay of the valve motion with respect to the fluid velocity onset during the opening process (1), and a delay of 7-10 ms with respect to the pressure onset (5). Thus, the occurrence of the observed delay in the leaflet response with respect to the fluid forces is not likely due to the weakly coupled fluid structure scheme. More probably, it may be due to the overestimation of the fluid inertia, the fluid being assumed quiescent at the beginning of the systolic phase: this implies a larger inertial load contrasting the onset of the opening process.

In the present study, some simplifying assumptions have been adopted and further investigations are mandatory. The Reynolds number has been limited to about 2400. Also the experimental set-up may be improved with respect to the triggering of the actual opening process onset and to a more detailed evaluation of the flow patterns at the opening process onset. The fluid-structure interaction algorithm can be improved introducing a variable under-relaxation parameter, thus enforcing the convergence. Alternatively, the current calculation scheme, including tight coupling, may be introduced in the current algorithm (2).

References

1. Shi Y, Zhao Y, Yeo TJH, Hwang NHC. Numerical simulation of opening process in a bilealflet mechanical heart valve under pulsatile flow conditions. *J Heart Valve Dis* 2003;12:245-56.
2. Dumont K, Vierendeels J, Verdonck PR. Feasibility study of the dynamic mesh model in Fluent for fluid-structure interaction of a heart valve. In: Brebbia CA, Arnez ZM, Solina F, Stankovski V (Ed.). *Simulations in biomedicine V*. Southampton: Wit Press; 2003. p. 169-176.
3. Dubini G, Redaelli A. Mesh updating in fluid-structure interactions in biomechanics: an iterative method based on an uncoupled approach. *Ann Biomed Eng* 1997;25(1):218-31.
4. Makhijani VB, Yang HQ, Dionne PJ, Thubrikar MJ. Three-dimensional coupled fluid-structure simulation of pericardial bioprosthetic aortic valve function. *ASAIO J* 1997;43:M387-M392.
5. Cheng R, Lai YG, Chandran KB. Two-dimensional fluid-structure interaction simulation of bileaflet mechanical heart valve flow dynamics. *J Heart Valve Dis* 2003;12:772-80.
6. Barbaro V, Grigioni M, Daniele C, Boccanera G. Reconstruction of closing phase kinematics by motion analysis for a prosthetic bileaflet valve. In: Power H, Brebbia CA, Kenny JM (Ed.). *Simulations in Biomedicine IV*. Southampton: Wit Press; 1997. p. 349-58.

FLOW-DYNAMICS OF THE ST JUDE SYMMETRY AORTIC CONNECTOR VEIN GRAFT ANASTOMOSIS DO NOT CONTRIBUTE TO THE RISK OF ACUTE THROMBOSIS

Alberto Redaelli (a), Francesco Maisano (b), Giuseppe Ligorio (a), Enrico Cattaneo (a), Franco Maria Montevecchi (b), Ottavio Alfieri (b)
(a) Dipartimento di Bioingegneria, Politecnico di Milano, Milan, Italy
(b) Unità cardiotoracica, IRCCS San Raffaele, Milan, Italy

Introduction

Miniaturization of the devices and improved biocompatibility allowed recent introduction of anastomotic devices for coronary artery by-pass grafting surgery (1, 2). Theoretical advantages of automated anastomoses include: standardization of the anastomosis, rapidity and easy of use, and, more interestingly, the possibility of performing a "clampless" proximal anastomosis on the ascending aorta. The St Jude Symmetry TM aortic connector is a nitinol endovascular device that enables sutureless end-to-side anastomosis between a venous graft and the ascending thoracic aorta. Drawbacks of the connector are the presence of a endolouminal stent-like nitinol structure, the necessity of manipulation of the vein graft during the preparation for delivery and the obligatory 90° offspring of the venous graft from the aorta, leading to higher risk for kinking and compression of the graft from the mediastinal structures. Possibly related to this issue there have been several reports of acute thrombosis of the vein graft, particularly at the proximal end of the graft (3-5). Local hemodynamic factors are involved in atherosclerotic plaque formation and development: "disturbed flow" may induce initial endothelial lesions and inflammatory activation with possible platelet aggregation and acute thrombosis. To determine whether proximal geometry of the offspring of the anastomosis from the ascending aorta may induce flow disturbances we designed a computational approach in order to compare the flow and wall shear stress patterns between conventional hand-sewn and automated proximal anastomosis geometries.

Materials and methods

Figure 1 depicts the six models of proximal anastomosis used in the present study.

Four models reproduce the typical morphology of a conventional hand-sewn anastomosis and differ for the angle between the graft axis and the aortic conduit; angles of 45, 90, 135, 180 degrees were considered. The other two models simulate the anastomoses performed with the aortic connector; they differ in the length of the straight portion of the graft upstream from the bending, which is 3 cm and 0.3 cm, respectively. For all models, the ascending aorta and the graft diameters were assumed equal to 3.5 cm and 0.5 cm, respectively; the graft was connected 2.3 cm downstream of the aortic inlet section and the length of the proximal graft was set equal to 5.4 cm. In order to obtain uniform outlet pressures the aortic conduit was assumed to be a 25 cm long straight tube; for the same purpose, a 2.6 cm long straight conduit was added at the end of the graft.

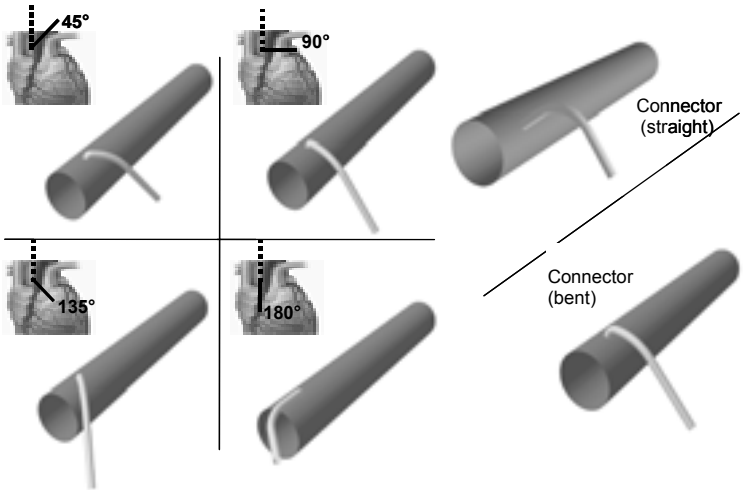

Figure 1. The four models on the left represent the hand-sewn anastomoses (angle between the graft axis and the aortic conduct is 45, 90, 135, 180 degree, respectively). The two models on the right represent the anastomoses performed with the aortic connector with respect to a standard case and a critical one

The graft walls were assumed to be rigid and no slip conditions were imposed. The numerical simulations were obtained under unsteady flow conditions. The flow rate profile by Swanson and Clark (6) was used at the aortic inlet, with an average flow rate of 5 L/min. The graft flow rate was calculated on the basis of the results obtained by a detailed numerical-distributed non-linear model of coronary by-pass circulation (7). In order to provide the correct diastolic graft inflow conditions, the aortic wall was assumed compliant; the Laplace law was used to calculate diastolic-to-systolic variation of the inner diameter of the aorta, by assuming the vessel thickness equal to 1 mm and the aortic elastic modulus equal to 1 MPa.

The fluid was assumed to be an isotropic, homogenous, incompressible and Newtonian fluid with a constant density (1060 kg/m^3) and viscosity (0.0033 Pa·s).

The Finite Volume Method (Fluent Inc. Lebanon, Illinois) was adopted to solve the Navier-Stokes equations. For the domain discretization the hexahedral meshing technique was used (approximately 230.000 cells).

Two fluid dynamics indexes were used to evaluate the Wall Shear Stresses (WSS), the Time Average WSS value (TAWWS) and the Oscillating Shear Stress Index (OSI). These indexes are used to identify low and oscillating WSS regions, usually associated with bifurcating flows and vortex formation that are strictly related to atherosclerotic plaques formation and fibrointimal hyperplasia (8-10).

Results

Figure 2 shows the vortex area downstream of the anastomosis during the systolic phase. This vortex is the consequence of the rapid change of direction experienced by the fluid entering the graft; such a behaviour is typical of small vessels originating from large vessels in which the blood flow is characterized by high velocities. During diastole, the flow rate inside the graft reaches its maximum value because of the coronary pressure reduction, which depends on the

cardiac muscle relaxation. In this case, the models simulating the hand-sewn anastomoses still show a vortex area, while in the anastomoses performed with the aortic connector, the path lines are parallel and no vortex occurs.

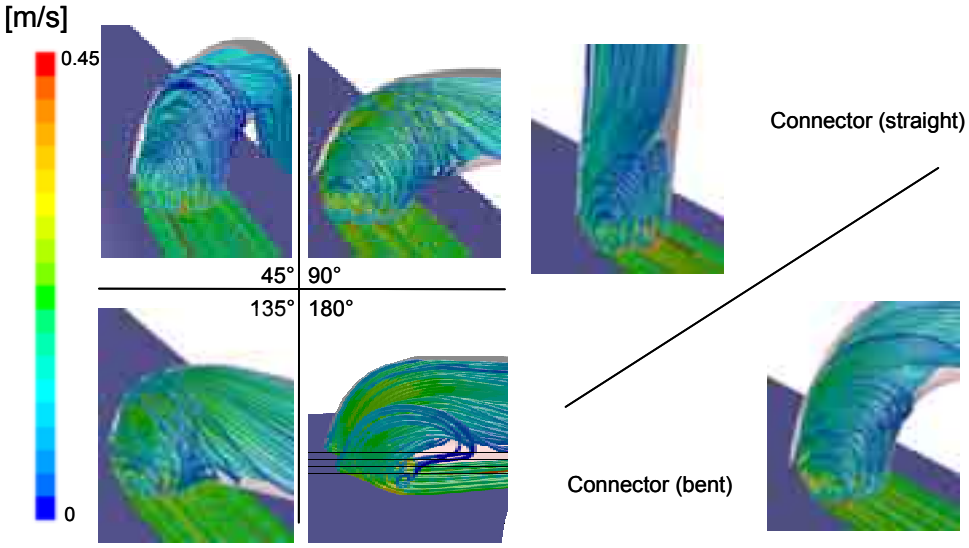

Figure 2. Path lines coloured with respect to the maximum velocity value at the systolic peak

Concerning the WSS, in the models simulating the hand-sewn anastomoses, low and oscillating WSS occur at the toe and heel regions respectively. Table 1 reports the TAWSS and OSI indexes in the two regions.

Table 1. WSS indexes

Bypass	zTAWSS(Pa)	zOSI	minTAWSS(Pa)	maxOSI
Toe region				
45°	0.60	0.25	0.35	0.41
90°	0.80	0.09	0.50	0.14
135°	0.99	0.04	0.59	0.08
180°	0.99	0.01	0.68	0.06
Connector (3 cm)	1.09	0.04	0.68	0.17
Connector (0.3 cm)	0.99	0.06	0.81	0.08
Heel region				
45°	0.40	0.16	0.26	0.38
90°	0.45	0.13	0.29	0.39
135°	0.39	0.12	0.25	0.42
180°	0.28	0.17	0.16	0.35
Connector (3 cm)	1.05	0.04	0.67	0.17
Connector (0.3 cm)	1.59	0.07	1.09	0.13

TAWSS and OSI values calculated in the toe and heel regions; zTAWSS and zOSI are the average values on the region. The table also reports the maximum and minimum TAWSS and OSI values in the investigated region.

Table 1 also reports their average value calculated with respect to an area of 0.1 cm^2. In the toe region, in the four models of hand-sewn anastomoses, the numerical results shows that low WSS are not associated to high OSI values, with the exception of the 45 degree configuration. On the other hand, high OSI values are present in the heel region in concomitance with low TAWSS. According to these results the most critical model is the 45° model of hand-sewn anastomosis, where the probability of pathological thickening is high both in the toe and in the heel regions. The most critical region is the heel one; the models simulating the anastomoses performed with the aortic connector show a significative improved fluid dynamics (TAWWS 1.32±0.04 Pa mean±SD *vs* 0.38±0.07 Pa; OSI 0.6±0.02 Pa *vs* 0.15±0.02 Pa). Eventually, the critical configuration simulating the graft bending 0.3 cm downstream of the anastomosis is characterised by the highest TAWSS value (1.59) due to the skewness of the velocity profile and by a OSI value of 0.07 which is intermediate between the extremely low value of the 3 cm straight anastomosis (0.04) and the hand-sewn anastomoses (0.15±0.02 Pa).

Discussion

Initial clinical experience with the anastomotic devices has been associated with a significative incidence of early graft thrombosis and late occlusion (3,4). However, according to the simulations results, the geometry of the proximal anastomomosis obtained with the Symmetry aortic connector leads to more favourable flow patterns than the conventional hand-sewn anastomosis. The 90° offspring of the anastomosis is associated with more regular flow patterns, higher diastolic wall shear stresses, and lower OSI index values. As a consequence a TAWWS value larger than 0.5 Pa is obtained throughout the cardiac cycle, which is not correlated to the formation of fibrous plaques (8). Similarly, the value of OSI, which is linearly related (r=0.6) to the occurrence of atherosclerosis (9), is strongly reduced. Consequently, factors responsible for early and late failure of the aortic connector may include insufficient biocompatibility of the device, procedural-specific manoeuvres (graft manipulation and necessity of performing the proximal anastomosis first) and the geometrical conformation (90° offset of the vein graft from the ascending aorta) which has a twofold implication: it may induce graft kinking and abnormal fluid dynamics (1). The presence of a nitinol structure inside the proximal anastomosis opens a number of questions about the biocompatibility of the St Jude Symmetry device, and resembles the situation of a stent. The automated anastomosis procedure involves several manipulations of the vein graft, that is “cannulated” on a mounting device in preparation to be deployed, with consequent contact of the endothelial surface with the device. Although the device has only smooth surfaces, this manoeuvre contradicts the no-touch technique on the vein graft.

References

1. Maisano F, Franze V, De Bonis M, Alfieri O. Off-pump coronary artery surgery with the use of anastomotic devices: an additional tool for the challenging patient. *Heart Surg Forum* 2002;5:25-7.
2. Hornik L, Tenderich G, Minami K, Fassbender D, Schulz TO, Beinert B, Koerfer R. First experience with the St Jude Medical, Inc, Symmetry Bypass System (Aortic Connector System). *J Thorac Cardiovasc Surg* 2003;125:414-7.
3. Donsky AS, Schussler JM, Donsky MS, Roberts WC, Hamman BL. Thrombotic occlusion of the aortic ostia of saphenous venous grafts early after coronary artery bypass grafting by using the Symmetry aortic connector system. *J Thorac Cardiovasc Surg* 2002;124:397-9.

4. Traverse JH, Mooney MR, Pedersen WR, Madison JD, Flavin TF, Kshettry VR, Henry TD, Eales F, Joyce LD, Emery RW. Clinical, angiographic, and interventional follow-up of patients with aortic-saphenous vein graft connectors. *Circulation* 2003;108:452-6.
5. Cavendish JJ, Penny WF, Madani MM, Keramati S, Ben-Yehuda O, Blanchard DG, Mahmud E, Perricone A, Tsimikas S. Severe ostial saphenous vein graft disease leading to acute coronary syndromes following proximal aorto-saphenous anastomoses with the symmetry bypass connector device: is it a suture device or a "stent"? *J Am Coll Cardiol* 2004; 43:133-9.
6. Swanson WM, Clark RE. Cardiovascular system simulation requirements. *J Bioeng* 1997;1:121-33.
7. Rammos KSt, Koullias GJ, Pappou TJ, Bakas AJ, Panagoupulos PG, Tsangaris SG. A computer model for the prediction of left epicardial coronary blood flow in normal, stenotic and bypassed coronary arteries, by single or sequential grafting. *Cardiovasc Surg* 1998;6:635-48.
8. Giddens DP, Zarins CK, Glagov S. The role of fluid mechanics in the localization and detection of atherosclerosis. *J Biomech Eng* 1993;115:588-94.
9. Keynton RS, Evancho MM, Sims RL, Rodway NV, Gobin A, Rittgers SE. Intimal hyperplasia and wall shear in arterial bypass graft distal anastomoses: an *in vivo* model study. *J Biomech Eng* 2001;123:464-73.
10. Ku DN, Giddens DP, Zarins CK, Glasov S. Pulsatile flow and atherosclerosis in the human carotid bifurcation. *Arteriosclerosis* 1985;5:293-302.

IMAGING AND NUMERICAL FLUID DYNAMICS FOR THE STUDY OF THE CARDIOVASCULAR SYSTEM

Luca Antiga
Dipartimento di Bioingegneria, Istituto Mario Negri, Ranica (BG), Italy

Introduction

Vascular disease is in general driven by systemic factors, such as biochemical or familiar factors, and local factors, such as the local hemodynamic environment and its history in the vicinity of the diseased territories. Atherosclerosis, for example, the most representative vascular disease in the Western world, is focal in nature, its lesions being localized at bifurcations or tracts of high curvature giving rise to complex flow patterns in the vicinity of the vessel wall (1). The very tissue components which the atherosclerotic plaque is made up of present distinct patterns of spatial organization and heterogeneity which are likely related to the hemodynamic milieu during the history of plaque growth. Plaque instability and rupture are also likely related to flow-related wall stress environment and focal inflammatory processes.

The hypothesis which relates hemodynamics to vascular pathology is corroborated by several studies in the field of cellular biology, in which the behavior of cultured endothelial and smooth muscle cells exposed to flow has been characterized. The picture drawn from these studies can be roughly summarized in the statement that complex flow and low and oscillating wall shear stress elicit an atherogenic behavior on the vessel wall (1), in terms of endothelial cytoskeletal rearrangement, proliferation, increase in permeability, expression of adhesion proteins, monocyte recruitment. On the contrary, unidirectional (even if unsteady) sustained flow and wall shear stress induce the endothelium to assume an actively athero-protective phenotype.

While it is possible to impose flow patterns and wall shear stress distributions on monolayers of cultured cells perfused under controlled conditions, measuring the same quantities non invasively *in vivo* is still a challenging task. Time-resolved velocity waveforms can be obtained with Doppler ultrasound (US) examination, although the information is limited to single sample volumes, while cross-sectional (or even volumetric) velocity distributions can be obtained with phase contrast magnetic resonance angiography (PC-MRA) sequences. However, the resolutions achievable so far are not sufficient to provide near-wall velocity vectors and derive wall shear stress distributions without regularity assumptions on near-wall velocity profiles.

Computational Flow Dynamics (CFD) has been proved to be a valuable tool in engineering over the last decades. Since the eighties, the potentiality of CFD as a tool to investigate blood flow has been sought, even though the limited computational resources posed a bound on the complexity of the models, especially as to the geometry of the computational domains. The first successful computational study showing some correlation between atherosclerotic lesion initiation and low and oscillatory wall shear stress has been led by Ku *et al.* (2) back in 1985, in which wall thickness from vascular wall specimens of carotid bifurcations were compared with wall shear stress values obtained computationally on a symmetric idealized carotid bifurcation model at corresponding locations. This work triggered a number of studies on the use of CFD to predict locations of low and oscillating wall shear stress, although the expected statistically significant correlations did not appear so evident as in the original study.

During the years, computational models of blood flow in vessels has been improved in several ways. Simulations has been performed in three-dimensions (3D) without resorting to

non-physiological symmetries, viscosity models other than Newtonian have been explored, the rigid walls assumption has been relaxed with the introduction of fluid-structure interaction codes. We will explore the significance of these advances during the course of this manuscript. However, the technical development which led to the most significant leap towards *in vivo* characterization of blood flow patterns has been the introduction of 3D non invasive imaging modalities (such as Computed Tomography – CT – and MR) and image processing techniques capable to accurately model vascular wall geometry. The coupling of image-based geometric modeling with CFD (3), first exploited in the early nineties, has opened the possibility to directly investigate the relationships between flow patterns and vascular disease in a subject-specific manner. In this context, Doppler US or PC-MRA have been employed to provide boundary conditions to CFD models.

Although a number of studies have been conducted in the field of image-based blood flow modeling, a final word on the quantitative relationships between flow conditions and vascular disease has not been stated yet. This might be due to several reasons, such as the inherent complexity of cellular mechanotransduction pathways, the 3D arrangement of several cell types interacting with each other and with the extracellular matrix within the vascular wall, the coupling between the effects of shear stress, tensile stress, passive and active transport of macromolecules, circulating inflammatory cell rolling, adhesion and extravasation, platelet activation, all of which contribute, together with systemic factors, to the development of focal atherosclerotic lesions. However, there are other factors that potentially contribute to obfuscate the relationship between wall shear stress and vascular disease, which necessarily have to be investigated before more complex models are elaborated. We here cite a few, such as the precision and accuracy of the computed flow-related quantities and the lack of proper tools for the analysis of the results obtained from population studies. In the following, we will try to address these relatively new issues and to summarize the major results obtained so far.

Precision and accuracy of predictions

Validation of the results of computational fluid dynamics can be performed at several levels. It first plays an important part in the development of reliable CFD codes, for which analytical solutions are employed on relatively simple test cases and controlled experiments are used to test for more sophisticated problems. In addition, to check whether the adoption of a computational model is adequate for modeling a given physical phenomenon, validation studies have to be performed to assess the errors related to model assumptions, uncertainty in domain definition and in the imposition of boundary conditions.

Several works have been carried out regarding the validation of CFD solutions in realistic physical models of blood vessels. Particle Imaging Velocimetry (PIV) and Laser Doppler Anemometry (LDA) have been successfully employed to this end in realistic physical models of vasculature, and of course carry a great potential on their own as to the basic understanding of fluid dynamics in complex bends or bifurcations. This kind of validation studies ensure that, once a computational mesh and boundary conditions are available, modeling errors are bounded. Although fundamental as a starting point, this kind of validation does not ensure that a model is actually reproducing what happens *in vivo*.

Validating *in vivo* flow patterns is a challenging task, mainly because to date no methodologies can adequately resolve flow dynamics, let alone non-invasively. Validation in this case can come from the simulation of image formation processes underlying clinical flow imaging modalities such as Doppler US, PC-MRA, or X-ray angiography. By virtually imaging computational models of blood vessels and comparing the resulting images with clinical data

acquired under the same conditions, it is possible to infer the correctedness of the computed flow fields with respect to the *in vivo* situation, even though the resolution with which this kind of indirect validation is performed is not comparable with that obtained through PIV or LDA.

The major problem related to accuracy determination is the marked inter-subject variability in vascular geometry and systemic flow distribution, which results in high variability in local flow conditions. This aspect makes the determination of the truth against which a computational solution is validated a challenging task in itself, and poses the question of what error in accuracy can be considered clinically relevant. Most models are reconstructed from MR or CT scans in which patients are lying in supine position, and similarly for the determination of boundary conditions, so that vascular geometry and flow conditions might be different during the subject's everyday life. Therefore, at a first sight, it could be stated that, as long as a computational model is accurate to within inter-subject variability, the computed flow-related quantities are representative enough. At the same time, this would require that an average representative geometry and flow are taken into account, which might not be the case if the starting point is a clinical scan. If the problem looks unsolvable, a help can come from what routinely performed in determining blood pressure in patients. Pressure has its own variability, and the conditions under which measurements are taken in clinical settings are probably far from representative of everyday life. Nevertheless, pressure is a key quantity for a huge amount of clinical problems, thanks to the number of clinical trials performed over the years that test its clinical relevance. The take-home message is therefore to make computational estimates of flow-related quantities available to evidence-based medicine, which can in turn determine the clinical relevance of the computed quantities as a separate step.

Related to accuracy, and a necessary complement to that, is precision. Measuring reproducibility is an easier task than determining accuracy, since knowledge of the truth is not needed. In fact, while no actual study on accuracy has been performed, a few studies on reproducibility of *in vivo* hemodynamic modeling has been published, the most relevant being the concurrent works of Thomas (4) and Glor (5), both performed on the human carotid bifurcation. In the first study, three subjects were imaged three times at weekly intervals, while in the second, eight subjects were imaged twice 2 to 4 weeks apart. While performed using different tools operating on different MR sequences, both works evidenced an overall error of about 10% in determining lumen geometry, while an error of about 30% to 40% in determining WSS (Wall Sheet Stress). Most of the error in WSS was demonstrated to be due to variability in the acquisition and reconstruction of lumen geometry, and only a minor part was ascribable to variability in hemodynamic boundary conditions. The errors presented by both studies are huge if compared to the precisions aimed for in phantom-based validation studies, nevertheless these are the errors that must be accounted for in designing a population study. It is likely that precision will be improved in the future by adopting better imaging scanners, such as new generation 3 Tesla MR scanners, and better modeling tools. Still, any study aimed to document the difference in a flow-related quantity between two populations will not have to be considered clinically significant if the observed differences, even if statistically significant, are within the range of the error in reproducibility.

The positive message of the reproducibility studies in question is that, while errors in the absolute values of hemodynamic quantities were found to be high, the overall patterns of their surface distributions turned out to be reproducible from a qualitative point of view. This is likely to be a relevant finding in the context of clinical studies. The fact that areas of low or high wall shear stress can be localized with a certain degree of confidence on a subject-specific manner is a solid basis for clinical observations. This is even clearer if we consider that, on the cellular biology side, a precise WSS range which triggers atherogenic behaviors has not yet been identified, the real trigger being probably a mixture of hardly quantifiable contributions of

local and systemic risk factors. In this hypothesis, locating areas of low and high WSS, or areas of high spatial and temporal variation of WSS, is to be considered of great impact from a biological point of view.

The role of open source projects

Given the finding that errors in geometry are amplified when hemodynamics comes into play, 3D modeling and mesh generation must be performed with the highest accuracy and precision and the lowest operator-dependence. Although research has been active in this field, there is still a great deal of manufacturing involving operator-dependent tasks in performing 3D reconstruction and meshing from medical images. Typically, several different commercial software packages are employed, from CAD packages to mesh generators, which are designed to solve industrial design problems rather than to deal with realistic vascular geometries. Furthermore, the licensing policies adopted in such packages do not allow one to understand the exact implementations of the algorithms employed. As a result, the modeling procedure has to adapt to what the tools expose to the user rather than the opposite.

These limitations are potentially overcome by relying on the growing number of open source projects available on the web, and possibly contributing to their development. Besides the advantage of being cost-free, they offer the unique opportunity of building consistent frameworks for streamlining image processing, 3D reconstruction, mesh generation and computational modeling. The reduction of operator-dependent tasks is achieved by a greater specialization of the tools, which are typically written or extended by researchers in the field. Research groups which don't have the strength or the interest of investing research years in tool development can readily use the state of the art to perform applied research. Last but not least, free availability allows a better quality of publications by making it possible to reproduce results.

We here name a few relevant open source projects

- Insight (www.itk.org): a library for image segmentation and registration
- Netgen (www.hpfem.au/netgen): a mesh generation application and library
- Libmesh (libmesh.sourceforge.net): a library for finite elements computations
- VTK - the Visualization Toolkit (www.vtk.org): a library for 3D modeling and visualization
- vmtk - Vascular Modeling Toolkit (vmtk.sourceforge.net): a framework for pre- and post- processing for image-based modeling of vascular segments

The list, of course, does not want to be conclusive, but offers a good starting point for searching related or alternative projects on the similar topics.

Analysis of results in population studies

A pressing issue in image-based hemodynamic modeling applied to population studies is data analysis. Flow-related quantities are typically distributed over complex 3D surfaces, whose shape is subject to high variability. Comparing two distributions of WSS defined over the surfaces of vessels with different geometry is not a trivial task, and it potentially introduces bias in the final results. If we recall the importance of reproducibly in estimating subject-specific spatial patterns of hemodynamic quantities, the need of data analysis methods capable of comparing such patterns over populations is of primary importance.

A possible solution to this problem has been proposed in a recent work by the author (6), which consists in cutting and unfolding the surface of a bifurcating vessel onto a rectangular parametric space. This is achieved through the definition of geometric quantities which solely rely on vessel shape and do not require operator decisions. The method is designed so to yield similar cutting and flattening results if applied to similar vessels. The implementation of the method and further extensions have been made available in the vmtk library.

Once each branch of a complex vascular structure is mapped onto a rectangular space, comparison of surface distributions of flow-related quantities in populations can be performed quantitatively with the help of univariate or multivariate statistical methods. The identification of proper statistical tools is yet one more challenge towards the application of image-based flow modeling on populations.

Conclusions

In this report we tried to give a brief overview on some of the problems arising in the application of image-based numerical modeling of blood flow to studies on populations. The problem is, once again, interfacing theory- and experiment-driven engineering with evidence-based medicine. While a lot of work has been carried out over the years on computational modeling and new developments are steadily being pursued, a few aspects still need to be explored before numerical modeling can become a widely recognized tool for clinically relevant studies. This will necessarily require the involvement of clinicians and cellular biologist in modeling studies and the constitution of interdisciplinary research groups.

Acknowledgments

The author would like to thank D.A. Steinman for the fundamental discussions on most of the topics presented in this manuscript.

References

1. Malek AM, Alper SL, Izumo S. Hemodynamic shear stress and its role in atherosclerosis. *JAMA* 1999; 282(21):2035-42.
2. Ku DN, Giddens DP, Zarins CK, Glagov S. Pulsatile flow and atherosclerosis in the human carotid bifurcation. Positive correlation between plaque location and low oscillating shear stress. *Atherosclerosis* 1985;5(3):293-302.
3. Steinman DA Image-based CFD modeling in realistic arterial geometries. *Ann Biomed Eng* 2002;30(4):483-97.
4. Thomas JB, Milner JS, Rutt BK. Reproducibility of computational fluid dynamics models reconstructed from serial black blood MRI of the human carotid bifurcation. *Ann Biomed Eng* 2003;31(2):132-41.
5. Glor FP, Long Q, Hughes AD, Augst AD, Ariff B, Thom SA, Verdonck PR, Xu XY. Reproducibility study of magnetic resonance image-based computational fluid dynamics prediction of carotid bifurcation flow. *Ann Biomed Eng* 2003;31(2):142-51.
6. Antiga L, Steinman DA. Robust and objective decomposition and mapping of bifurcating vessels. *IEEE Trans Med Imaging* 2004;23(6):704-13.

MULTISCALE MODELS OF THE CARDIOVASCULAR SYSTEM APPLIED TO THE STUDY OF THE FLOW IN A CAROTID BIFURCATION

Rossella Balossino (a), Francesco Migliavacca (a), Giancarlo Pennati (a), Gabriele Dubini (b), Christian Vergara (c), Luca Formaggia (c), AlfioVeneziani (c)
(a) Dipartimento di Bioingegneria, Politecnico di Milano, Milan, Italy
(b) Dipartimento di Bioingegneria Strutturale, Politecnico di Milano, Milan, Italy
(c) Dipartimento di Matematica, Politecnico di Milano, Milan, Italy

Introduction

The circulatory system exhibits a multiscale nature due to the strong relationships between local and systemic phenomena in the circulation. An accurate analysis of the flow in a specific sub-region should take into account the fact that every district is part of a complex and interactive circulatory system. Local haemodynamic is responsible for pressure changes which in turn affect the blood flow distribution in downstream and upstream vessels or organs. Since a precise description in terms of morphology as well as fluid dynamics behaviour of the whole circulatory system is impossible, a promising solution is the use of a heterogeneous mathematical model, coupling a local and accurate model of the district of interest with a simplified model of the remaining vascular system.

In our study we considered a carotid artery bifurcation as an example to highlight the important contributions that correct computational fluid dynamics simulations may give in the quantitative prediction of the haemodynamics. In more detail, the multiscale approach is here apply to two 3D models of a carotid bifurcation with or without a stenosis, respectively (Figure 1), and the results are also compared to a stand-alone 3D geometry of the same stenosed carotid model.

Mathematical model

We considered two different sub-models, a local one based on the 3D Navier-Stokes equations, and a global or systemic model based on a lumped-parameter representation derived from the analogy between hydraulic and electric networks.

A finite volume method was adopted for the 3D model to solve the mass and momentum conservation equations derived for an incompressible Newtonian fluid:

$$\begin{cases} \rho \dfrac{\partial \mathbf{u}}{\partial t} + \rho(\mathbf{u} \cdot \nabla)\mathbf{u} - \mu \nabla^2 \mathbf{u} + \nabla p = 0 \\ \nabla \cdot \mathbf{u} = \mathbf{0} \end{cases}$$

Lumped-parameter model (LM) provides a description of the whole circulatory system by suitable splitting into elementary districts or compartments, which are described by resistances (R), capacitances (C) and eventually inductances (L).

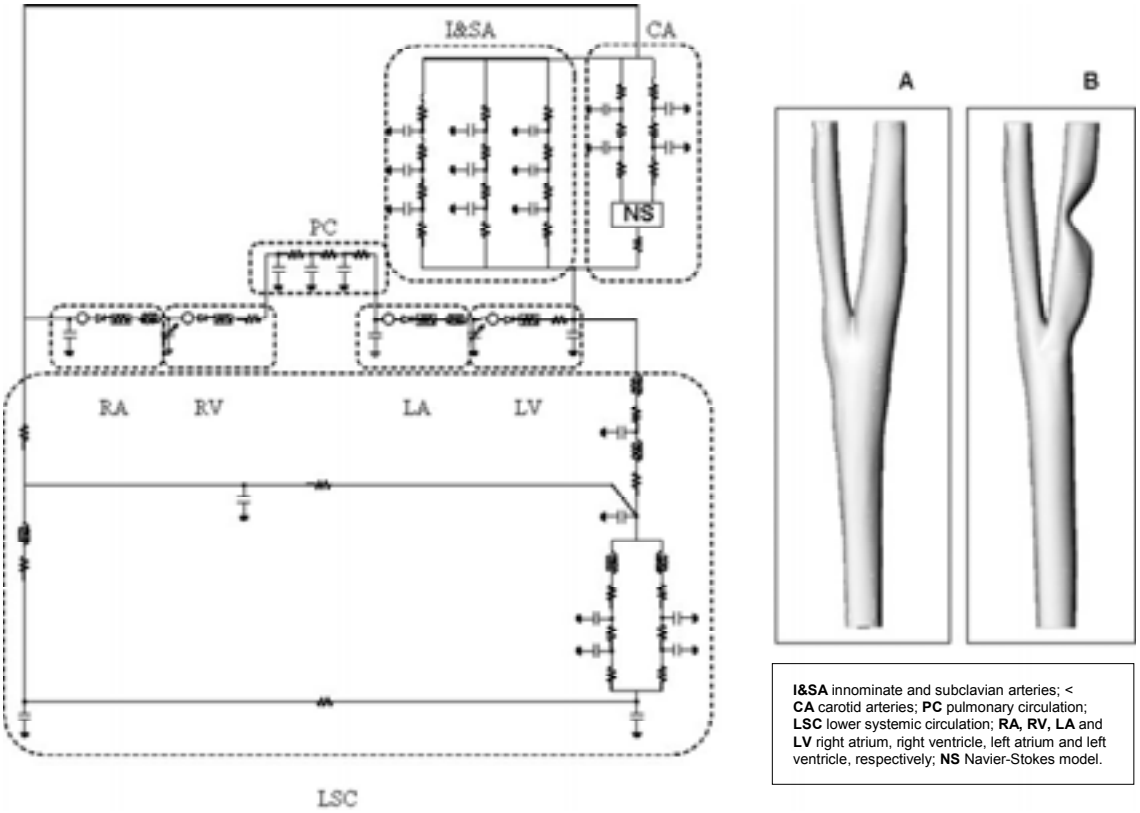

Figure 1. Lumped parameter model (left) of the circulatory system. Representation of the two 3D models (right) used in the simulations: A. healthy carotid artery and B. stenosed carotid artery

In each compartment the blood flow and pressures are modelled by ordinary differential equations, which can be obtained by simplification of the Navier-Stokes model. From the momentum and mass conservation laws, the following ordinary differential equations can be obtained

$$Q_{in}(t) - Q_{out}(t) = C \cdot \frac{\mathrm{d}P_{out}(t)}{\mathrm{d}t}$$

$$P_{in}(t) - P_{out}(t) = R\,Q_{in}(t) + L \cdot \frac{\mathrm{d}Q_{in}(t)}{\mathrm{d}t}$$

where:

$$R = \frac{8\mu l}{\pi R_o^4}, \qquad L = \frac{\rho l}{\pi R_o^2}, \qquad C = \frac{3\pi R_o^3 \left(1-\sigma^2\right) l}{2Eh}$$

while s, E and h denote Poisson ratio, the Young modulus and the thickness of the external wall, respectively. In particular we assume s = 0.5, which means that external wall of the vessel is incompressible. The whole system of ordinary differential equations (ODE) was then solved with an explicit Euler method by means of a user defined function included in the Fluent code (Fluent Inc, Lebanon, NH, USA).

The coupling between the two sub-models was accomplished by means of interface conditions: particularly pressures, calculated by the LM, are the boundary conditions applied to

the 3D model at the downstream and upstream sections. On the other hand the forcing terms in the ODE system depend on the interface volume flow rates calculated from the 3-D model. In this way the local velocity profiles are not forced but calculated at each time step in a fully coupled manner.

Numerical results

Two different simulations were carried out. In the former multiscale modelling was applied to two different geometries of a bifurcation carotid artery, while in the latter a stand-alone 3D model of the same stenosed carotid artery was considered as a comparison.

Computed tomography images of a carotid artery, (courtesy of M. Tuveri, Clinica S.Elena Quartu Cagliari, Italy) were imported into a 3D image processing and editing software, Mimics (Materialise Leuven, Belgium), and a model of a healthy artery with a rigid-wall was created. This geometry was then modified using a commercial modelling code, Rhinoceros (Robert McNeel & Assoc., Seattle, USA), in order to obtain a stenosed model of the same carotid artery. The minimum lumen area created was of 5.9 mm2 which, compared to the closest maximum area, correspond to a stenosis of 80% (Figure 1). A mesh was then generated with the commercial code Gambit, for both models using an unstructured grid of approximately 100,000 elements. The diameter of the common carotid artery was 6.4 mm.

The circuit shown in Figure 1 is assumed as a completely lumped parameter description of the global circulation. The network is divided into several subsystem: the heart, the pulmonary circulation, the upper and lower systemic circulation. Time varying elastances were used to model the ventricle and constant ones for the atria. Non linear resistances were adopted to describe the outflow or inflow from the valves.

In the multiscale approach the boundary conditions, previously described, are exchanged between the two submodels in a iteratively manner, avoiding any external prescription. In the stand-alone 3D model we imposed, as boundary conditions, a pulsatile velocity profile at the inlet section (whose waveform was derived from the multiscale simulations, in good agreement with the literature data), while fixed and equal pressure was prescribed at the outlet sections (since the velocity profiles are not well known a priori from experimental measures). A no slip condition was imposed at the vessel walls. Blood is assumed to have a constant dynamic viscosity of 0.004 cP and a mass density of 1060 kg/m3.

Four cycles were simulated to ensure that flow is truly periodic, with a period of 0.8 seconds, corresponding to a heart rate of 75 beats per minute.

Multiscale models

Figure 2 shows the velocity contour in the two models on a vertical cutting plane in a particular instant during systole using the same scale. An increment in the velocity values can be observed in correspondence of the stenoses, as a consequence of the reduced cross sectional area. At the outlet sections, in both models, the velocity values are similar, which means that the flow rates are also quite close, being the cross sectional area not so different. If we compare the flow rates in the two branches for both models, it can be noted that there is an almost equi-distributions, in the stenosed model, too, where a reduction could be expected in the right branch with respect to the left one because of the obstruction. In the stenosed model only a slightly lower percentage of flow rate passes in the left branch with respect to the right one (49,76% *vs* 50,25%), with a reduction in the mean total flow rate in the CA respect to the healthy case (5.33 *vs* 5.58 mL/s).

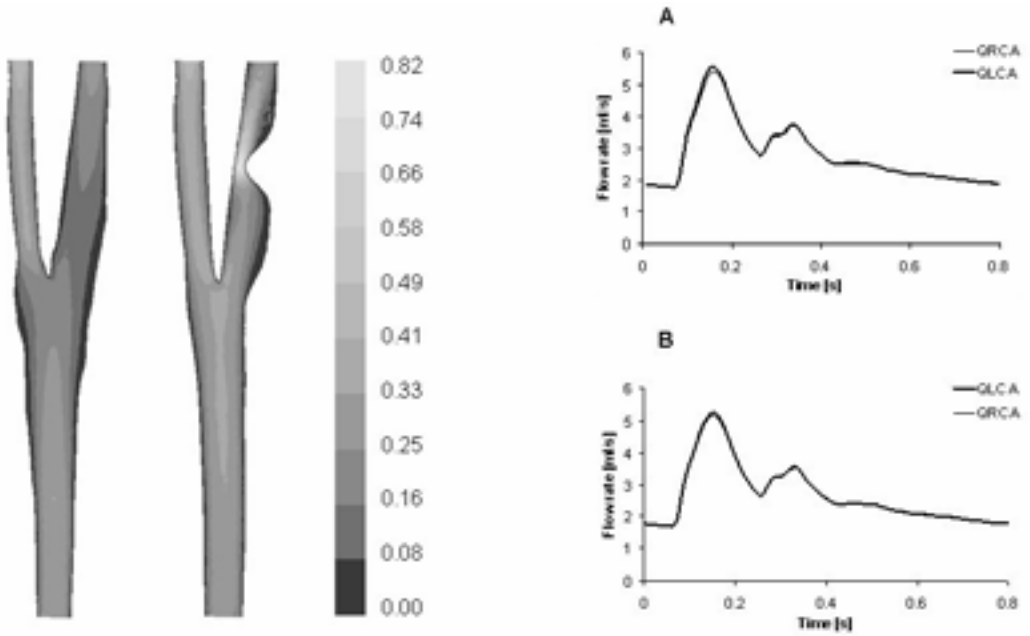

Figure 2. Velocity contour (left) on a cutting plane reported for a particular instant (t=0.2s) during systole; flow rates in the two branches for the healthy model (A) and the stenosed model (B)

Stand-alone 3D model

Figure 3 shows the results obtained with the stand-alone stenosed carotid artery model. In this case the prescription of a fixed pressure at the outlet sections causes a different flow rate distribution in the two branches according to the resistance encountered by the blood flow: due to the reduction of the cross sectional area in correspondence of the stenosis the resistance is very high, so the flow rate is higher in the left branch. In the multiscale model, instead, the resistances prescribed in the LM at the downstream of the outlet sections are greater since they account for the capillary arteries and, above all, the outlet pressures are not imposed, but vary in time according to what happens in the remaining part of the circulatory system. Flow rates are thus balanced by the pressure compensatory mechanism.

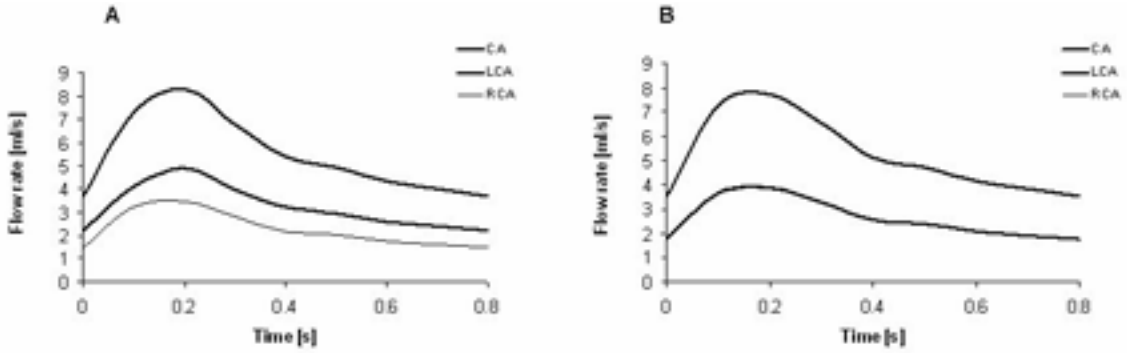

Figure 3. Comparison of the flow rates in the common (CA), left (LCA) and right (RCA) artery between the stand-alone 3D model (A) and the multiscale model (B)

Conclusions

It has been showed that a stand alone 3D model with unrealistic boundary conditions at the sub-region interfaces could give misleading results. The multiscale approach has, instead, the advantage that the boundary conditions are not forced but calculated and derived from the LM, representing the remaining part of the circulatory system without any external imposition. However, the multiscale model still suffers from some limitations such as the assumption of rigid artery wall in the 3-D model, the absence of any feed-back control (except for the Starling law of the heart) and the difficult identification of lumped parameter values.

References

1. Pietrabissa R, Quarteroni A, Dubini G, Veneziani A, Migliavacca F, Ragni S. From the global cardiovascular hemodynamics down to the local blood motion: preliminary applications of a multiscale approach. In: Oñate E, *et al*. (Ed.). *ECCOMAS 2000, Barcelona, 2000*.
2. Lagana K, Dubini G, Migliavacca F, Pietrabissa R, Pennati G, Veneziani A, Quarteroni A. Multiscale modelling as a tool to prescribe realistic boundary conditions for the study of surgical procedures. *Biorheology* 2002;39(3-4):359-64.
3. Quarteroni A, Veneziani A. Analysis of a geometrical multiscale model based on the coupling of PDE's and ODE's for Blood Flow Simulations. *Multiscale Modeling and Simulation: A SIAM Interdisciplinary Journal* 2003;1(2):173-95.

INTERACTIONS OF THE IMPLANTABLE CARDIOVASCULAR MEDICAL DEVICES WITH MR PROCEDURE: A REVIEW

Rossella Canese (a), Giuseppe D'Avenio (b), Perla Filippini (b), Franca Podo (a), Mauro Grigioni (b)
(a) Dipartimento di Biologia Cellulare e Neuroscienze, Istituto Superiore di Sanità, Rome, Italy
(b) Dipartimento di Tecnologie e Salute, Istituto Superiore di Sanità, Rome, Italy

Introduction

Magnetic Resonance Imaging (MRI) is becoming an important tool in the diagnosis of pathologies which affect internal organs. It plays an important role also in the study of pathologies of the heart and large vessels. Moreover, MRI has been shown to provide accurate images of the coronary arteries and to be highly superior to echocardiography for the detection of the ischemic heart disease (1).

MRI analyses on patients or individuals with metallic implants cause interactions between the device and the magnetic fields necessary to the image encoding. Hence, the importance to know the physical phenomena underlying these interactions in order to evaluate risks and propose protection guidelines to be adopted for patients who would benefit form MRI examinations.

The present work overviews the tests generally performed to assess the safety of use a large variety of cardiovascular devices during a typical MRI examinations. Moreover, a short review is presented of the artifacts generally produced by this implantable devices on the MR image.

Cardiovascular implantable devices

Coronary arterial stents are the most widely utilised cardiovascular devices. Stents are currently made of a large variety of materials. Most of them are composed of "low carbon" stainless steel or cobalt alloy or tantalum. The 316 "low carbon" stainless steel in bulk form is non magnetic. However, the type of cold working required to create the complex shapes of the stents produces significant ferromagnetic domains within these devices (2).

Prosthetic heart valves are built with either metallic, or polymeric and/or carbonous materials. Titanium is the most used metal for its non ferromagnetic properties, high biocompatibility and mechanical properties similar to those of stainless steel. Cobalt based alloys and pyrolitic carbon are also frequently used materials in the construction of prosthetic heart valves.

Ferromagnetic materials are therefore generally present in the cardiovascular implantable devices.

Possible interactions

The potential risks arising from the MRI analysis in patients or individuals carrying cardiovascular implantable metallic devices are:

1) possible dislodgement during positioning of the patient within the magnet and during the analysis due to:
   - the attraction or ferromagnetic force directed toward the centre of the magnet;
   - the torque, by which the device tends to be aligned along the static magnetic field;
2) possible heating: the radiofrequency (r.f.) associated with pulsed gradients, used in MR imaging, can create currents in loop-shaped devices, such as valves and stents, and therefore cause local heating;
3) possible artifacts in the images caused by local magnetic field changes, produced by the ferromagnetic, paramagnetic and diamagnetic properties of the metallic devices.

Assessment of ferromagnetic attraction

For the quantitative assessment of the attraction or ferromagnetic force exerted on cardiovascular implantable devices a protractor is typically used (3-6). The protractor is a pendulum to which the device is tied by a thin suture material. The angle of deflection from the vertical is related to the electromagnetic force exerted by the static magnetic field on the device by the following formula:

$$F = m \cdot g \cdot \tan(\theta)$$

where m is the mass of the device g, is the gravity acceleration (9.81 m/s^2) and q the deflection angle from the vertical.

Assessment of torque

To the best of our knowledge only qualitative assessment of the magnetic field induced torque has been so far performed on cardiovascular implantable devices. The procedure consisted of the use of a flat plastic device, with a millimetre grid etched on the bottom. The devices were placed in the centre of the magnet, where the effect of the torque force is expected to be the highest. The tests have been performed with the device perpendicular to Bo and rotated in the axial plane, in order to encompass the full 360° rotation. A qualitative scale was used to report the results (3, 4, 6).

Assessment of heating

The determination of heating effects during a MR imaging analysis is complex because heating can be very localised.

For the assessment of local heating the devices are immersed in different types of materials during MRI analyses. A typical material used for these tests is a semisolid gel composed by hydroxyethyl-cellulose (HEC) in aqueous solution (91.58% water) along with 0.12 % NaCl (in order to have a dielectric constant of approximately 80 and a conductivity of 0.8 S/m at 64 MHz (4). Usually the devices are dipped in the gel and the temperature can be measured by a fluoroptic thermometer (with the thermometric probes placed in close contact with the exposed metallic portion of the device) before, during and immediately after the running of sequences which maximise the r.f. Specific Absorption Rate (SAR). Thermocouple and infrared camera can also be used to determine heating effects.

Artifacts

Two major effects occur when a metal implant is imaged with a MR system. Ferromagnetic materials can disturb the homogeneity of the static magnetic field, which results into distorted images. Conductive but not ferromagnetic materials may exhibit induced r.f. currents that lead to image distortion. The large variety of MRI techniques and the wide range of values for the parameters commonly used in clinical imaging make a classification of the artifacts impossible.

An artifact can be a void in the signal, a reduction in signal intensity, a reduction in the dimension of the visible lumen, a reduction in the signal intensity within the lumen, a distorsion in the image and a wrong collection of data with consequent hyperintensity signal spots.

Several studies showed typical artifacts in the MR images due to the presence of metallic devices (2-5, 7-9). The devices were dipped in solutions or materials which had the relaxation times comparable to those of human myocardial tissue and MR images were collected with the sequences commonly used in diagnostic clinical analyses.

Discussion

Several studies analysed the attraction and torsion force induced on stents (2, 3) and prosthetic heart valves by magnetic field values up to 1.5 T (4, 5). Some valve were also studied at 3.0 T (6).

The largest ferromagnetic force measured on a stent was minimal (27.6·10-6 N) compared to the force exerted by the beating heart (i.e., approximately 7.2 N). No stent has been report to align with the static magnetic field. The deflection angles measured for the prosthetic heart valves were less than 45° which is the limit adopted byn the ASTM guidelines (10), and represents an attraction force equal to the force on the implant due to gravity (its weight). Some valves gradually align with the magnetic field but this qualitative findings are not believed to present a hazard or risk for patient implanted with these devices and undergoing a MRI examinations (4). Neither attraction nor torque have been measured on biological prosthetic valves at 1.5 T (4, 5). The same result has been found for the prosthetic heart valves built in nitinol (nickel –titanium alloy) or in titanium at 3.0 T (6).

No heating has been observed on either stents (3) or valves (4, 5) *in vitro*. In all cases the temperature increases were smaller than 1°C. As already mentioned before full map of local temperature increases is hard to be obtained *in vitro*. However, possible hot spots produced on these devices can be reduced *in vivo* by blood flow.

Regarding artifacts they are mainly due to local magnetic field alterations caused by the magnetic materials of the cardiovascular devices. Usually there is a good correlation between ferromagnetic properties and the extent of the artifact. In fact, iron containing alloys and, to a lower extent, alloys composed of cobalt, nickel and chromium produce artifacts in the MR images. The cause of geometric distortion or localised signal changes in MR images is thought to be a reduction in radio frequency amplitude near the metallic prosthesis which is dependent on its shape (2). Geometry dependent artifacts were studied by Wang *et al*. (8) on stents. They used a 3D Gradient Echo (GE) sequence with short Repetition Time (TR) and large flip-angle, in order to emphasise the component of the artifact due to the susceptibility of the stent material (Figures 1a and b), and with long TR and small flip-angle, in order to highlight the shielding factor due to the geometry of the stent (Figures 1c and d). Different wefts in the same material (nitinol) produce different susceptibility or shielding artifacts. The extent of the artifacts is also determined by the selected pulse sequence (spin echo sequences produce a better spin phase refocussing than the gradient echo techniques) (3, 4) and by the parameters used for image

collection (long echo times induce higher signal losses due to susceptibility variations, than the short ones). The visibility of the lumen was studied by Van Holten et al. (9). They showed that the flip-angle can be optimised for each stent in order to allow a clear determination of their lumens. Figure 2 shows MR images of a stent made of ABI alloy (i.e. an alloy of silver and palladium with mechanical properties similar to those of stainless steel). The lumen is completely obscured by using currently used parameters (e.g. flip-angle = 90°), while it becomes completely visible at a larger flip-angle (250°). In non metallic devices the visibility of the lumen is also related to the angle between the device and the static magnetic field. In fact, as shown by Lenhart et al. (7), the artifact size increases with the angle, according to a non linear relationship (Figure 3). If the device is parallel to the magnetic field the visibility of the lumen is maximal, but a band-like artifact occurs at the end of the stent, in the direction of the read out (or frequency encoding) gradient (indicated by an arrow in Figure 3b).

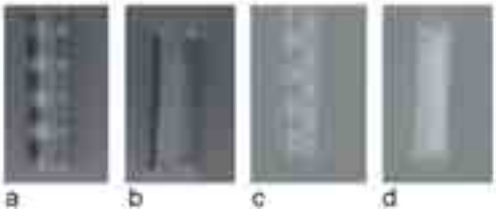

Figure 1. Typical examples of geometry dependent artifacts
(Reprinted with permission of Wiley/Liss, Inc., a subsidiary of John Wiley & Sons, Inc.) (8)

Figure 2. Flip-angle signal dependence within the lumen
(Reprinted with permission of Wiley/Liss, Inc., a subsidiary of John Wiley & Sons, Inc.) (9)

Figure 3. Typical examples of visibility of the lumen within 4 stents oriented perpendicular (a) and parallel (b) to the static magnetic field. The white arrows indicate the band-like read out artifact
(Reprinted with permission of Radiology Society of North America) (7)

Conclusions

Most of the coronary arterial stents and prosthetic heart valves are claimed to be safe for MR procedure in most of peer-reviewed reports. The cardiovascular devices of the new generations, which are built with new materials, may also be artifact free or induce minimal signal perturbation. These results suggest that MR analysis may, under appropriate conditions, be performed on these devices with minimal risk or loss of diagnostic information.

References

1. Lima JA, Desai MY. Cardiovascular magnetic resonance imaging: current and emerging applications. *J Am Coll Cardiol* 2004;44:1164-71.
2. Teitelbaum Gp, Bradley WG, Klein BD. MR imaging artifacts, ferromagnetism, and magnetic torque of intravascular filters stents and coils. *Radiology* 1988;166:657-64.
3. Hug J, Nagel E, Bornstedt A, Schnackenburg B, Oswald H, Fleck E. Coronary arterial stents: safety and artifact during MR imaging. *Radiology* 2000;216:781-87.
4. Edwards MB, Taylor KM, Shellock FG. Prosthetic heart valves: evaluation of magnetic field interactions, heating, and artifact at 1.5 T. *J Magn Reson Imaging* 2000;12:363-9.
5. Pruefer D, Kalden P, Schreiber W, Dahm M, Buerke M, Thelen M, Oelert H. *In vitro* investigation on prosthetic heart valves in magnetic resonance imaging: evaluation of potential hazards. *J Heart Valve Dis* 2001;10(3):410-4.
6. Shellock FG. Biomedical implants and devices: assessment of magnetic field interactions with a 3.0-tesla MR system. *J Magn Reson Imaging* 2002;16:721-32.
7. Lenhart M, Völk M, Manke C, Nitz WR, Strotzer M, Feuerback S, Link J. Stent appearance at contrast-enhanced MR angiography: *in vitro* examination with 14 stents. *Radiology* 2000;217:173-8.
8. Wang Y, Truong TN, Yen C, Bilecen D, Watts R, Trost DW, Prince MR. Quantitative evaluation od susceptibility and shielding affects of nitinol, platinum, cobalt-alloy, and stainless steel stents. *Magn Reson Med* 2003;49:972-6.
9. Van Holten J, Wielopolsky P, Bruck E, Pattynama PMT, van Dijk LC. High flip angle imaging of metallic stents: implications for MR angiography and intraluminal signal interpretation. *Magn Reson Med* 2003;50:879-83.
10. American Society for Testing and Materials (ASTM). Designation: F 2052. Standard test method for measurement of magnetically induced displacement force on passive implants in the magnetic resonance environment. In: *Annual book of ASTM standards. Section 13: Medical devices and services. Volume 13.01: Medical devices; emergency medical services.* West Conshohocken, PA: ASTM; 2002. p 1576-1580.

A NOVEL METHOD FOR TORQUE MEASUREMENT ON IMPLANTABLE MEDICAL DEVICES BY NMR AT 4.7 T

Giuseppe D'Avenio (a), Rossella Canese (b), Franca Podo (b), Mauro Grigioni (a)
(a) Dipartimento di Tecnologie e Salute, Istituto Superiore di Sanità, Rome, Italy
(b) Dipartimento di Biologia Cellulare e Neuroscienze, Istituto Superiore di Sanità, Rome, Italy

Introduction

The use of NMR techniques is widespread in the clinical field. The growing need for higher resolution calls for increasing static fields (1), so that nowadays systems working at fields of 4 T are not so uncommon as in the past, and it is foreseen that even more stronger static fields will be exploited in the future. The question may be posed if cardiovascular implants, that are often the outcome of past technological developments, can withstand not only the NMR exposure of the last generations' systems, but also the static fields that can be used in more modern equipment.

The present paper is meant to contribute to such an assessment, by proposing a new method for the measurement of the torque resulting from the interaction between static field and biomedical device.

Materials and methods

The torque T acting on a biomedical device in a magnetic field is measured with a torsion balance, which is suited for the measurement of very tiny forces. In fact, this type of device enabled Cavendish to measure *G*, the universal constant of gravitation, in 1798. Cavendish used a torsion balance to measure the force with which a small lead ball was attracted to a larger ball.

For this specific application, a copper wire was used as the elastic element in the balance, on account of its diamagnetic properties. The wire was inserted in a perspex holder, snugly fitting the cradle to be inserted in the NMR scanner (Varian Inova 200/183 operating at 4.7 T). We tested, in particular, a prosthetic heart valve (SJ 27 mm): the wire was wound twice on the valve's housing ring, and the two free ends were firmly attached by adhesive tape to the holder, after having been inserted in two holes located at two opposite points of the latter. The wire was tightly pulled, so that only the orientation of the valve (represented by the angle α between the valve plane and the scanner's axis) was allowed to vary during the experiment. In order to assure that the valve was subjected only to the torque parallel to the wire, thereby excluding the possibility of inclination due, e.g., to the torque directed normally to the wire, the part of the housing ring opposite to that anchored to the copper wire was held in contact with the latter by means of a thin cotton string. As confirmed by the experiments, the movements of the valve due to the normal component of the torque were largely limited by this arrangement.

A small-area reflecting surface was positioned on the valve's sewing ring, perpendicular to the valve plane, and held in place with adhesive tape. The deflection angle was measured by projecting a laser beam (He-Ne laser, 35 mW CW), parallel to the magnet axis, on the valve-mounted mirror, and by recording the longitudinal position (x) of the spot reflected by the latter. In this way, an optical pendulum was built, which allowed indirect determination of the angle

by means of a formula, reported in the following, relating the spot location x to the angle α between the device and the scanner axis.

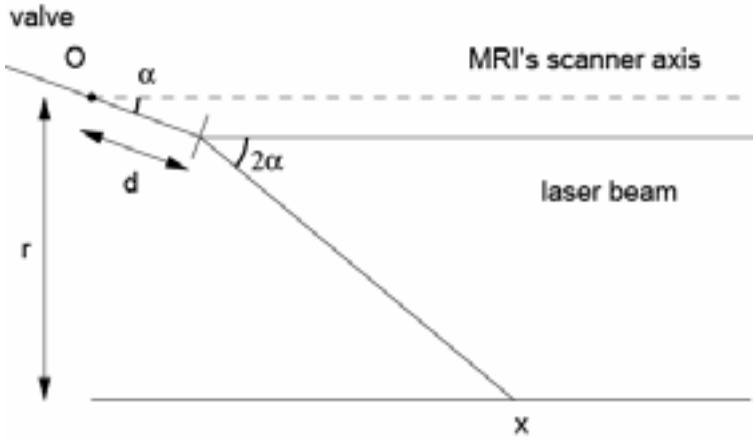

Figure 1. Path of the laser beam, reflected by the medical device on the MRI cradle's inner side at the axial location x

In Figure 1 the scheme of the measurements is shown, with the laser beam reflected on the inner side of the MRI cradle. After some straightforward calculations, it can be seen that the relationship between x and the angle α is given by

$$x = d\cos\alpha + (r - d\sin\alpha)\tan\left(\frac{\pi}{2} - 2\alpha\right) \qquad [1]$$

where *r* denotes the radius of the cradle and *d* is the distance between the torsion wire and the reflector positioned on the valve's sewing ring.

After preliminary trials, it was found that the area of the reflecting element mounted on the valve was too large to enable accurate measurements of the angle, thus the reflecting surface was covered with a piece of adhesive tape, punched in the middle so that only a small area (a circle of around 0.5 mm diameter) of the mirror could reflect the incoming light. Then, a small spot was projected on a graduated scale placed on the cradle.

The torque exerted on the valve caused the wire to rotate by an angle α, corresponding to the equilibrium between the torque due to the magnetic field and the reaction torque of the wire. Since the device was in contact with the wire in correspondence to a single point, ideally, the wire itself can be thought of as being decomposed in two parts (whose length is denoted as l_1 and l_2, respectively), both rotated by α. Then the torque tending to move the valve back to the initial angle (α_0) was given by $T = T_1 + T_2$, where

$$T_1 = \frac{(\alpha - \alpha_0)JG}{l_1} \qquad [2a]$$

$$T_2 = \frac{(\alpha - \alpha_0)JG}{l_2}; \qquad [2b]$$

here J is the polar moment of inertia of the wire segment (defined as $J = \frac{\pi}{2}r^4$, r being the wire radius), and G is the shear modulus of copper.

Two set-ups were adopted, one with D=0.18 mm, and the other with D=0.30 mm, while maintaining fixed the wire lengths l_1 and l_2. Thus, at the same value of the torque T, different deflection angles were observed in the two cases. More precisely, one should expect an inverse proportionality to J, i.e.:

$$\frac{\Delta\alpha_{0.30}}{\Delta\alpha_{0.18}} = \frac{J_{0.18}}{J_{0.30}} = \left(\frac{0.18}{0.30}\right)^4, \qquad [3]$$

where $\Delta\alpha = \alpha - \alpha_0$ is the deflection angle, and the subscript of each quantity denotes the relative wire diameter, in mm. The orientation of the wire was fixed to the vertical position; the vertical component of the torque was thus measured at four locations: outside the magnet (at the 20 G line), at the Magnet Inlet (MI), at the point of Maximal Deflection (MD) of the valve and at the Center of the Magnet (CM). The first three measurement locations were at 290, 42 and 25 cm from the center of the magnet, respectively.

Results and discussion

The experimental uncertainties are reported in Table 1 as the relative error in the determination of α, calculated with the standard deviation of the data taken at each location of the experiment, for the three independent repetitions of the latter. A good reproducibility of the method is demonstrated by these figures, with a relative error always better than 3.8%.

Table 1. Experimental uncertainties

D (mm)	20 G	MI	MD	CM
0.18	0.0104	0.0315	0.0036	0.0136
0.30	0.0132	0.0113	0.0383	0.0217

The difference between valve angles was measured, referring to the 20 G location, and plotted in Figure 2 for both set-ups. Black dots (empty circles) indicate the measurements with D=0.18 mm (D=0.30 mm).

As expected, the deflection angles for the thicker wire are smaller than in the case of D=0.18 mm, since for the latter the value of the polar moment of inertia (J) is lower, and from Eqs. 2a and 2b, at the same value of the torque, the deflection angle $\Delta\alpha = \alpha - \alpha_0$ is inversely proportional to J. The values of the measurements with D=0.30 mm, predicted from the data with D=0.18 mm, on the basis of Eq. 3 are also reported (crosses) in Figure 2. It can be seen that these values are within the experimental error, for all the three locations considered, referred to the 20 G data. This is the most natural choice, since at this low value of the magnetic field the valve is not sensing any torque, so that its angle can be assumed to be the initial angle (α_0) for the successive measurements.

The values of the torque measured with our set-up were always less than 2.65 x 10^{-5} N*m, value relative to the center of the magnet. We can define an equivalent force acting on the valve, by dividing the value of the torque by the diameter of the valve. The result is 9.81 x 10^{-4} N, corresponding to 0.1 g. Lower values were found further from the center of the magnet.

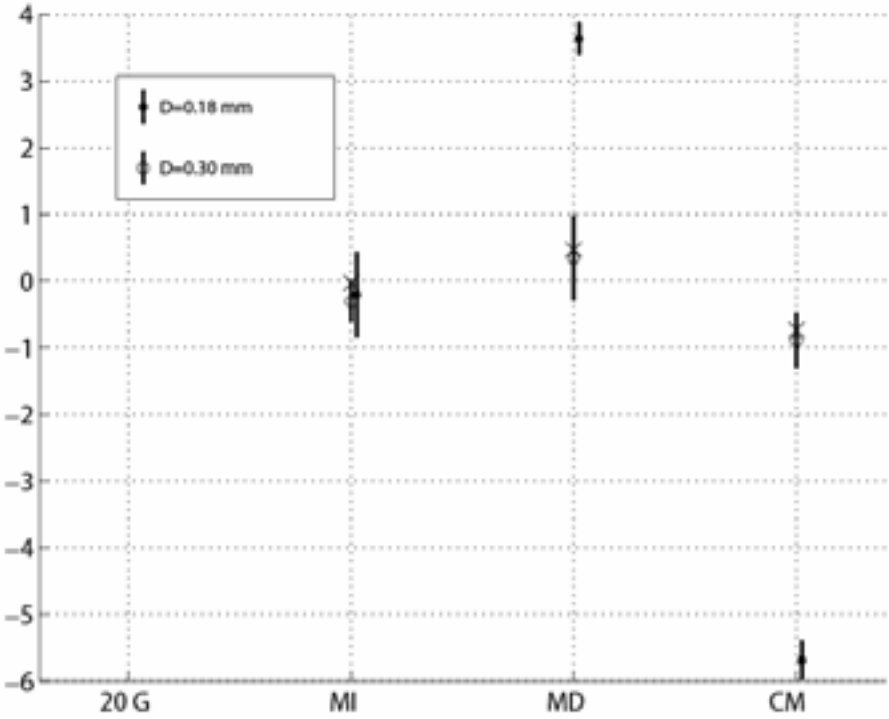

Figure 2. Deflection angles of the St. Jude valve for two set-ups, referred to the angles measured at the 20 G line

To the best of our knowledge no previous quantitative assessment has been made on the torque which is exerted by a static magnetic field on cardiac prosthetic valves. Quantitative assessment of the torque exerted by a static magnetic field has been so far performed on few non ferromagnetic implantable devices. In particular New and colleagues (2) measured the torque on surgical and dental devices in a 1.5 T MR system. The device was suspended by one end using a silk suture and a lead weight was attached to the free end. According to this method, the torque is given by:

$$N = (M + m)\, L\, g \sin \vartheta, \qquad [4]$$

where M is the mass of the added weight, m is the mass of the device, L is the distance from the pivot to the centre of the mass (device + weight), g is the gravitational acceleration (9.81 m/s^2), and ϑ is the angle of rotation. In New et al. (2) it was suggested to adjust the weight so as to obtain ϑ=45. It must be underlined that the determination of L is not immediate, since it depends on how the additional weight is applied to the device under test; in particular, L depends on the deflection angle ϑ. Then, it can be stated that the method proposed by New *et al*. (2) is subjected to potentially large errors, if L is not calculated rigorously. Moreover, only the component of the torque perpendicular to gravity can be measured, whereas with the method hereby proposed this limitation does not apply.

Conclusion

An accurate and easily implementable method for torque measurement of medical devices in MRI static fields has been proposed in the present work. The method has been validated with the measure of the torque with two different experimental conditions (torsion wire diameter), yielding results in agreement with the theory, in the limits of the experimental uncertainty.

References

1. Hu X, Norris DG. Advances in high-field magnetic resonance imaging. *Annu Rev Biomed Eng* 2004;6:157-84.
2. New PF, Rosen BR, Brady TJ, Buonanno FS, Kistler JP, Burt CT, Hinshaw WS, Newhouse JH, Pohost GM, Taveras JM. Potential hazards and artifacts of ferromagnetic and nonferromagnetic surgical and dental materials and devices in nuclear magnetic resonance imaging. *Radiology* 1983;147(1):139-48.

INTERACTION OF IMPLANTABLE MEDICAL DEVICES WITH MRI: EFFECT OF IMPLANT GEOMETRY ON CATHETER HEATING

Michele Triventi, Giovanni Calcagnini, Federica Censi, Pietro Bartolini, Vincenzo Barbaro
Dipartimento di Tecnologie e Salute, Istituto Superiore di Sanità, Rome, Italy

Introduction

Although Magnetic Resonance Imaging (MRI) is the imaging modality of choice in many cases, cardiac PaceMakers (PM) are considered a contraindication (1-3). MRI can cause many potential problems of interaction with PM. The static magnetic field can apply forces and torques to ferromagnetic materials (4,5); the time-varying gradient magnetic fields (at about 1 kHz) can mimic intrinsic cardiac activity and interfere with PM function (6); such gradients and/or the radiofrequency fields can induce voltages and currents in pacemaker catheter, resulting in cardiac stimulation (4); finally, the RF field can induce heating in pacemaker leads (6, 7). Aim of this study was to investigate the effect of implant geometry on catheter heating. We studied catheter heating induced by a continuous RF field in several implant and pacemaker configurations.

Materials and methods

Experiments were carried on at the Electromagnetics and Wireless Laboratory of the Center for Device and Radiological Health – Food and Drug Administration, Rockville, MD, USA. Figure 1 shows the experimental set-up for the temperature measurements. It consists of a RF coil, a signal generator HP8647A, 250-1000 MHz, a RF Power Amplifier EIN 3100, 250 kHz-105MHz, 50 dB, a Power Meter HP436A and a Fluoroptic Thermometer System Luxtron 3100 whose analog outputs were acquired by a laptop equipped with an acquisition card (NI, 250 Hz, 12 bit resolution).

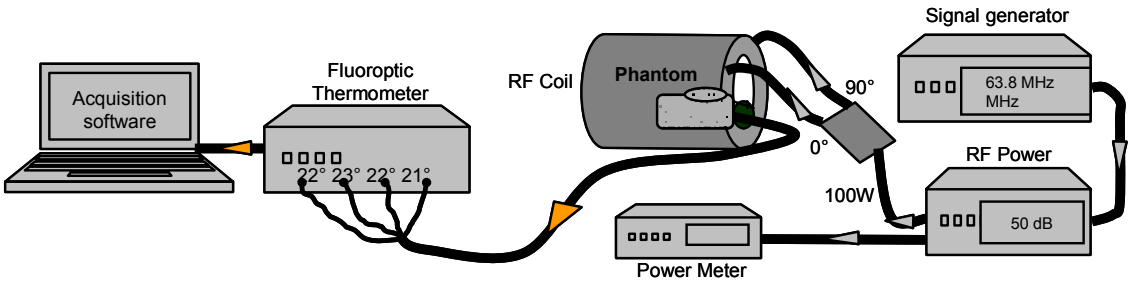

Figure 1. Experimental setup

The PM and the catheter, fixed to a plastic grid, were immersed in a human torso-shaped phantom, filled with gelled saline material that mimics the electrical properties of the human

tissue (conductivity of 0.59 siemens/m). The gel agent (hydroxy ethyl cellulose, HEC) was used to reduce the convection phenomenon (8, 9). The phantom used in the experiments is shown in Figure 2.

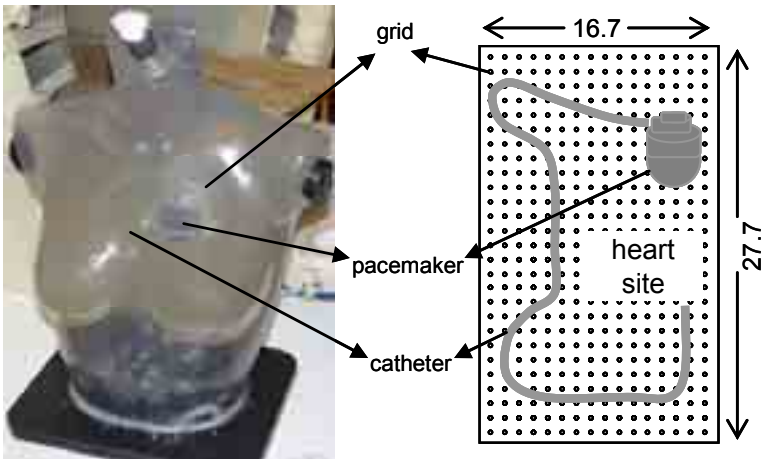

Figure 2. Phantom used for the experiments

Each PM was placed at the left side of the chest and the electrode approximately located at the heart site. The grid (16.7x27.7 cm) forms an array of square holes 1 cm apart, to fix the catheter, the PM and the temperature probes by plastic screws. Single and dual chamber PMs have been tested during unipolar and bipolar stimulation. In order to investigate the effect of loops on the heating phenomenon of the lead, for each pacemaker setting, we analyzed 4 implant configurations with the catheter forming none, 1 or 2 loops around the PM, as showed in Figure 3. For the one loop configuration, the catheter was looped counter-clockwise, as the main loop formed by the PM, the cathether and the saline between catheter tip and PM case.

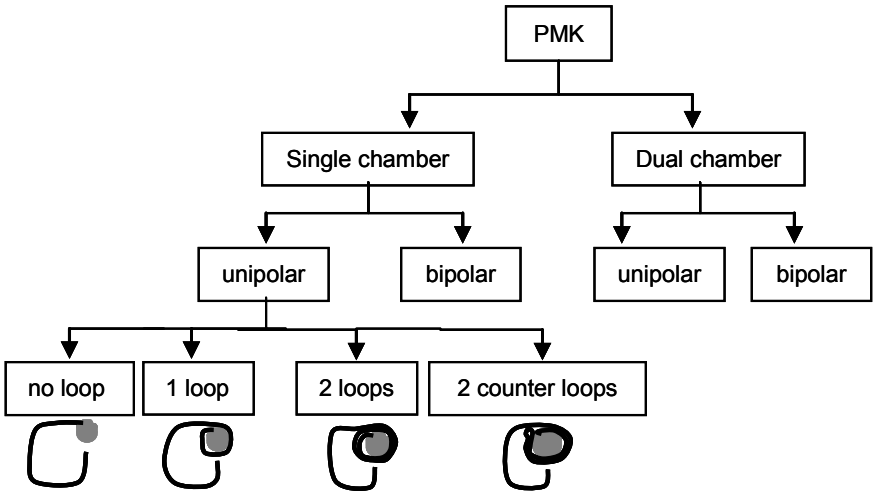

Figure 3. Pacemaker and implant configurations tested

Adding one more counter-clockwise loop led to the configuration we defined as 2 loops. The 2 counter loops configuration was obtained adding one clockwise loop to the 1 loop configuration.

In addition, in order to study the impact of implant area on temperature rise at the electrodes, a number of implant geometry with different areas have been tested.

In all the experiments the distance between the PM and the catheter tip was maintained constant (7.5 cm) and the catheters have the same length.

Fluoroptic probes were positioned on the PM case, on the catheter tip and in the gel. For bipolar catheters, the temperature of the ring electrode was measured by positioning the fluoroptic probes parallel and orthogonal to the ring. The protocol consisted of 2 steps: 1 minute baseline followed by the application of a continuos RF radiation at 64 MHz, 100 W, lasting 2 minutes (steady state).

Results

Figure 4 shows the temperature increases measured by the fluoroptic probes for the 4 implant configurations, at the end of the 2 minutes of RF exposure. We found that the catheter tip showed the maximum temperature increase in all configurations, while PM types and settings (single or dual chamber, unipolar or bipolar stimulation) did not influence the temperature increase.

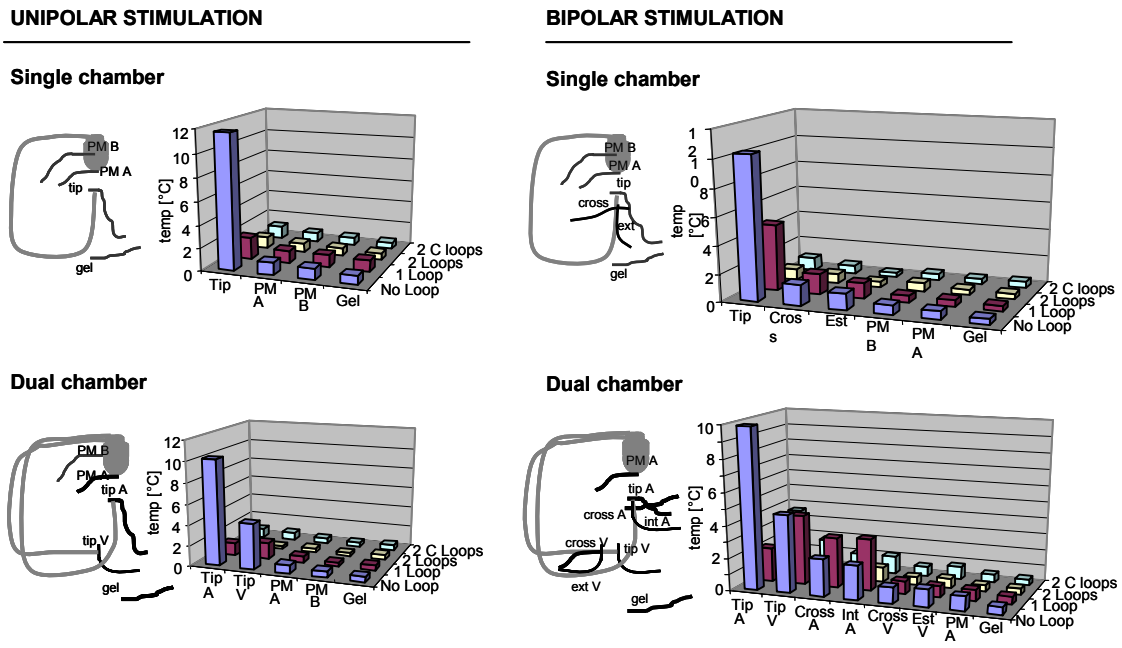

Figure 4. Temperature increases (°C) for the 4 implant configurations measured by the fluoroptic probes as indicated at the left side of each graph. (2 C loops= 2 counter loops)

Table 1 summarises the temperature increases at the tip obtained for all implants and PM configurations: the bigger the number of loops, the smaller the temperature increase at the

catheter tip. Figure 5 shows the temperature increase at the catheter tip obtained for the implant geometry reported along the x axis. As expected the smaller the implant area, the lower the temperature rise.

Table 1. Tip temperature increase (°C, accuracy ±0.1 °C)

Geometric configuration	Single chamber unipolar	Single chamber bipolar	Dual chamber unipolar	Dual chamber bipolar
No Loop	11.7	10.3	10.2	9.9
1 Loop	1.9	4.8	1.2	2.1
2 Loops	1	0.8	0.4	0.5
2 Counter Loops	1.1	0.9	0.9	0.6

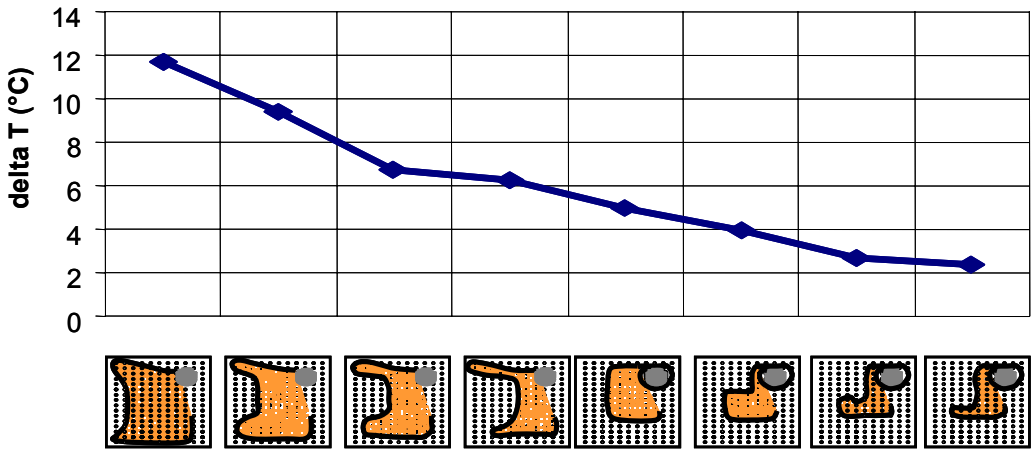

Figure 5. Temperature increase at the catheter tip obtained for the implant geometry reported along the x axis

Discussion and conclusion

MRI-induced heating in metallic implants is mainly due to the energy deposition into the conductive parts of the implant, which is redistributed into the surrounding human tissue. Heating occurs at the conductive surfaces of the implant: the smaller the surface the higher the current density. Given the presence of insulation along the implant, maximum induced heating is generally found at the catheter electrodes (i.e. tip and ring). We found the maximum increase at the catheter tip in all implant and PM configurations, regardless PM type and settings. In addition, the loops seemed not to enhance the heating phenomenon. Basically, the bigger the number of loops, the smaller the area of the coil formed by the catheter, PM and the saline, the smaller the flux of the magnetic component (B field) of the RF field concatenated with the coil.

Since catheter heating seems to be especially problematic when implant forms coils of not negligible areas, future investigations should include evaluations of implants with the PM at the right site of trunk, with catheters of different lengths, and with and without a connected PM, to get a better impression about the expected heating. The presence of extended wires can indeed act as dipole antennas picking up the electrical component (E field) of the RF field (10). Parameters such as lead impedance and thermal conductivity should also be taken into account, strongly influencing the heating phenomenon.

Acknowledgement

Authors would like to thank Howard Bassen and Wolfgang Kainz from the Center for Device and Radiological Health, Food and Drug Administration, Rockville, MD, USA, for the use of the MRI simulator, and Guido Gaggini from the Sorin Biomedica for the catheters and PM samples used in this study.

References

1. Gangarosa RE, Minnis JE, Nobbe J, Praschan D, Genberg RW. Operational safety issues in MRI. *Magn Reson Imaging* 1987;5(4):287-92.
2. U.S Food and Drug Administration Magnetic resonance diagnostic device; panel recommendation and report on petitions for MR reclassification. *Fed Reg* 1988; 53:7575-79.
3. Bartolini P. Installation of magnetic resonance equipment: technical requirements, site suitability criteria and safety control. Aspects related to the safety of the patients and the population. *Ann Ist Super Sanità* 1994;30(1):95-108.
4. Luechinger R, Duru F, Scheidegger MB, Boesiger P, Candinas R. Force and torque effects of a 1.5-Tesla MRI scanner on cardiac pacemakers and ICDs *Pacing Clin Electrophysiol* 2001;24(2):199-205.
5. Bartolini P. Interactions of electromagnetic fields produced by magnetic resonance with prostheses and ferromagnetic materials. *Ann Ist Super Sanità* 1994;30(1):51-70.
6. Martin ET, Coman JA, Shellock FG, Pulling CC, Fair R, Jenkins K. Magnetic resonance imaging and cardiac pacemaker safety at 1.5-Tesla. *J Am Coll Cardiol* 2004;Apr 7;43(7):1315-24.
7. Sommer T, Vahlhaus C, Lauck G, von Smekal A, Reinke M, Hofer U, Block W, Traber F, Schneider C, Gieseke J, Jung W, Schild H. MR imaging and cardiac pacemakers: in-vitro evaluation and in-vivo studies in 51 patients at 0.5 T. *Radiology* 2000;215(3):869-79.
8. Ruggera PS, Witters DM, von Maltzahn G, Bassen HI. *In vitro* assessment of tissue heating near metallic medical implants by exposure to pulsed radio frequency diathermy. *Phys Med Biol* 2003;Sep 7;48(17):2919-28.
9. Park, SM, Nyenhuis JA, Smith CD, Lim EJ, Foster KS, Baker KB, Hrdlicka G, Rezai AR, Ruggieri P, Sharan A, Shellock FG, Stypulkowski PH, Tkach J. Gelled versus nongelled phantom material for measurement of MRI-induced temperature increases with bioimplants. *IEEE Trans Mag* 2003;39(5):3367-71.
10. Hofman MB, de Cock CC, van der Linden JC, van Rossum AC, Visser FC, Sprenger M, Westerhof N. Transesophageal cardiac pacing during magnetic resonance imaging: feasibility and safety considerations. *Magn Reson Med* 1996;35(3):413-22.

CHARACTERIZATION OF WIRELESS COMMUNICATIONS IN CLINICAL ENVIRONMENTS

Diego Salamon (a), Micaela Liberti (a),Guglielmo D'Inzeo (a), Stefano De Luca (c), Mauro Grigioni (b)
(a) Dipartimento di Ingegneria Elettronica,Università degli Studi "La Sapienza", Roma, Italy
(b) Dipartimento di Tecnologie e Salute, Istituto Superiore di Sanità, Rome, Italy
(c) Dipartimento di Scienze Matematiche Fisiche e Naturali, Università degli Studi "Tor Vergata", Roma, Italy

Introduction

Wireless communications are carrying out a noticeable part in the health-care sector innovation. But this impulse must be guaranteed by an analysis of risks these technologies can create in environments where it is necessary to assure high security standards. A set of rules gives guidelines which must be respected in order to assure such security standards. By taking into consideration utilization in clinical environments of the same wireless technologies used in IT sector, this work intends both to make an electromagnetic compatibility analysis directed to hospital environment and to give informations to use these technologies in such places.

Health care informatics

The health care industry is currently experiencing a fundamental change (1). Health care organizations are reorganizing their process to reduce cost, be more competitive, and provide better and more personalized customer care. This new business strategy requires health care organizations to implement new technologies such as Internet applications, enterprise systems, and mobile technologies in order to achieve their desired business changes.

Mobile communications offer two distinct advantage to the health care world. First, mobile technologies are important for telemedicine success. While certain media that are already in place, such as television and telephones, offer avenues for telemedicine deployment, mobile communications offers another avenue that can also be used in conjunction with telemedicine. Personal Digital Assistant (PDA) can be used by physicians to send instant messages to patient reminding them when they need to take their medication Second, mobile devices and wireless Internet allow physicians access information anywhere at anytime. This is an important benefit for providers, because real-time information is essential for physicians and hospitals and mobile devices provide that capability. Wireless Technologies are the best application for mobile device and their use in clinical environment are best innovation for the future digital hospital.

Wireless technologies

Wireless LAN is a flexible data-communications system, implemented as an extension to or as an alternative for wired LAN. Using radio frequency technology, WLAN transmit and receive data over the air, minimizing the need for wired connections. Thus WLANs combine data connectivity with user mobility. They are becoming very popular in a number of vertical

markets, including healthcare, retail, manufacturing, warehousing. These industries have profited from the productivity gains of using hand-held (2) terminals and notebook computers to transmit real time information to centralized hosts for processing.

Because of their strength against interference, the principal technologies are based on the Spread Spectrum technique. Such technique is based, in transmission, on the information dispersion on a wider frequency spectrum (spreading). In reception, the information is recompacted (despreading), and one obtain a just by receiver interpretable signal. The technique Direct Sequence Spread Spectrum technique (DSSS) foresees the transmission of the signal multiplied by a note binary sequence (chip sequence) at higher speed, making it similar to low power noise, but to wide band one. The receiver, who knows the chip sequence, can recover the information contained in the transmitted signal. As longer it is the chip duration, as greater it is the probability that original data can be recovered (and greater it is the used band). To a not synchronized receiver, the DSSS appears like a low power noise at wide band, therefore it is ignored by many narrowband receivers. Frequency Hopping Spread Spectrum (FHSS) technique, instead, transmits the signal in temporal slot associated to differently frequencies according to a jump sequence (hopping sequence) note to receiver. To a not synchronized receiver, the FHSS appears to be noise of impulsive type. These techniques allow to get a low spectral power density signal and to minimize the possibility of interfering with other signals, present in the same area. The natural candidates to the possibility of installations in clinical environments are: the WiFi transmission (IEEE802.11b) and the Bluetooth one (IEEE802.15).

Electromagnetic compatibility

The electromagnetic waves' harmful effects can belong to three typologies (3): thermal effects, cellular ones and on medical devices' ones. For the interest applications, the wireless communications to 2.4 GHz give birth to neither substantial modifications to the cellular level nor temperature alterations also in case of transmission in proximity of the human body; this thing can be supported for the extremely small value of the generated electromagnetic field and for the generally used frequency for these transmissions (4). The same thing cannot be told for the interference towards medical devices. Six years ago FDA found cases of medical devices' bad functioning owed to electromagnetic interference; today a standard of immunity has not been emanated but FDA (5) proposes as guideline the respect of 7 V/ m around at 900 MHz. In Europe the considered normative is the IEC60601-1-2 that imposes the respect of the 3 V/m around at 1000MHz and of the 10 V/m around at 2.4GHz.

Conclusion

The value of electric field radiated from a source is directly dependent on his power. Various technologies are differently compliant with the normative. The study shows that Bluetooth are the best choice for medical environments because medical device have not interference for the electromagnetic field generated by Bluetooth transmitter. Other technologies are compliant only if the distance from the medical device is longer than 2.5m.

Normative aspect of the problem is very important. Different states adopted different laws, so the panorama is very differentiate by this point of view.

One of the principal advantages of wireless communications is the possibility of access to information anytime anywhere. The pervasive computing is the next hospital medicine frontier,

where portable devices like handheld will be the future clinical tools; for example, "George Pompidou" Hospital in Southern France has become famous as the most technological hospital in Europe: the medical staff agrees to the patients clinical folders through notebook set in cart.

References

1. Siau K. Health care informatics. *IEEE Trans Inf Technol Biomed* 2000;7(1):1-7.
2. Adatia F, Bedard PL. Palm Reading: HandHeld software for physicians. *CMAJ* 2003;168:27-34.
3. Witters D, Portnay S, Casamento J, Ruggera P, Bausser H. Medical Device EMI:FDA analysis of incident Reports. *IEEE International EMC Symposium*, Montreal, 13-17 August 2001. p.1289.
4. Siau K. Health care informatics. *IEEE Transaction on Information Technoogies in Biomedicine* 2003;7(1):1-7..
5. Adatia F, Bedard PL. "Palm reading": 2. *Handheld software for physicians. Canadian Medical Association Journal* 2003;168(6):727:34.

VIBROCARDIOGRAPHY FOR NON CONTACT MONITORING OF THE HEART BEAT BY LASER VIBROMETRY

Lorenzo Scalise (a), Umberto Morbiducci (a, b), Mirko De Melis (a), Enrico Primo Tomasini (a), Mauro Grigioni (b)
(a) Dipartimento di Meccanica, Università Politecnica delle Marche, Ancona, Italy
(b) Dipartimento di Tecnologie e Salute, Istituto Superiore di Sanità, Rome, Italy

Introduction

The monitoring of heart rate is a typical task in clinical environment for a great variety of patient's condition (1). The possibility to obtain this information without any contact with the patient represented a future tool in many fields also outside of the clinics. In fact generally this task cannot be accomplished when patient's condition determine impairment of their health if contact with skin or any other surface has to be avoided, (e.g. severely burnt subject), or when the type of functional situation e.g. such as the case of people with (e.g. magnetic resonance imaging analysis) or people within confined environment (such as hyperbaric chamber) do not allow to put any sensor or electrodes within the examination environment. In all these situations an alternative method to the typical one must be provided to monitor heart rate activity at least from the point of view of the beat rate, with respect to heart rate obtained by normally using continuous electrocardiographic records, which the QRS complex detected. In the following we propose a new technique capable to obtain no contact monitoring of the heart rate using an optical method. Laser vibrometry technique (2) is applied to monitoring heart rate by means of the measurement of the proprieties of the motion of the external surface of human body (chest wall). Laser techniques for vibration measurement, due to their non-contact nature, present an alternative investigational tool with respect to the traditional contact methods (ECG, EMG, etc.) to be tested in clinic fields. An advantage of this approach is that it provides a non-contact method to measure HR, and to assess the vital sign monitoring. The purpose of this study is to develop a non-contact method to measure the heart rate, and to assess the vital sign monitoring.

Materials and methods

Short-term recordings (5 minutes) (1) were carried out on 5 healthy human subjects at resting. The ECG and the velocity of vibration of the chest wall, i.e., the VCG (VibrioCardioGram) were simultaneously recorded. To do this, a laser head for Doppler vibrometry measurement bench test was built up. Figure 1 shows the laser head positioning on the torax on a subject and the measurement point on the chest wall. After the laying of the laser beam, ECG and the vibratory signal from the chest wall were contemporary recorded and retrieved afterwards to measure the consecutive RR and vibrocardiographic (VV) intervals (Figure 2). Under the basic assumption that the mechanical event follows the electic stimulus, sequences of RR and of the corresponding (i. e., the vibratory peak immediately following the R peak in ECG) VV intervals were obtained, and on them tachograms were built by using a proper

own code for peak detection, by means of MATLAB (The MathWorks, USA) software. Atrial or ventricular ectopic beats were deleted (as in the current practice) (3).

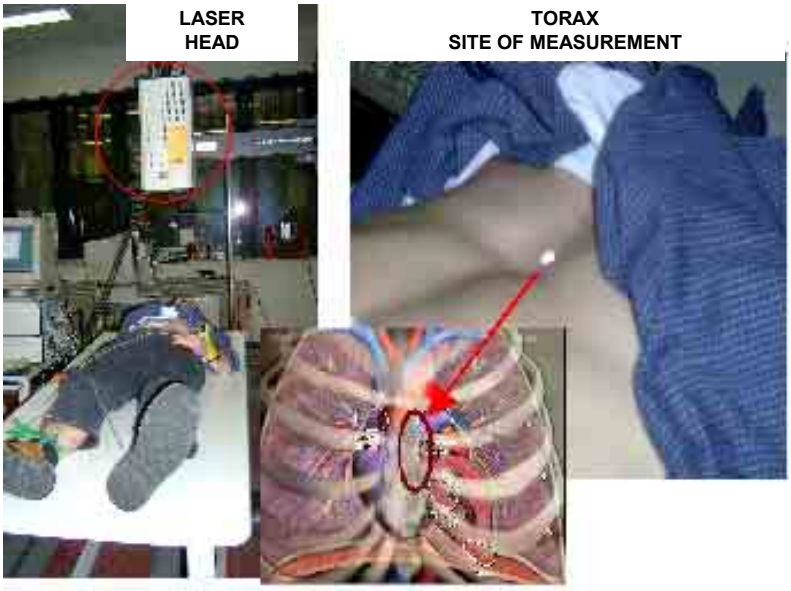

Figure 1. Laser head positioning and measurement site for VCG signal recording

Power spectral analysis of heart rate variability is a commonly used method in the measurement of sympathovagal interaction on sinus node (4). However, only an estimate of the true power spectral density of the tachograms can be obtained, independent of the mathematical methods (properly) employed. In the present study a non parametric method, with the simple, high processing speed, Fast Fourier Transform algorithm, was applied for the calculation of the power spectral density. In order to stress the limits of the vibratory signals in representing the sympatho-vagal activity as the ECG, the power spectral analysis was carried out. VCG an ECG tachograms were resampled at 2Hz, and a Hanning window was applied in the time domain. After the square of the fast Fourier transform was computed, the power spectrum was obtained after multiplying each frequency component by 2.66, to correct for Hanning window (5). Spectral entropy was estimated (6). From the recordings in patients undergoing measurements, we evaluated the physiologic relationship of the ECG to the vibratory waves.

Results

Figure 2 shows a typical beat VCG simultaneously with the recording of ECG. The VCG clearly includes a low-frequency wave during Atrial Systole (AS), a larger wave during Ventricular Systole (VS), and a wave in early diastole, at the time of early Ventricular Filling (VF). Resting VCGs, although there are minor differences among subjects, show common features to all, in particular the shape of the VS complex.

Figure 3 shows 10 s recordings relative to a subject. All the components of the vibratory signal are present for all the monitored subjects. Figure 3 also shows peak detection, realised by a proper code, preliminary step for data analysis (as mentioned above).

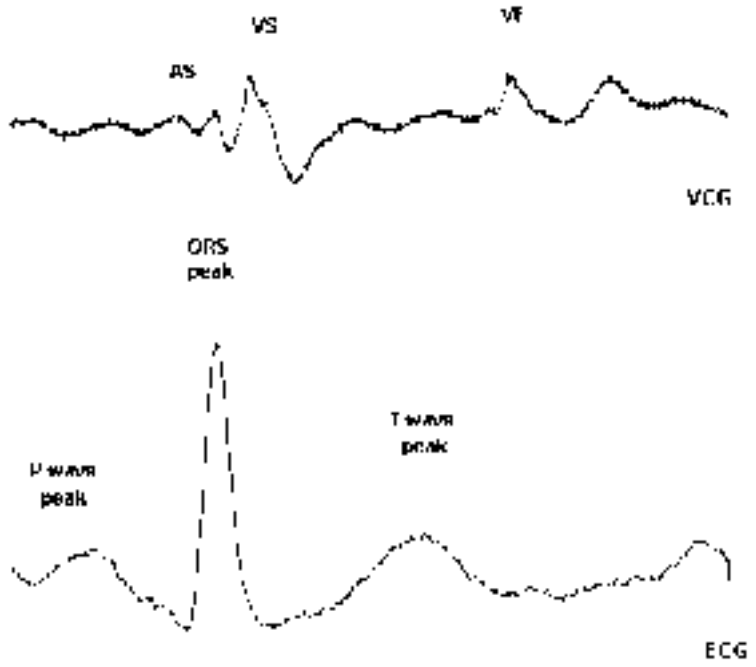

Figure 2. Typical human, one beat, VCG, together with the simultaneously recorded ECG. Individual components of the VCG are labelled: low-frequency wave during AS; larger wave during VS; wave in early diastole, at the time of early VF

On the built up tachograms the Power Spectral Density (PSD) was calculated: for all the monitored subjects the Chi-square test gave no statistical significative difference ($p<1$) between the PSD from RR and VV.

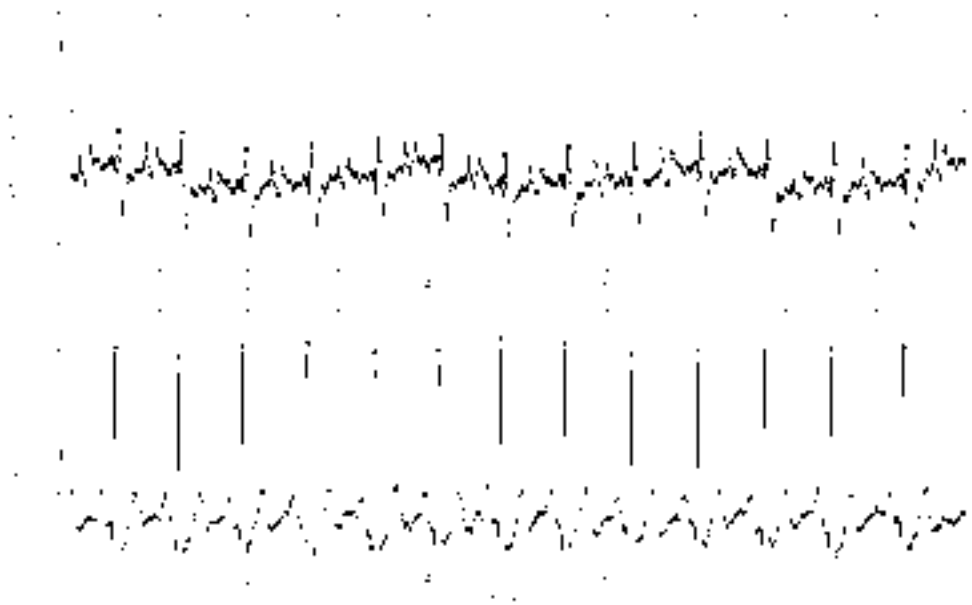

Figure 3. Unaveraged continuous recording of the VCG and ECG (the shape of the VS complex can be noticed. Peak detection is also shown, preliminary step for data analysis)

Table 1 summarizes the results of the spectral analysis on PSDs from VCG and ECG derived sequences: percentage differences in total spectral power, Shannon channel entropy (6), and LF/HF spectral powers ratio were calculated for all the monitored subjects. Percentage differences less than 5.5% were obtained for LF/HF spectral powers ratio, and differences less than 2.1% and 1.2% were obtained for total spectral powers and LF/HF spectral power ratios, respectively.

Table 1. Percentage differences in total spectral power, Shannon channel entropy, and LF/HF spectral powers ratio calculated for all the monitored subjects

Subject number	LF/HF spectral power ratio	Total spectral power	Spectral entropy
1	-0.481%	-0.248%	-0.017%
2	5.515%	2.148%	1.156%
3	0.194%	0.088%	-1.024%
4	4.239%	-0.530%	0.900%
5	-4.441%	0.470%	0.096%

The results resumed in table I clearly demonstrate the coincidence between the selected events, i.e. the relationship between the R peak on the ECG, and the V peak on the vibratory signal from the thorax.

Discussion

The motion of the surface of the external surface of the human body can be related to the mechanical activity of the heart and of the lungs, and is mediated by the tissue motion originated by the quality of the flow and pressure at the heart or at the site of interest together with the compliance of the cardiovascular tree (impedance). In a general sense also the information on the cardiovascular tree condition (e.g. hypertension or compliance affections) could be obtained together with the quality of the beat to beat variability if sufficient long recordings could be made. Moreover also several functional information could be achieved from the optical signal we carry out from the vibrometer thank to the actual algorithm used to investigate the simpato-vagal control from the neural structure of a patient, that is a mathematical technique capable to obtain the breathing frequency, the impairment of one of nervous system control (simpathethic or vagal nerve) or the incorrect balance among them. In all these cases relevant patient's condition related to the pathology is obtained. Thus Heart rate variability (HRV) can be carried out as one of the most promising markers for the quantitative assessment of autonomic activity of nervous system on heart and its significant consequences on cardiovascular efficiency and post-infarction mortality related to lethal arrhythmias and other cardiovascular pathologies (1). Time variations in heart rate are normally carried out using continuous electrocardiographic records, from which each QRS complex is detected. HRV analysis, showed to be a very powerful tool in the assessment of cardiovascular disease (1) is an important marker for the quantitative assessment of autonomic activity of nervous system on heart and its significant consequences on cardiovascular efficiency and mortality related to lethal arrhythmias (7) and other cardiovascular pathologies (1). A review of the alternative methods for assessment of cardiac rate suggests the interest on displacement cardiography and presents limits: phono-cardiology as well as the use of stethoscope can be considered among

this class of instruments even if limited by the high frequency sensitivity related to audible range of such instruments; ballisto-cardiography (8), widely used in the past, has not gained the status of a valid clinical diagnostic tool; kineto-cardiography (9), that detects the pressure waves generated by heart wall displacement by means of a pressure sensor placed on the chest, has not been used widely, due to its low sensitivity; seismocardiography (10) has been presented as a novel non-invasive technique, notwithstanding it is a contact procedure, for the recording of cardiac vibratory activity. The HR measured using the proposed method agreed, with high coincidence, with the rate derived from an ECG record. This method appears promising as a non-contact method to monitor the cardiac activity of patients under specific conditions, e.g., in incubated newborns, and in severely burnt subjects.

References

1. Task Force of the European Society of Cardiology and the North American Society of Pacing and Electrophysiology. Heart rate variability: standards of measurement, physiological interpretation, and clinical use, *European Heart Journal* 1996;17:354-381.
2. Castellini P, Revel GM, Tomasini EP. Laser Doppler Vibrometry. *The Sound and Vibration* 2001.1;68(2):201-7.
3. Kuo CD, Chen GY, Wang YY, Hung MJ, Yang JL. Characterization and quantification of the return map of RR intervals by Pearson coefficient in patients with acute myocardial infarction. *Auton Neurosci* 2003;105(2):145-52.
4. Akselrod S, *et al*. Power spectrum analysis of heart rate fluctuation: A quantitative probe of beat to beat cardiovascular control. *Science* 1981; 213:220-2.
5. DeBoer RW, Karemaker JM, Strackee J. Comparing spectra of a series of point events particularly for heart rate variability data. *IEEE Trans Biomed Eng* 1984; 31(4):384-7.
6. Acharya R, Kumar A, Bhat PS, Lim CM, Iyengar SS, Kannathal N, Krishnan SM. Classification of cardiac abnormalities using heart rate signals. *Med Biol Eng Comput* 2004;42(3):288-93.
7. Swartz PJ, Priori SG. Sympathetic nervous system and cardiac arrhythmias. In: Zipes DP, Jalife J (Ed.). From cell to bedside. Philadelphia: W.B. Sauders; 1990. p. 330-43.
8. Lindqvist A, Pihlajamaki K, Jalonen J, Laaksonen V, Alihanka J. Static-charge-sensitive bed ballistocardiography in cardiovascular monitoring. *Clin Physiol* 1996;16(1):23-30.
9. Rodriguez G, Beghin L, Michaud L, Moreno LA, Turck D, Gottrand F. Comparison of the TriTrac-R3D accelerometer and a self-report activity diary with heart-rate monitoring for the assessment of energy expenditure in children. *Br J Nutr* 2002;87(6):623-31.
10. Salerno DM, Zanetti JM, Green LA, Mooney MR, Madison JD, Van Tassel RA. Seismocardiographic changes associated with obstruction of coronary blood flow during balloon angioplasty. *Am J Cardiol* 1991 15;68(2):201-7.

VORTEX IDENTIFICATION DOWNSTREAM OF PROSTHETIC HEART VALVES

Umberto Morbiducci, Giuseppe D'Avenio, David Di Meo, Costantino Del Gaudio, Mauro Grigioni
Dipartimento di Tecnologie e Salute, Istituto Superiore di Sanità, Rome, Italy

Introduction

The evaluation of the fluid dynamical behaviour of prosthetic heart valves (PHV) is of fundamental importance to discriminate on the correct functionality of these devices, especially in those quantities which can be related to blood damage: as these quantities are given by statistics of higher order than the simple velocity average, care must be taken in the accuracy of the measure. The fluid dynamics of PHVs is particularly complex, with high spatial gradients and Reynolds shear stresses, especially as far as mechanical heart valves are concerned. The fine-scale characterization of such flows calls for very accurate experimental techniques, in terms of both spatial and temporal resolution. In particular, velocity profiles and Reynolds stresses downstream of heart valve prostheses are vital parameters in the study of hemolysis and thrombus formation associated with these valves. PIV is routinely used by flow researchers and medical device manufacturers to provide two-dimensional mapping that can identify disturbed flow patterns. PIV is basically a multipoint measurement technique that furnishes full-field measurement of instantaneous velocity vectors in a flow field, thus allowing us to map the entire velocity flow field over the aortic root. As such, it provides a powerful tool for studying the safety and efficacy of flow-related devices. An advantageous feature of PIV technique, is the fact that it does not perturb the flow to be investigated. This essential property allows much more rapid results, and has gained sufficient temporal and spatial resolution to estimate velocity fields, depending on the degree of instability in the flow, provided that sufficient images are available to estimate the mean flow (1). The purpose of this study is to determine the dynamics of the vortex in the Valsalva sinus during the cardiac cycle, after the map the flow fields downstream of a mechanical prosthetic heart valve in the aortic root region was performed *in vitro*, under pulsatile flow conditions, with PIV technique. The presence of the three sinuses of Valsalva in the aortic root, makes the region immediately downstream of the aortic valve non-symmetric, with remarkable consequences in the flow domain and related significant consequences both functional, haemodynamical and rheological. It is opinion of the authors that the study of vortex dynamics in the Valsalva sinus has to be massively addressed, playing it a significant role both in the opening and closing motion of valve's leaflets.

Materials and methods

A pulsatile study has been performed in a mock circulatory loop consisted of the Sheffield pulse duplicator properly modified with a glass blown model of epitrochoidal-shaped aortic root, and an optically clear valve housing segment to allow unobstructed laser measurements (2). The command waveform for the pulse duplicator has been set to attain mean aortic pressure: 100 mmHg, 70 beats/min and a 35% systole/cycle ratio, for cardiac output of 4 L/min. Within

the mock circulatory loop a transparent Newtonian test fluid consisting of a water – glycerine solution about 33%, with a 3.7 cSt (blood analogue) kinematic viscosity, was used.

The macroscopic description of the flow field is given through the characteristic adimensional quantities Reynolds (5685) and Womersley (10.97) numbers, calculated considering the average velocity at peak systole in the flow meter section.

Flow measurements were performed, at a mid section of the aortic root, downstream of a CarboMedics bileaflet mechanical heart valve (19mm tissue annulus diameter), implementing a two-dimensional PIV system. A light sheet was created by a dual Q-Switched Nd:Yag laser source. Silicon carbide powder was used to have flow tracers that the fluid was seeded with, allowing the light emitted by the laser to be scattered by those fluorescence particles.

A PIV commercial software (Insight 5, TSI Inc., USA) was used to process and analyse the acquired images. The solution used as test fluid guaranteed optical refraction index matching, which improves the optical image quality further. In addition to the scan of the observation plane, a scan in time was performed, with particular attention to the time interval around the systolic peak.

The calculation of instantaneous velocity vector mappings in the region of the aortic root was done by means of a cross-correlation algorithm for each interrogation area. In the present investigation, 1000 PIV measurements have been ensamble averaged to obtain true-mean flow field and a stationary turbulence first order statistics.

A vortex detection algorithm is applied, which allows determining the instantaneous position and the relative dynamics of the recognized events, e.g., the tidal evolution of vortical structures inside the sinuses of Valsalva. Vortex evolution was tracked by means of the λ_2 method by Jeong and Hussain (3). The mean rate-of-displacement tensor d_{ij} is defined by:

$$d_{ij} = \frac{\partial u_i}{\partial x_j}$$

where u_i are the mean velocity components and x_j are the space variables in a Cartesian coordinate system. The mean rate-of-displacement tensor can be decomposed into the summation of the symmetrical rate-of-strain tensor s_{ij}:

$$s_{ij} = \frac{1}{2}\left(\frac{\partial u_i}{\partial x_j} + \frac{\partial u_j}{\partial x_i}\right)$$

and the skew-symmetrical rate-of-rotation tensor r_{ij}:

$$r_{ij} = \frac{1}{2}\left(\frac{\partial u_i}{\partial x_j} - \frac{\partial u_j}{\partial x_i}\right)$$

Jeong and Hussain (3) evaluate locally the flow rotation on the basis of the second invariant of the velocity gradient tensor. They define a vortex a vortex core as a connected region with two negative eigenvalues of $s_{ij}s_{kj}+r_{ij}r_{kj}$, i.e., the steady, symmetric part of the gradient of the Navier Stokes equation (for further details, see Jeong and Hussain). Due to its symmetry, $s_{ij}s_{kj}+r_{ij}r_{kj}$ has real eigenvalues only. As a consequence, the definition by Jeong and Hussain (3) is equivalent to say that the second largest eigenvalue of $s_{ij}s_{kj}+r_{ij}r_{kj}$, named λ_2, is the parameter in identifying a vortex: high negative values of λ_2 identify vortical flow regions where the rotation rate dominates the strain rate in the mean flow field.

Results

Figure 1 show PIV vector velocity fields at three phases of the cardiac cycle (i.e., acceleration, peak systole, deceleration), chosen to show the instantaneous evolution of the structure of the flow field during systole. In particular, the progression of the vortex within the sinus can be appreciated: it is possible to follow both the growth and the spatial displacement of this vortex during the temporal evolution of the systolic period (typical vortical structure released downstream of the leaflets and in the sinus region). The presence of a ricirculating region, pointed out in the vector maps, is clearly evident within the sinus of Valsalva, in accordance with the inversion of the velocity values in this region (4).

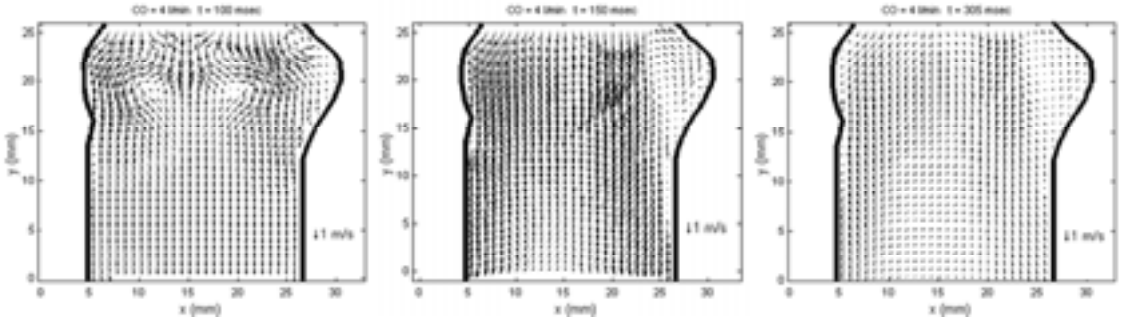

Figure 1. Velocity vector maps at three different instants (acceleration, peak, and deceleration) during systole

Figure 2 shows the vortex evolution during systole tracked by means of the λ_2 maps by Jeong and Hussain (3). The spatial progression of shedding vortices from the leaflets can be appreciated; in particular, the choice of this plane of investigation documented the history of a large vortex in the sinus that has the maximum size on this projection.

The herein followed approach allows to emphasize the typical vortical structure released downstream of the leaflets and in the sinus region. Figure 1 and Figure 2 show a right jet from the open valve with an axial velocity peak towards the longitudinal axis of the valve conduit, due to an increased extension of the recirculating area in the sinus; moreover, this jet is associated to the highest values of the axial velocity in the sections immediately downstream of the valve. This is due to the boundary action exherted by the vortex developed in the sinus of Valsalva, which makes the right jet more co-linear to the valve conduit. The effect of the deceleration increases the dimensions of the sinus fluid recirculation and squeezes the fluid toward the duct centre. During the deceleration phase, there is a reduction of the values of both the two velocity components. Considerations on vortex dynamics in the aortic root during systole cannot overlook that a strong reduction of vortices, in terms of magnitude and size, in the sided regions of the aortic root downstream of the prosthetic device, seems to be a not favourable condition for feeding the coronary arteries (5). In the case of the natural aortic valve, the vortex flow in the sinus of Valsalva pushes the leaflet to close, and the valve starts the closing motion earlier than the prosthetic valve as the forward flow decelerates On the contrary, conventional bileaflet prosthetic mechanical heart valves close passively with backflow, and the valve has problems associated with closure, such as backflow, water hammer effect, and fracture of the leaflet (6).

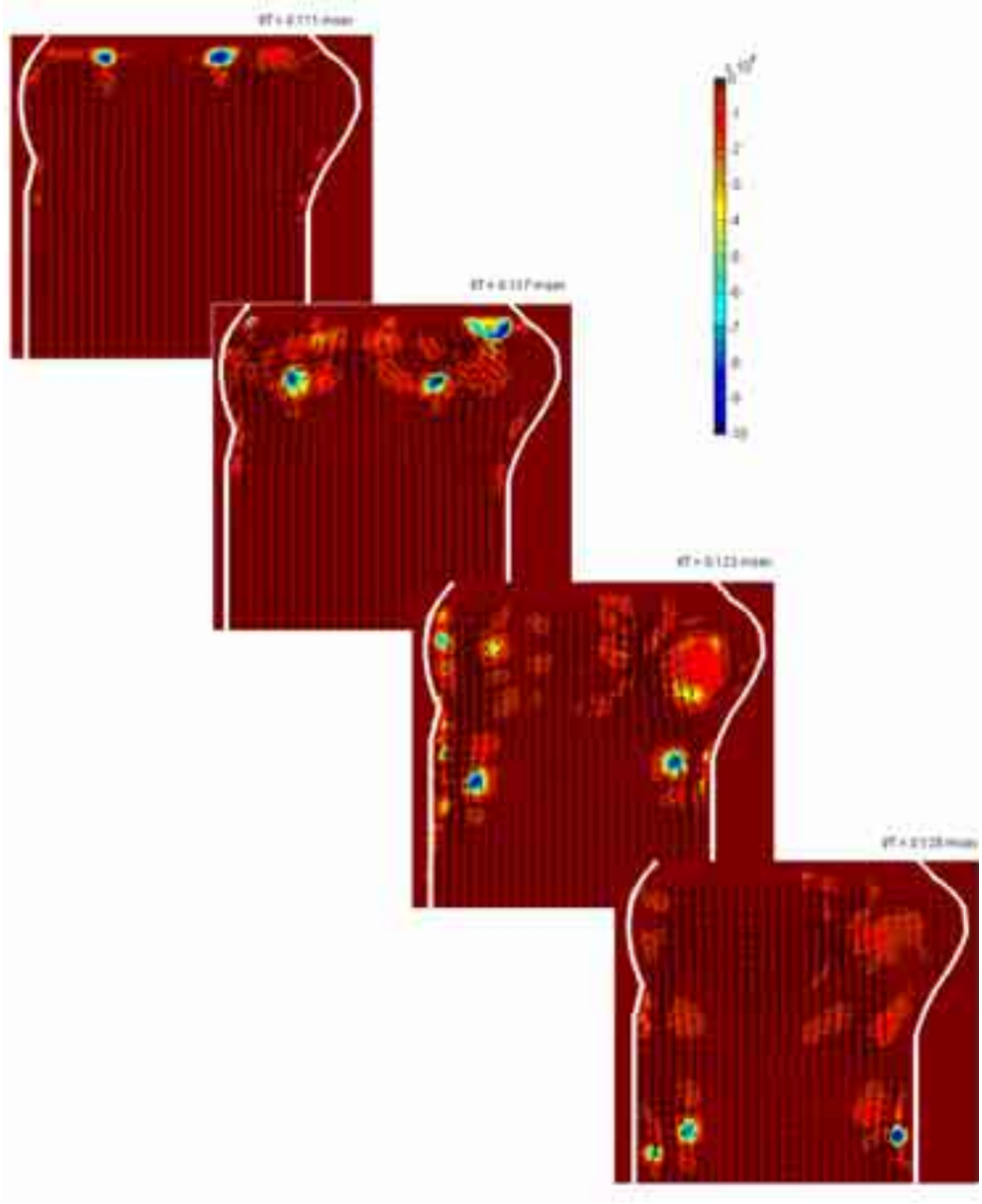

Figure 2. Vortex evolution during systole tracked by means of the λ_2 maps

Discussion

Recently, FDA advocated also the use of PIV technique to investigate implantable devices related fluid dynamics: "This measurement technique can identify zones of flow stagnation or high shear stress, either of which can lead to adverse effects. Flow stagnation can cause thrombosis, embolism, and stroke. Excessive shear causes hemolysis, that is, ruptured red blood cells" (7). In the past, PIV technique was applied to study artificial valves related fluid

dynamics. Steady and pulsating flow, rather than regurgitant and forward flow were investigated both for mechanical and biological prostheses. A summary of PIV studies on valvular prostheses indexed in the Medline can be found in (8). Full-field measurement of instantaneous velocities in the flow field of mechanical artificial heart valves is vital as the flow is unsteady and turbulent. PIV provides us the ability to do this as compared to other point measurement techniques, like LDA (9,10), where the velocity is measured at a single point in space over time. However, the experience the Authors gained in the setting up of environments conducive for both LDA and PIV studies of artificial heart valves suggests that the PIV technique has sufficient temporal and spatial resolution to estimate velocity fields depending on the degree of instability in the flow, provided the sufficient images are needed to duplicate mean flow (1). The need to be closer to the anatomical aortic root shape relies on the fact that the fluid dynamics in this region is strictly correlated to the degree of perfusion. Some authors (11) showed that the presence of the sinuses of Valsalva ensure a forward flow in aorta that is greater than the corresponding one in an aorta without sinuses. The vortex formation in the sinus of Valsalva supports the opening and the closing motion of the leaflets valve during the cardiac cycle; nevertheless, the phenomena of slow moving fluid is well documented in the sinuses region, as is the thrombus formation on the valve's cuff. The recirculating vortex measured in the sinus cavity during the ejection period is believed both to provide a beneficial wash-out of the valve region and assist in valve closure, and was observed in most aortic valves by Hwang et al. (12). The detailed analysis carried out in the present study allowed to highlight the presence of vortices, in terms of magnitude and size, in the sinus, which seems to be a favourable condition for feeding the coronary arteries (5).

Conclusions

The evaluation of the fluid dynamical behaviour of PHVs is of fundamental importance to discriminate on their correct functionality, especially in those quantities which can be related to thrombogenicity and hemolysis: as these quantities are given by statistics of higher order than the simple velocity average, care must be taken in the accuracy of the measure. Considering PIV technique as a reliable measurement solution for the complete analysis of prosthetic heart valves related fluid dynamics, several methodological and technological problems are still open. An experimental investigation was conducted upon the unsteady features of the flow in an aortic root model geometry downstream of a PHV by means of PIV. The method proposed in (3) was used to detect the footprints of both the vortices shedding from the leaflets and moving through the Valsalva sinuses. Further analysis on singular vortices tracking in time and the obtained trajectories will allow to draw some conclusions about the typical vortex lifecycle in the Valsalva sinus (highlighting the major mechanisms of vortex shedding, large-scale vortex interaction, vortex-wall interaction in the sinuses). PIV technique coupled with a robust method for vortex identification and an analysis of trajectory data constitute a valuable tool for the study of coherent structures dynamics.

References

1. Uzol O, Camci C. The effect of sample size, turbulence intensity and the velocity field on the experimental accuracy of ensemble averaged PIV measurements. 4th International Symposium on Particle Image Velocimetry G□ttingen, Germany, September 17-19, 2001.

2. Grigioni M, Daniele C, Morbiducci U, Di Meo D, D'Avenio G, Del Gaudio C, Barbaro V. Particle Image Velocimetry to study the fluid dynamics of prosthetic mechanical valves: open problems. Proceedings on XII Mediterranean Conference on Med Biol Eng Comp, 2004, Ischia, Italy; pps 4.
3. Jeong J, Hussain F. On the identification of a vortex. *J Fluid Mech* 1995;285:69-94.
4. Barbaro V, Grigioni M, Daniele C, D'Avenio G, Boccanera G. 19 mm sized bileaflet valve prostheses' flow field investigated by bidimensional laser Doppler anemometry (part I: velocity profiles). *Int J Artif Organs* 1997:20(11):622-8.
5. Bellhouse BJ, Bellhouse FH, Reid KG. Fluid mechanics of the aortic root with application to coronary flow. *Nature* 1968;219:1059-61.
6. Ohta Y, Kikuta Y, Shimooka T, Mitamura Y, Yuhta T, Dohi T. Effect of the sinus of valsalva on the closing motion of bileaflet prosthetic heart valves. *Artif Organs*. 2000;24(4):309-12.
7. Office of Science and Technology (OST) Annual Report Fiscal Year 2001
8. Grigioni M, Daniele C, D'Avenio G, Morbiducci U, Del Gaudio C, Abbate M, Di Meo D. Innovative technologies for the assessment of cardiovascular medical devices: state of the art techniques for artificial heart valves testing. *Expert Review of Medical Devices* 2004;1(1):89-101.
9. Barbaro V, Grigioni M, Daniele C, D'Avenio G. A discussion on the threshold limit for hemolysis related to Reynolds shear stress. *J Biomech* 1999;32:1107-12.
10. Browne P, Ramuzat A, Saxena R, Yoganathan AP. Experimental Investigation of the Steady Flow Downstream of the St Jude Bileaflet Heart valve: A Comparison Between Laser Doppler Velocimetry and Particle Image Velocimetry Techniques. *Ann Biomed Eng* 2000;28(1):39-47.
11. Bellhouse BJ, Talbot C. The fluid mechanics of the aortic valve. *J Fluid Mech* 1969:35:721-35.
12. Hwang NH, Reul H, Reinhard P. *In vitro* evaluation of the long-body On-X bileaflet heart valve. *J Heart Valve Dis* 1998;7(5):561-8.

STEADY STATE INVESTIGATION OF TURBULENT FLOW FIELD DOWNSTREAM OF HEART VALVE PROSTHESIS

Costantino Del Gaudio, Umberto Morbiducci, Mauro Grigioni
Dipartimento di Tecnologie e Salute, Istituto Superiore di Sanità, Rome, Italy

Introduction

The investigation of the fluid dynamic behavior of mechanical heart valves requires a particular care in order to evaluate the fluidic pattern associated to these prosthetic devices, being not free from complications related to the non physiologic flow regime established through and downstream of mechanical valves; it is possible to detect high shear stress, local flow recirculation that may induce damage to blood cells, i.e. platelet activation (1).

Computational fluid dynamics (CFD) represents an useful tool in order to furnish a detailed description of the complex flow regime and pressure fields associated to mechanical heart valve, to be integrated with experimental results to have a full characterization of the device under study, allowing to obtain information in districts not easily accessible by means of experimental methodologies (2). For this aim the analysis of the turbulent flow field established through and downstream of a bileaflet heart valve was performed by means of computational fluid dynamics in steady state conditions.

Material and methods

Computational model

The fluidic pattern relative to a mechanical heart valve, similar to St Jude 23 HP, was investigated in turbulent conditions for 25, 30, 35 L/min adopting two turbulence models: the k-ε and the k-ω, in which k is the turbulent kinetic energy, ε is the dissipation rate and ω is the specific dissipation rate.

The geometrical model of the valve, with leaflets fixed in the fully open position, was placed in a cylindrical tube, having the internal diameter equal to 35 mm (to allow proper comparison with ISO5840 steady flow set-up). Velocity boundary conditions were set at the inlet section, according to the prescribed flow rate investigated, for Reynolds number ranging from about 4500 to 6500 based on the internal diameter of the cylindrical tube. The entire geometrical model was discretized by means of tetrahedral elements (about 1520000) using the pre-processor Gambit (Fluent, Lebanon, NH), taking particular care for the discretization in the near wall regions to properly resolve the viscous sublayer setting the first grid point at $y^+ \leq 1$ (y^+ is the non-dimensional height of the viscous sublayer), being this approach more suited for the k-ω model (3). Successively, the general purpose computational fluid dynamics code Fluent (Fluent, Lebanon, NH) was adopted to solve the three-dimensional flow domain. The fluid was assumed to be Newtonian, homogeneous, incompressible and experimentally simulated by water-glycerol solution.

Experimental set-up

The St Jude bileaflet valve (23 mm tissue annulus diameter) was tested in a steady-flow apparatus, in which the flow was driven by a constant head tank, using water-glycerol solution (35%) as testing fluid to take into account the physic properties of the blood (density ~ 1060 kg/m^3 and dynamic viscosity ~ 3.5 cP). Three flow rates were imposed, ranging from 25 to 35 L/min in step of 5 L/min, to analyse the pressure recovery of this biomedical device (4).

Pressure was measured along 17 equispaced taps (Δx = 17.5 mm) placed on a plexiglass test pipe, as required by the CEN EN 12006-1 Directive (5), by means of visual inspection of the height of the solution column above each pressure tap. The precision of the measurements can be conservatively quantified to be on the order of 0.5 mm of fluid, thus the uncertainty on pressure measurements was 0.039 mmHg. Pressure measurements so collected were then interpolated by cubic splines in order to estimate the maximum pressure drop at vena contracta. Flow rate was measured with an electromagnetic flow probe (<0.1% accuracy) (Endress & Hauser, Atlanta, GA, USA).

The experimental set-up is reported in Figure 1.

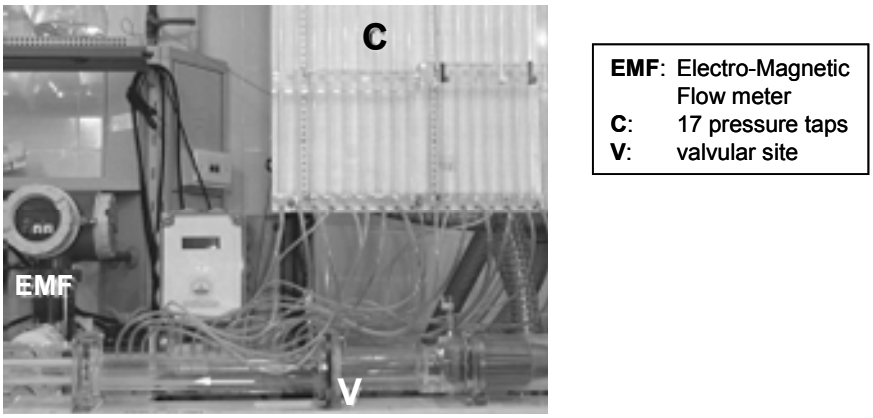

Figure 1. Experimental set-up

Results

Axial velocity contour map, in the transversal section of the model, is reported in Figure 2 for 30 L/min: it is evident the difference in the extension of the jets outcoming from the mechanical valve as predicted by the two numerical models. The k-ε model presented a more localized velocity structure in the middle of the geometrical model while the k-ω model resulted in a wider area interested by the typical three jets outcoming from the valve with a less spatial localization along the central axis. Moreover this latter turbulent model predicted a more evident central jet with respect to the other numerical model.

In Figure 3 the comparison of pressure recovery predicted by the two turbulent numerical models implemented, measured along 17 equally spaced transversal section as in the experimental set-up, and the experimental results is reported.

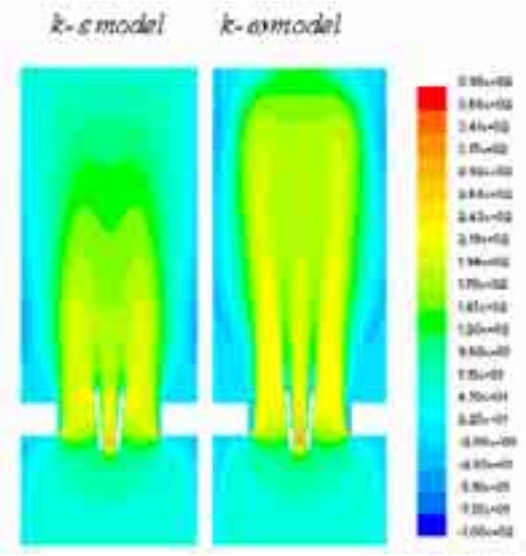

Figure 2. Axial velocity contour plot for 30 L/min resulting from the two turbulent numerical simulations (cm/s)

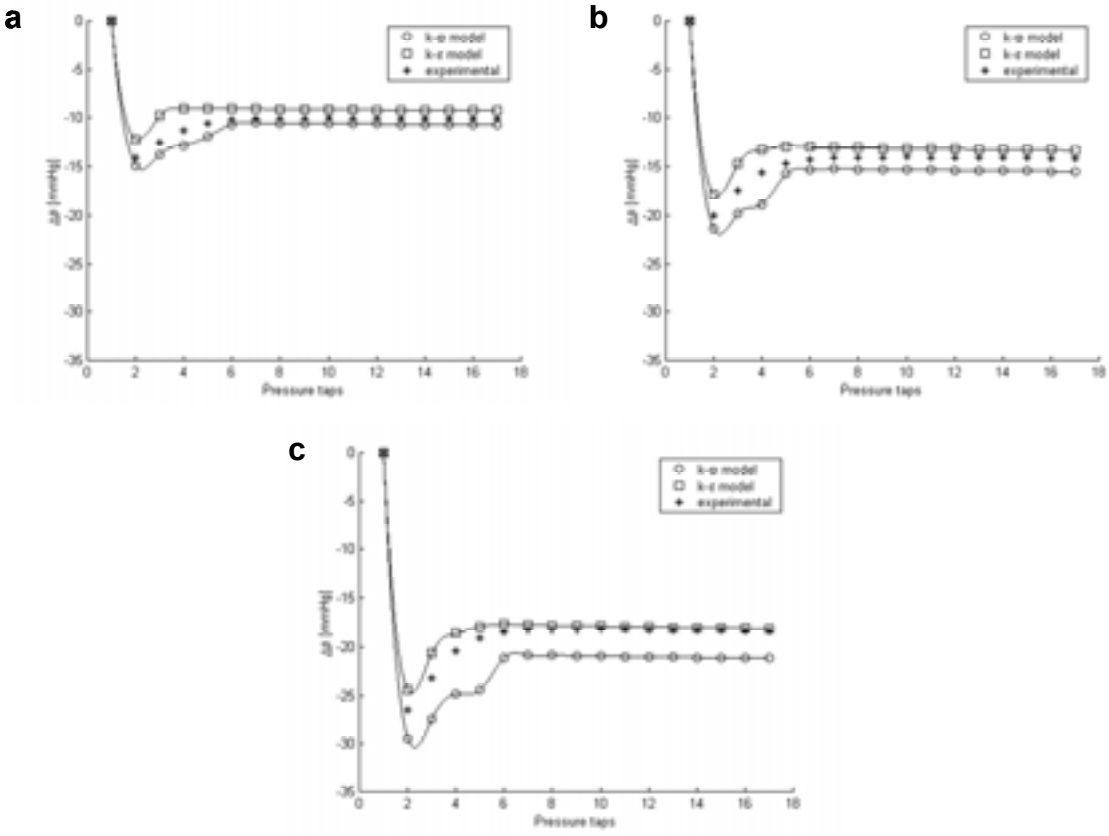

Figure 3. Comparison of pressure recovery as resulted from the two turbulent numerical simulations and from the experimental investigation

Discussion

Numerical simulation here considered highlighted the different behavior of two turbulent models implemented with respect to the experimental set-up, in order to compare the CFD prediction of the fluid dynamic performance of a mechanical heart valve in turbulent conditions. The analysis of the flow regime established downstream of the investigated prosthetic device revealed different velocity patterns, highlighting stronger outcoming valvular jets in the prediction of the k-ω turbulent model. At the same time, the investigation of the pressure recovery, compared to the experimental results, showed a substantial agreement for both the numerical models. The k-ε model highlighted a slight underestimation with respect to the measured pressure drop curve of the prosthetic valve under study while the k-ω showed an overestimation especially for the maximum pressure drop value. Moreover the k-ω presented a particular distribution of the pressure drop immediately past the valve, especially for higher flow rates, that the other model did not show, resembling the experimental distribution in a better way compared to k-ω turbulent model. A possible explanation for this result can rely on the fact that the k-ω model has been developed to study the transitional effect from laminar to turbulent regime while the implementation of the k-ε model assumes isotropic turbulence (6).

Numerical steady state simulations of turbulent flow associated to mechanical heart valve revealed good agreement in the prediction of the pressure recovery distribution, compared to experimental measures, especially for the k-ε model; however more investigations are needed in order to have a fully validation of numerical codes with respect to experimental measurement session, also regarding the velocity patterns.

References

1. Bluestein D, Li YM, Krukenkamp IB. Free emboli formation in the wake of bi-leaflet mechanical heart valves and the effects of implantation techniques. *J Biomech* 2002;35(12):1533-40. Erratum in: *J Biomech* 2003;36(7):1065-6.
2. Shipkowitz T, Ambrus J, Kurk J, Wickramasinghe K. Evaluation technique for bileaflet mechanical valves. *J Heart Valve Dis* 2002;11:275-82.
3. Varghese SS,Frankel SH. Numerical modeling of pulsatile turbulent flow in stenotic vessels. *J Biomech Eng* 2003;125:445-60.
4. Grigioni M, Daniele C, D'Avenio G, Barbaro V. Hemodynamic performance of small-size bileaflet valves: pressure drop and Laser Doppler Anemometry study comparison of three prostheses *Artif Organs* 2000;24(12):959-65.
5. UNI EN 12006-1. Impianti chirurgici non attivi. Requisiti particolari per impianti cardiaci e vascolari. Protesi valvolari cardiache. Milano: Ente Nazionale di Unificazione; 2001.
6. Bluestein D, Li YM, Krukenkamp IB. Free emboli formation in the wake of bi-leaflet mechanical heart valves and the effects of implantation techniques. *J Biomech* 2002;35:1533-40.

NUMERICAL SIMULATION OF THE AORTIC ARCH FLOWS

Costantino Del Gaudio, Umberto Morbiducci, Mauro Grigioni
Dipartimento di Tecnologie e Salute, Istituto Superiore di Sanità, Rome, Italy

Introduction

Atherosclerotic lesions arise preferentially in vascular districts in which the local geometry presents bending, branching and non-planar configuration (1). The related fluidic pattern and the physiologic pulsatility result in fully three-dimensional structures in which velocity profiles inside the vessels result highly skewed. Thus shear stress distribution in these sites can induce the vascular response of the endothelium: fluidic forces acting on the vessels' wall can stimulate the endothelium to produce several cellular factors that can inhibit or promote inflammatory events (2); the production of these factors seem to be related to the local fluid dynamics, highlighting that vascular districts of low shear stress are eligible for the formation of atherosclerosis (2). The effect of the fluid mechanically stress induced on the endothelium, the innermost of the vascular intima, can be regarded as a cause in the initiation of atherogenic lesions in particular sites (3).

To investigate on the relationship between flow field and associated shear stress and on the possible vascular response to mechanical stimulus induced by complex flow patterns, a numerical time dependent simulation in a aortic arch model, complete of a realistic aortic root and of the principal arterial vessels, is presented.

Material and methods

A three-dimensional time dependent numerical simulation has been investigated in a non-planar geometric model of aortic arch complete of a realistic aortic root and of the major branches for a peak Reynolds number of 2200 and a Womersley number of 20.4. The geometrical model is shown in Figure 1 in two different views to highlight the non-planar configuration.

The model was discretized by means of eight nodes hexahedral elements (about 442000) using the pre-processor Gambit (Fluent, Lebanon, NH); vessels was connected to the aorta allowing to discretize each of them separately. Computational fluid dynamic code Fluent (Fluent, Lebanon, NH) was successively adopted to solve the three-dimensional unsteady Navier-Stokes equations and the continuity equation, as below reported:

$$\rho \frac{Du}{Dt} = -\nabla p + \nabla \tau \qquad [1]$$

$$\nabla u = 0 \qquad [2]$$

where u is the velocity vector, ρ the density of the fluid, p the pressure and τ the stress tensor. A plug time-dependent velocity profile was imposed at the inlet section of the aortic root; this boundary condition was acquired in an experimental session on a bioprosthetic aortic valve in a mock circulatory loop (Vivitro System, Inc., Canada).

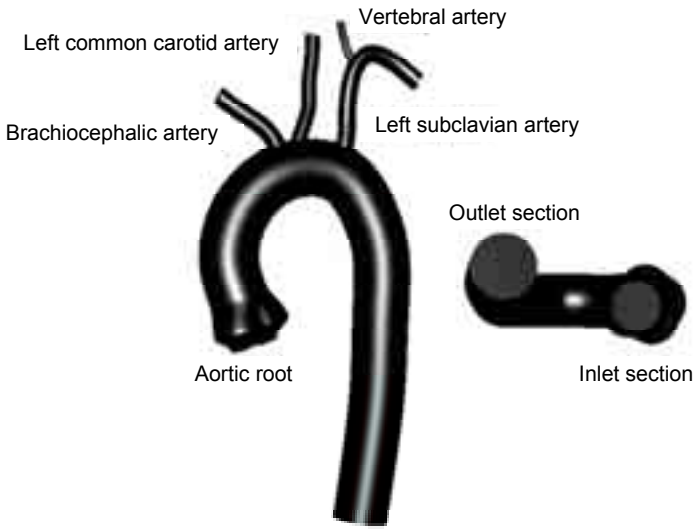

Figure 1. Numerical model of the aortic arch completed of principal and secondary branches

Figure 2 shows the velocity waveform implemented, normalized with respect to the systolic peak velocity value.

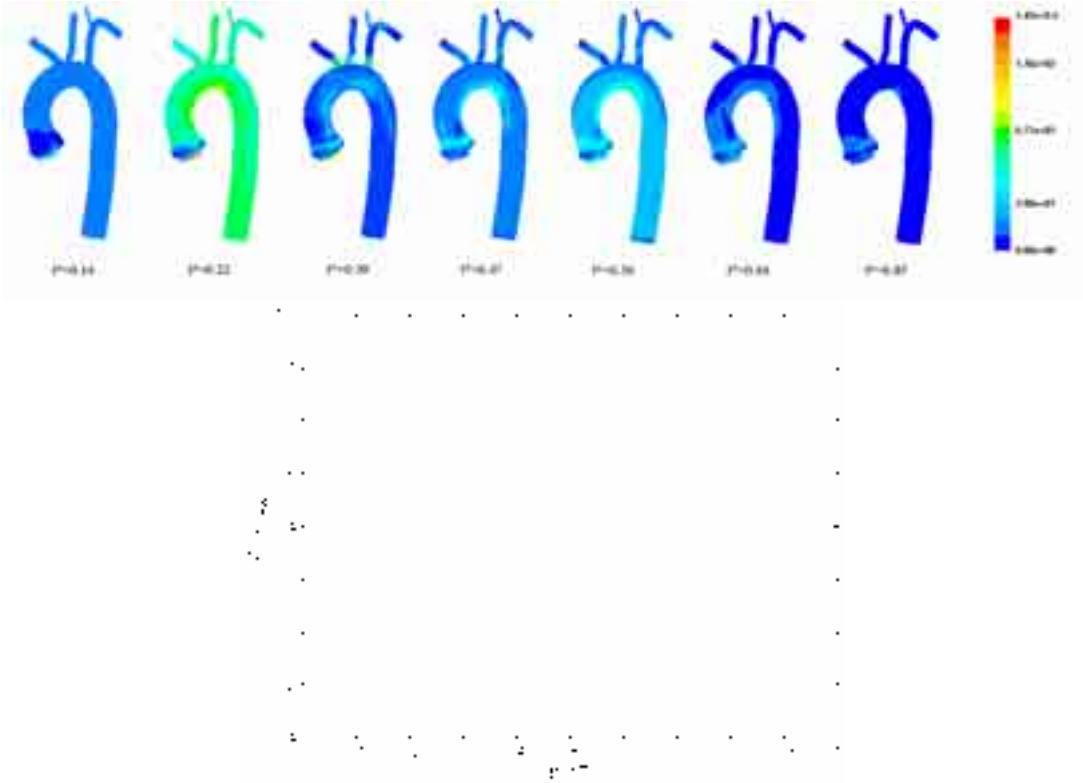

Figure 2. Normalized wall shear stress of the numerical model for the selected time instants within the cardiac cycle (upper panel); normalized inlet velocity curve (lower panel)

Blood was assumed to behave like a non-Newtonian fluid with a constant density of 1.06 g/cm^3 and viscosity described by the following power-law formulation $\mu=0.1344\gamma^{(0.7485-1)}$ cP (γ is the shear rate) with a yield stress at 0.1 s, based on findings of previous researchers (4, 5) for a hematocrit level of 40% at 37 °C.

Results

Normalized wall shear stress (6), is presented according to the following formulation:

$$\tau^* = \frac{\tau_W}{\tau'} \qquad [3]$$

where τ_W is the dimensional wall shear stress and $\tau' = \frac{\mu U_{mean}}{r}$ (μ is the dynamic viscosity at high shear rate, Newtonian behaviour; U_{mean} the mean velocity value the inlet section and r the radius of the inlet section).

τ* is reported in Figure 2 for seven time-steps within the simulated cardiac cycle. Higher values of τ* can be highlighted on the curvature of the aortic arch and in the inserting regions of the secondary vessels with respect to the principal ones (the brachiocephalic, the left common carotid and the left subclavian arteries on the aortic arch and the vertebral artery on the left subclavian artery). Highest values of τ* are reached at the systolic peak showing a nearly uniform distribution in the numerical model (t*=0.22), while relevant differences in the spatial distribution of τ* are evident in the deceleration phase (t*=0.39) and at the end of the dynamic regurgitation phase (t*=0.64) in which the highest value for the normalized shear stress is located along the inner wall of the aortic arch. The spatial distribution of τ* at about the peak of the reversal flow (t*=0.56) shows low values on the outer wall of the aortic arch and on the distal walls of the three principal branches with respect to the position of the aortic root.

Discussion

The computational study here presented was performed by modelling the aortic arch and its principal branches on the basis of findings of previous researchers (1, 6): in this way the effects of non-planar geometry has been took into account to reach a more realistic shape of this anatomical vascular district. Moreover the reconstructed model does not necessarily represent a limitation due to the highly variability of the configuration of the aortic arch (6). This study highlighted the reliability to perform a fluid dynamics analysis in a fully three-dimensional vascular model showing the characteristic flow structures and the wall shear stress distribution which is considered one of the main causes in the promotion of vascular diseases. The investigation on the correlation between the established fluid dynamic pattern and the intimal thickening underlines that atherosclerotic plaques are localized in regions with low and oscillating shear stress; moreover a degeneration of the intimal thickening into atherosclerotic plaques can be observed if low-density lipoprotein concentrations are present (3) and if further mechanical stress leads to endothelial injury (7).

This study showed the investigation of the basic fluid dynamics in the aortic arch and in its major branches, highlighting the complexity of the wall shear stress distribution along the model, giving the possibility to localize particular regions prone to vascular lesions.

The model presented will be the set-up of different virtual or conceptual experiments to infer on how valve haemodynamics can alter the shear stress distribution all along the aortic arch and relative branches.

References

1. Mori D, Yamaguchi T. Computational fluid dynamics modeling and analysis of the effect of 3-D distortion of the human aortic arch. *Comput Methods Biomech Biomed Engin*. 2002;5(3):249-60.
2. Yoshizumi M, Abe J, Tsuchiya K, Berk BC, Tamaki T. Stress and vascular responses: atheroprotective effect of laminar fluid shear stress in endothelial cells: possible role of mitogen-activated protein kinases. *J Pharmacol Sci* 2003;91:172-6.
3. Chandran KB. Flow dynamics in the human aorta: techniques and applications. Chapter 5. In: Leondes CJ (Ed.). *Biomechanic systems techniques and applications*. Boca Rato, FL: CRC Press; 1997. p 5.1-5.25.
4. Merrill EW. Rheology of blood. *Physiol Rev* 1969;49(4):863-88.
5. Walburn FJ, Schneck DJ. A constitutive equation for whole human blood *Biorheology* 1976;13(3):201-10.
6. Shahcheraghi N, Dwyer HA, Cheer AY, Barakat AI, Rutaganira T. Unsteady and three-dimensional simulation of blood flow in the human aortic arch *J Biomech Eng* 2002;124(4):378-87.
7. Kensey KR. The mechanistic relationships between hemorheological characteristics and cardiovascular disease. *Curr Med Res Opin* 2003;19(7):587-96.

Stampato da Tipografia Facciotti srl
Vicolo Pian Due Torri 74, 00146 Roma

Roma, dicembre 2005 (n. 4) 22° Suppl.